Feasibility study of magnetic field measurement system using cosmic-ray muons

ハミッド, バシリ

Feasibility study of magnetic field measurement system using cosmic-ray muons

九州大学
KYUSHU UNIVERSITY

Hamid Basiri

Department of Advanced Energy Engineering Science
Kyushu University

This dissertation is submitted for the degree of
Doctor of Engineering

August 2023

I would like to dedicate this thesis to my beloved family,
and my supervisor, Professor Tadahiro KIN . . .

Declaration

I hereby declare that except where specific reference is made to the work of others, the contents of this dissertation are original and have not been submitted in whole or in part for consideration for any other degree or qualification in this, or any other university. This dissertation is my own work and contains nothing which is the outcome of work done in collaboration with others, except as specified in the text and Acknowledgements.

Hamid Basiri
August 2023

Acknowledgements

I completed this thesis at the Kin Laboratory, Department of Advanced Energy Engineering Sciences (AEES), within the Interdisciplinary Graduate School of Engineering Sciences (IGSES) at Kyushu University.

I wish to express my profound gratitude to my academic mentor, Associate Professor Tadahiro KIN. His guidance, mentorship, and encouragement were priceless throughout my research journey. His broad knowledge and wisdom served as my guiding light in this demanding yet fulfilling endeavor. His teachings, which go beyond academia, will remain a source of inspiration for me in my future endeavors. The lessons I've learned from Dr. KIN have had a tremendous impact on my personal and academic growth.

I am especially thankful to our esteemed research collaborators from UCLouvain University, Dr. Andrea Giammanco and Prof. Eduardo Cortina Gil. Dr. Giammanco's insightful recommendations and contributions were key to the successful completion of this project. I am deeply grateful for his willingness to share his knowledge and experience, as well as for his continuous encouragement and support throughout the research process. Similarly, I wish to express my heartfelt appreciation to Prof. Eduardo Cortina Gil for his collaboration, support, and valuable feedback on my research. I am grateful for his willingness to work with me on this project and for the friendship and support he has shown. Their significant contributions have undoubtedly enriched this research endeavor, and I feel truly honored to have had the opportunity to work with such accomplished scholars.

I extend my gratitude to Professor Kenichi WATANABE and Professor Takeshi IDO for their careful review of this thesis and their constructive comments. Their insights greatly enhanced my understanding of crucial aspects of this thesis.

I also want to express my thanks to Professor Yukinobu WATANABE and Assistant Professor Shoichiro KAWASE. Their knowledge and constructive feedback significantly improved my research. Their readiness to share their insights was instrumental to my growth.

I am grateful to all the members of the Kin and Watanabe Laboratories. Special thanks to Dr. Katsumi Aoki, Dr. Hikaru Sato, Mrs. Mikhail Mary Alfone, Mr. Naoya Okamoto, Mr. Wataru Sekiguchi, Mr. Takahiro Kihara, Mr. Taisei Eto, Mr. Taiki Kawanoga, Mr. Yasuhiro Aso, Mr. Yuto Tanaka, Mr. Hiroto Shiba, Mr. Yunji Shinjo, Mrs. Satoko Kamei, and others

for their help and support. I also thank Ms. Takako Kimura, Ms. Kazuyo Mine, and Ms. Rumiko Koga for their administrative support. The enriching environment and advanced resources provided by the lab significantly contributed to this work.

My gratitude also extends to the organizers of the Kyushu University Intellectual Exchange and Innovation Program (IEI Program) for providing the opportunity to join the Ph.D. program, and to the International Student Support Center Chikushi Campus, AEES departmental office for their continual support during my studies.

I am profoundly thankful to the Japanese Government (Monbukagakusho: MEXT) Scholarship for their financial aid, which enabled me to pursue my academic ambitions. This scholarship provided me with the opportunity to explore this intriguing field of research.

Finally, I am grateful to my parents, wife, family, and friends for their love and support. Their encouragement has been my driving force, and without them, this work would not have been possible.

This research journey, while challenging, has been greatly rewarding. None of it would have been possible without the support and assistance of all these individuals and institutions. My deepest appreciation goes to all.

Abstract

Over a hundred years ago, Victor Hess's groundbreaking discovery of cosmic rays marked a new era in the field of particle physics. One of the most remarkable advancements in this field is the use of cosmic-ray muons. These particles, showering the Earth's surface at a rate of roughly 10,000 per square meter per minute, have been deployed for a variety of applications. Their unique properties, including the ability to penetrate deeply into any material, their universal availability (even underground), nearly perfect detection efficiency, and non-destructive interaction with objects, make them invaluable. One notable technique that leverages these properties is muon radiography, also known as muography. This technique primarily serves two major purposes: it enables the survey of the internal structure of large objects through the absorption ratio and facilitates the inspection of hidden nuclear materials based on scattering angle.

This technology was initially employed by Alvarez for the purpose of exploring hidden chambers within the pyramids. Despite the initial promise and potential of this technology, there was a period of prolonged inactivity, largely due to the technological demands of muography detectors which limited its widespread applications. Nevertheless, with the recent breakthroughs in detector technology such as large scale data acquisition system, commercial detector availability, and data analysis technology made many researchers possible to apply muography for various targets. The application of muography has expanded to areas such as volcanology, geotomography, nuclear waste investigations, nuclear reactor inspections, detection of high-Z materials, imaging of cultural heritage artifacts, and even assessing infrastructure degradation.

Magnetic fields are one of the principal forces in nature, playing an instrumental role in a multitude of natural phenomena and technological applications, including but not limited to accelerators, medical imaging, electric cars, and fusion reactors. However, existing methods for accurately measuring and monitoring magnetic fields are not without limitations. Traditional magnetic field detection techniques, such as Hall effect sensors and loop coils, although useful in providing valuable data on local magnetic fields, often lack for measuring large targets and they must touch the magnetic field to provide us the information of the

magnet and inserting the probe will cause some difficulties. As a result, there is an increasing effort to improve magnetic field detection and characterization.

Muon particles are fundamentally elementary particles similar to electrons, but much heavier. They carry an electric charge identical in magnitude to that of an electron, and we find both positive and negative muons. This characteristic is crucial when discussing their behavior in magnetic fields. Due to their charged nature, muons are subject to the Lorentz force when moving through a magnetic field, which can deflect their trajectory. Notably, this deflection is not random; instead, it follows a helical path as dictated by the right-hand rule. The degree of deflection is influenced by several factors, including the muon's velocity, charge, and the strength of the magnetic field. This study explores the feasibility of using cosmic-ray muons, given their natural abundance, unique characteristics, and behavior in magnetic fields, as potential tools for magnetic field measurement. Simultaneously, the effect of magnetic fields on muography images and material identification is significant, yet there are no studies addressing the interference of magnetic fields in muon-based material identification systems, a promising technology for security inspections. In this thesis, we also investigate the impacts of magnetic fields on scattering muography inspection systems.

This thesis aims to address a gap in current understanding by investigating the feasibility and potential of cosmic-ray muons, for the detection, imaging, and measurement of magnetic fields. Despite the significant progress and potential exhibited by muography in various applications, its use in detecting magnetic fields remains largely unexplored. Furthermore, while existing magnetic field measurement techniques demonstrate impressive capabilities, they are not without limitations that necessitate the exploration of alternative approaches such as muography. The findings from this study suggest that under appropriate conditions, muography could potentially be utilized for magnetic field detection and measurement. We examined two methods; the first one, akin to transmission muography, appears promising when the magnetic field is strong (almost tesla order) and acts as a shield for low-energy muons. The second method is rooted in scattering muography, and our results demonstrated that by using techniques such as PoCA, we can identify the position of the magnetic field and this method may also assist in estimating the magnetic flux density.

Keywords: Cosmic-ray, Muon, Muography, Magnetic Field, Muon Tomography

Table of contents

1 Introduction **1**

1.1 Cosmic-ray Muons . . . 1

1.1.1 Cosmic-ray Muon Creation Processes . . . 2

1.2 Muography . . . 3

1.2.1 Historical Evolution of Muography . . . 4

1.2.2 Principles of Muography . . . 5

1.2.3 Muography Detectors . . . 9

1.2.4 Muography Application Areas . . . 11

1.3 Magnetic Field Measurement Techniques . . . 14

1.4 Study Objectives . . . 15

1.5 Overview of the Thesis . . . 16

2 Methodology **19**

2.1 Muons Motion in a Magnetic Field . . . 19

2.2 Cosmic-Ray Spectrum Models . . . 24

2.2.1 PARMA Model . . . 26

2.2.2 CORSIKA (COsmic Ray SIMulations for KAscade) . . . 27

2.2.3 CRY . . . 27

2.3 Interaction of Muons with Matter . . . 28

2.4 Particle Transport Tools . . . 34

3 Magnetic field muography detectors **37**

3.1 Transmission Method . . . 37

3.1.1 Transmission Muography Detector Design . . . 37

3.1.2 Transmission Muography Analysis Method . . . 41

3.2 Deflection Method . . . 43

3.2.1 Detector Design . . . 43

3.2.2 Coulomb Scattering Angle . . . 44

3.2.3 Magnetic Field Deflection Angle 47
3.2.4 Analysis Method for Deflection Method 49
3.2.5 Magnetic Flux Density Estimation Through Shift in PoCA Points . 50
3.3 Muon Energy Spectrometer 57
3.3.1 Magnetic spectrometer 58
3.3.2 Time-of-Flight (ToF) 61
3.3.3 Multi-layer Muon Energy Spectrometer 61

4 Feasibility Simulations **63**
4.1 Transmission method 63
4.1.1 Strong Magnetic Fields 63
4.1.2 A Dipole Magnet with a Magnetic Field of 200 mT 66
4.2 Deflection Method 70
4.2.1 Magnetic Field Effect in Material Detection 70
4.2.2 Magnetic Field Effect in Imaging using Cosmic-ray Muons 76
4.2.3 Magnetic Flux Density Estimation using a Known Magnet 78
4.2.4 Magnetic Flux Density Estimation Through PoCA Point Analysis . 79
4.3 Summary 82

5 Conclusions **85**
5.1 Summary of Findings 85
5.2 Prospects 86
5.3 Concluding Remarks 86

References **87**

Appendix List of figures **93**

Appendix List of tables **97**

Chapter 1

Introduction

This chapter provides an overview of the principles and current state of cosmic-ray muon research and muography. It also introduces the potential applications of muography in magnetic field measurements, elaborates on the current techniques and their limitations, and outlines the objectives and scope of this thesis.

1.1 Cosmic-ray Muons

Cosmic-ray muons are elementary particles, discovered in 1937 by American physicists S. H. Neddermeyer and C. D. Anderson, who identified a particle with the same absolute charge and 207 times larger mass as those of electrons [1]. This particle, denoted by μ, has since been classified as a lepton in particle classifications, an integral concept in the field of particle physics.

Particles are broadly classified into three groups: bosons, leptons, and hadrons, as illustrated in Figure 1.1 [2]. The lepton class, which includes the muon (μ), consists of six particles: the electron, muon, tau, and their corresponding neutrinos. Each of these particles exists in two forms: a negatively charged version and a corresponding neutrino. In the case of muons, there are two types (μ^- and μ^+) which share the same mass but bear opposite charges. The μ^- muon carries the same charge as an electron, while the μ^+ muon bears the positron's charge. Both types of muons are unstable, with a lifetime of 2.2×10^{-6} s. Muons decay with the following reactions:

$$\mu^- \rightarrow \beta^- + \nu_e + \overline{\nu}_e \tag{1.1}$$

$$\mu^+ \rightarrow \beta^+ + \overline{\nu}_\mu + \nu_e \tag{1.2}$$

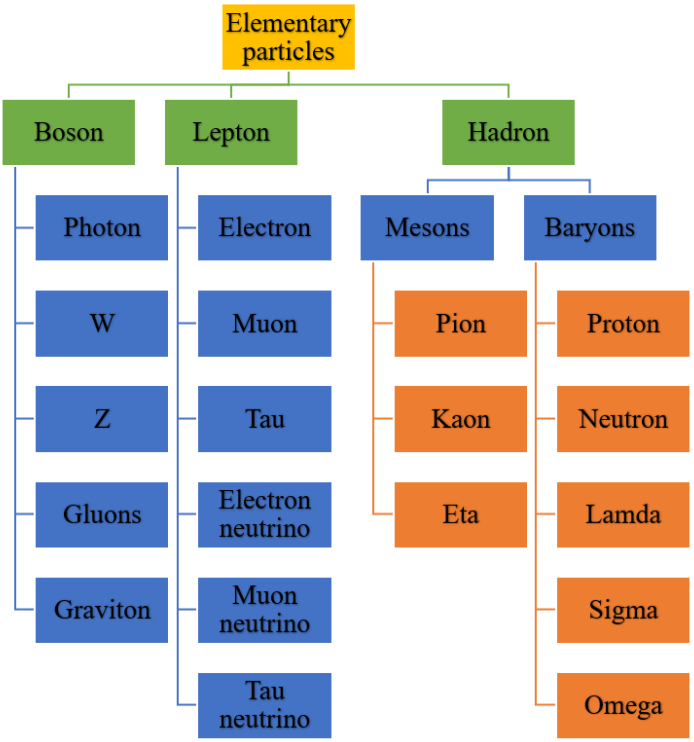

Fig. 1.1: Particle classification.

1.1.1 Cosmic-ray Muon Creation Processes

Cosmic-ray muons are produced through the interaction of primary cosmic rays with atmospheric nuclei. They decay products of kaons and pions which are generated in a spallation reaction.

There are three types of pions: positive (π^+), negative (π^-), and neutral (π^0). The charged pions are unstable, with a lifetime of 2.6×10^{-8} s. Charged pions almost decay into a muon and the neutral pion (π^0) decays into two γ-ray photons within a lifetime of 0.8×10^{-16} s as described by the following equations:

$$\pi^\pm \rightarrow \mu^\pm + \nu_\mu(\overline{\nu}_\mu) \tag{1.3}$$

$$\pi^0 \rightarrow \gamma + \gamma \tag{1.4}$$

Another source of cosmic-ray muons is the decay of kaons. Kaons can decay into various particles, including muons, as demonstrated by the following decay equations:

$$K^{\pm} \rightarrow \mu^{\pm} + \nu_{\mu}(\overline{\nu}_{\mu}) \tag{1.5}$$

$$K^{\pm} \rightarrow \mu^{\pm} + \pi^0 \tag{1.6}$$

A schematic view of the extensive air shower created due to interaction of high-energy primary proton is illustrated in Figure 1.2 [3].

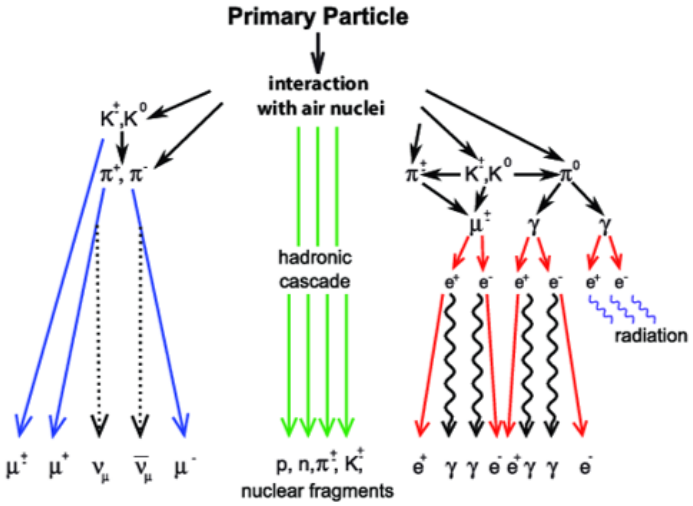

Fig. 1.2: Schematic view of an extensive air shower.

1.2 Muography

Cosmic-ray muons, a naturally occurring radiation source, exhibit distinct properties: deep penetration into materials, universal availability (even underground), near-total detection efficiency, and non-destructive interaction with objects. Such characteristics render muons a valuable tool for imaging and non-destructive testing of a broad array of targets. The advent of

sophisticated reconstruction algorithms has further enhanced the potential for data extraction from each muon measurement, addressing concerns related to lengthy measurement durations. The exploitation of these particles has given birth to a technique known as "muography", which is defined as "a technique to scan internal structure by cosmic-ray muons". This innovative imaging technique has found applications in diverse fields, spanning from geology and civil engineering to archaeology and particle physics.

In muography, muon positions or rates are measured using particle detectors. By comparing these rates or the displacement of muons, the density distribution of the object can be obtained. Based on the attenuation or scattering of muons, two distinct types of muography techniques have been developed. These have contributed to the expansion of muography applications. The techniques and applications of muography will be discussed in more detail in the subsequent sections.

1.2.1 Historical Evolution of Muography

Muography is a technique stemming from a series of discoveries and technological advancements over the last decades. In 1912, Austrian physicist Victor Hess discovered cosmic rays during a series of hot air balloon rides, aimed at finding the source of ionization radiation from the ground and atmosphere [4]. His highest altitude was 5.3 km, leading to a Nobel Prize in 1936. The existence of muons was first suggested in 1933 by Paul Kunze using a Wilson Cloud Chamber exposed to cosmic rays. However, it was unclear what this particle was at the time. American physicist Carl Anderson and his student Seth Neddermeyer definitively discovered muons in 1936 [1].

With the birth of the first generation of particle accelerators in the 1950s, the scientific knowledge about muons and their applications accelerated. One such accelerator was the Synchrocyclotron at CERN. The first record of muons, produced by cosmic rays, was their use by Eric George to measure the ice thickness above a tunnel in Australia in 1955 [5]. Luis Alvarez's team used muon radiography in 1969 to search for hidden chambers in the Pyramid of Khafre in Egypt, although no hidden chambers were found at that time [6].

Substantial advancements in muon tomography occurred in the late 20th and early 21st centuries. For instance, in 1987, muons measured the depth of Nagoya's underground system tunnels using scintillator detectors [7]. In 1999, the Soudan II detector in Minnesota, USA, observed the "shadow" of the moon by measuring the muon flux [8]. In 2003, the Pyramid of the Sun's interior in Mexico was prepared for inspection by a muon detector [9], and the same year saw the pioneering use of muon scattering at Los Alamos National Laboratory to identify high-Z materials for detecting nuclear materials [10].

Muon radiography measured Mount Asama's average density profile in Japan in 2007, marking the first application of muon tomography to geological structures like volcanoes [11]. In 2009, the National Institute of Nuclear Physics of Italy built a large-volume muon tomography system, demonstrating the ability to differentiate between various materials based on muon scattering [12]. In 2012, simulations of the Fukushima-Daiichi Nuclear Power Plant indicated muon tomography's feasibility to identify voids and track material movement within the core of the damaged reactor [13]. That year also saw the start of an investment project to use muography for monitoring carbon dioxide levels in deep sub-surface carbon storage sites and a proposal by Atomic Energy of Canada Limited to use muons for nuclear waste imaging and spent fuel verification [14].

In 2013, muon transmission tomography probed the volcanic dome of Puy de Dôme, France [15], and Caltech researchers proposed using muon tomography to map Martian terrain, suggesting rovers equipped with muography systems could observe Martian geological structures [16]. In 2014, a muon tomography-based monitoring system detected minor deformations in Italy's Palazzo della Loggia, dating back to 1574 [17], and the first images of nuclear waste containers' interior were obtained by the Sellafield Muon Tomography project in the UK [18].

The WatTo experiment conducted in Saclay, France, in 2016, used a muon transmission tomography telescope to observe a water tower to detect density variations inside the tower, correlating to changes in water levels [19]. Muon transmission tomography was also used to study the interior of Egypt's pyramids in 2017, notably the Great Pyramid, which led to the discovery of a new large chamber above the Great Gallery [20]. The same year marked the start of the MEV project, aiming to design and test a new high-resolution telescope for muography of Etna Volcano [21].

In 2019, U.S. Customs and Border Protection partnered with Decision Sciences to pilot the Discovery™ scanning system at a major port of entry, revealing its superior capability in accurately detecting anomalies [22]. Lastly, in 2023, the first 3D imaging of a whole nuclear reactor was obtained using the largest set of muography projections ever made in this field [23], and cosmic-ray muon radiography detected a large void and a smaller unidentified void in the Great Pyramid, along with a hidden corridor near its main entrance [24].

1.2.2 Principles of Muography

The technique of muography can be broadly classified into two types, based on the fundamental principles at work: absorption muography and scattering muography.

Absorption Muography

Absorption muography, also known as transmission muography, is the more traditional approach. It operates on the principle of measuring the intensity of muon flux after passing through an object (also called one-sided muography) as shown in Figure 1.3. Since muons are absorbed and scattered as they traverse through matter, variations in the flux intensity can be used to infer the density and structure of the object being studied. A higher muon flux corresponds to less dense or thinner regions, while a lower muon flux indicates denser or thicker regions. The intensity of the cosmic muons can be represented by the measured count rate. If we consider R_0 as the count rate of muons in a detector before the region of interest and R as the count rate after passing through the absorbing medium, we obtain:

$$R = R_0 e^{-\mu x} \tag{1.7}$$

If the count rate and the thickness of the absorber are measured, the absorption coefficient can be determined from the slope obtained after fitting the linear equation,

$$\ln(R) = \ln(R_0) - \mu x \tag{1.8}$$

This equation can be used to experimentally determine the absorption coefficient. The fitting adapted is the least square technique [25]. This method is often employed in applications where the target is huge such as volcano imaging and pyramid exploration, where it is used to investigate the internal structure based on the differences in muon absorption.

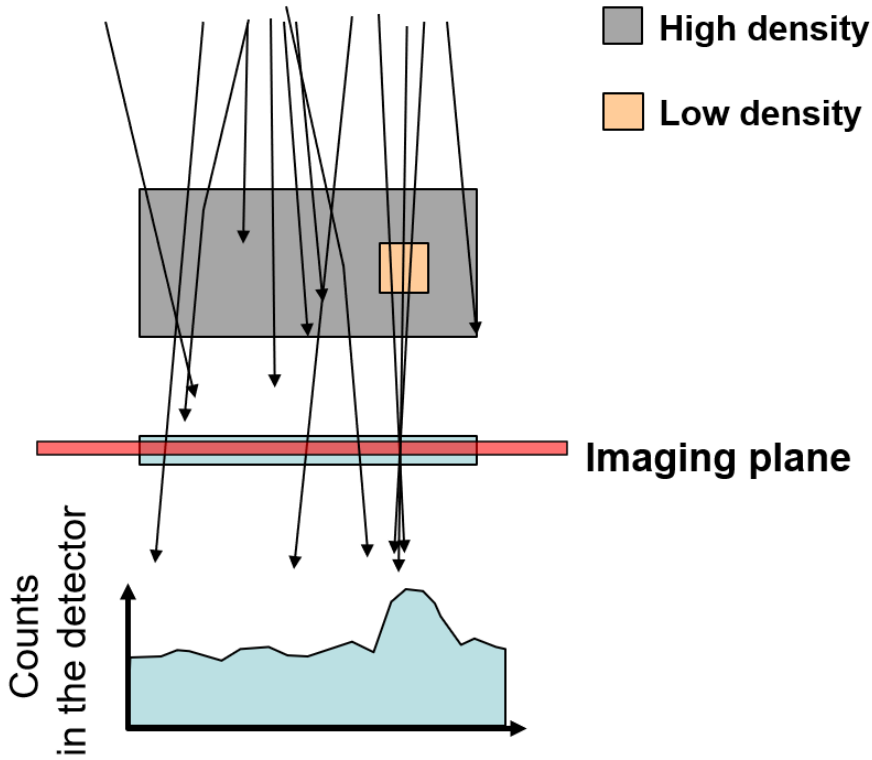

Fig. 1.3: Absorption muography method.

Scattering Muography

Scattering muography is based on the measurement of the scattering angles of muons as they pass through an object. Here the target is sandwiched between two sets of muon position sensitive detectors (also called two-sided muography) and by comparing the information of incoming muons and out going muons the information of the target is revealed. Figure 1.4 shows a conceptual design of muon scattering method. As muons interact with atomic nuclei, they are deflected off their initial trajectory. By tracking these deflections, one can reconstruct the path of the muon and, consequently, gain information about the material properties of the object the muons have traversed.

This method is especially effective in detecting high-Z (high atomic number) materials because the scattering of muons is more pronounced when they interact with larger nuclei. This property makes scattering muography an effective tool for applications such as security screening and detection of nuclear materials. In the following we will investigate the scattering of muons in detail.

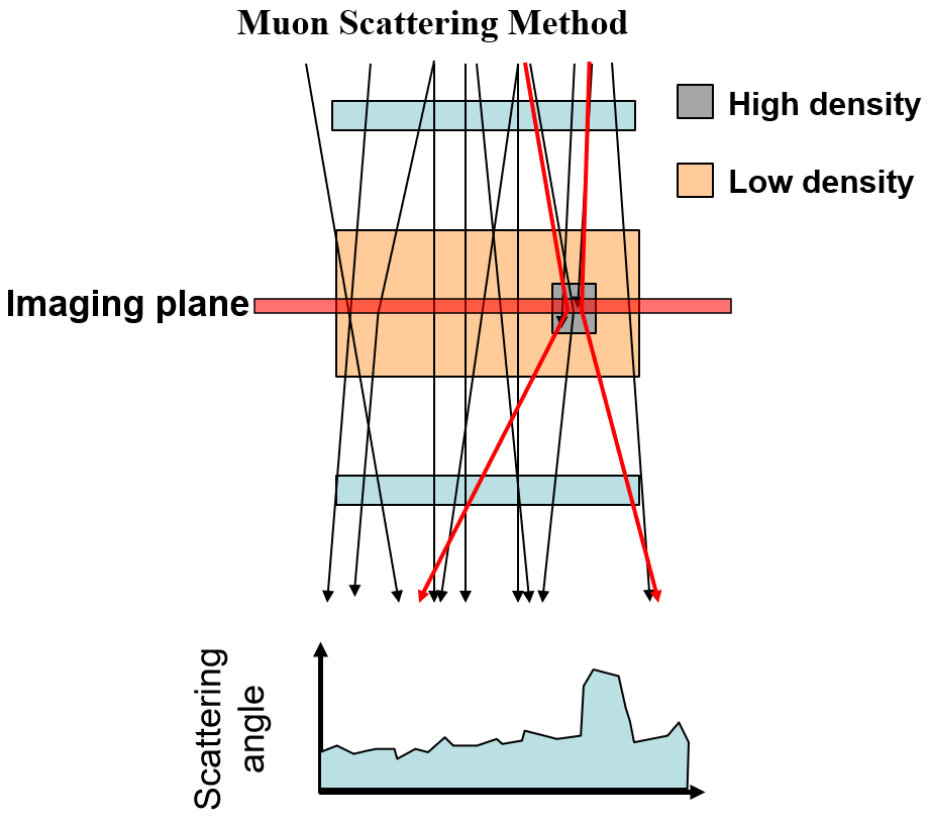

Fig. 1.4: Scattering muogaphy method.

Muon Multiple Scattering

Multiple scattering is a phenomenon that occurs when muons traverse through matter. As muons pass through a material, they continuously interact with the atomic nuclei , leading to a sequence of deflections in their trajectory. The extent of these deflections is not only influenced by the density of the material but also the atomic number (Z) of the material. In particular, materials with a high atomic number tend to cause larger deflections as shown in Figure 1.5 the expected scattering angle for uranium is higher than iron.

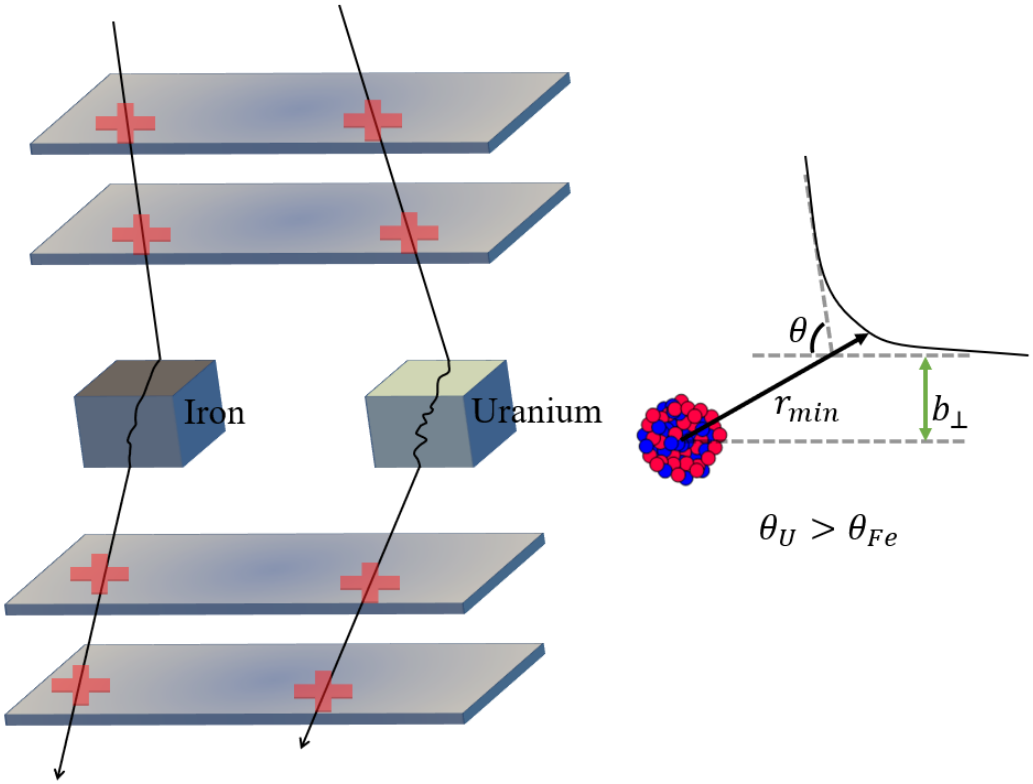

Fig. 1.5: Muon multiple scattering.

The distribution of the scattering angles follows a Gaussian distribution centered around the initial trajectory of the muon. In the next section we well investigate the scattering angle of muons.

1.2.3 Muography Detectors

Muon detectors are very important in muography. They help us to find muon's flux, their position and direction. The design, functionality, and effectiveness of these detectors strongly influence the resolution and overall quality of the final data produced by muography. Despite the low event rates inherent to muon imaging, these detectors remain robust, cost-effective, and durable, attributes that significantly contribute to their usage.

There are mainly three types of detectors employed in muography; scintillator detectors, gaseous detectors, and emulsion detectors. Each category has its strengths and potential applications, which have been discussed below.

Scintillator Detectors

There are different type of scintillator based detetors but plastic scintillators are predominantly used in muography due to their unique set of advantages. These devices are physically robust, relatively easy to manufacture and deploy, and provide reliable performance. When a muon interacts with the material within a scintillator, it imparts energy to the atoms present, leading to the emission of light. This light is subsequently collected using photomultiplier tubes or silicon photomultiplier(SiPM), which convert the light into an electrical signal. This signal can then be processed and analyzed to determine the trajectory and energy of the incident muon, thus providing valuable information about the muon flux. Figure 1.6 represents a plastic scintillator based muography detector.

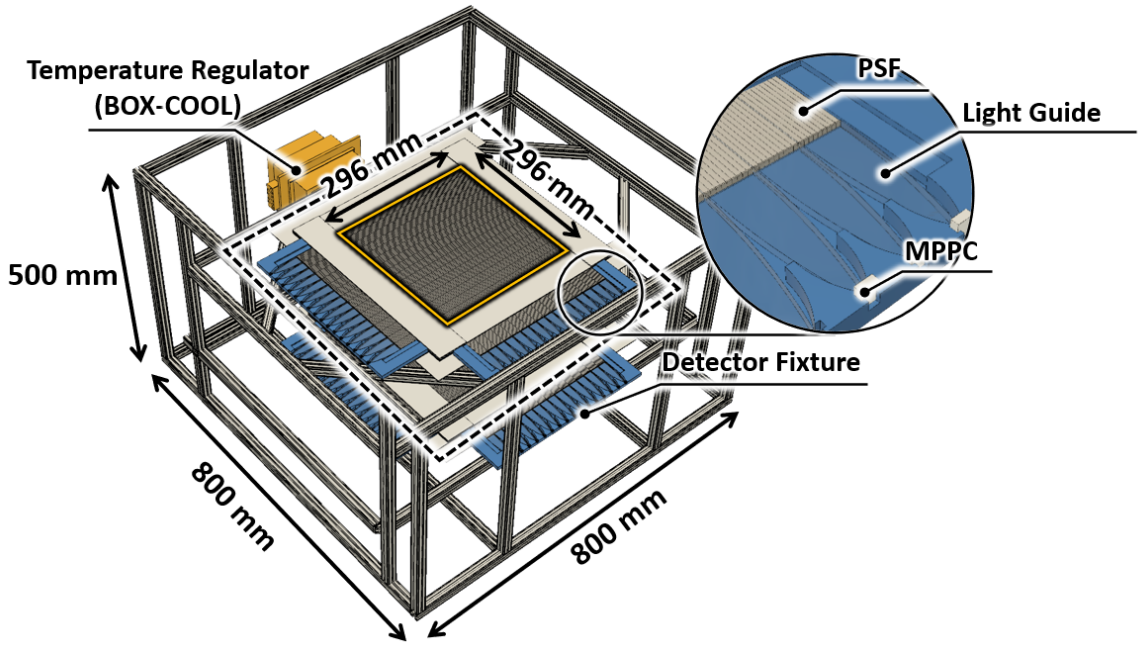

Fig. 1.6: A plastic scintillator based muography detector.

Gaseous Detectors

Gas detectors function through ionization, where a beam of particles passing through a gas causes the generation of ion-electron pairs. These detectors typically comprise two electrodes filled with gas. As a charged particle, such as a muon, travels through this gas-filled space, it loses energy, inducing a current in the electrodes that can be measured or converted into a pulse to count individual particles. Drift tubes and Resistive Plate Chambers (RPCs) represent two types of gaseous detectors employed in muography. Drift tubes consist of an array of gas-filled tubes, placed in parallel. When a muon traverses one of these tubes, it ionizes

the gas molecules along its path, liberating electrons. These free electrons drift towards an anode, usually a wire running along the center of the tube, under the influence of an electric field. The movement of these electrons induces an electrical signal that is then recorded and processed. Similarly, RPCs are made up of two parallel plates, usually composed of glass or plastic, separated by a gap filled with gas. When a muon passes through this gas-filled gap, it ionizes the gas, creating a trail of charged particles. An electric field applied across the gap causes these charged particles to move, generating a strong electronic signal. Both drift tubes and RPCs allow for the accurate determination of the muon's position and trajectory, hence enabling precise imaging.

Emulsion Chambers

Emulsion films, also known as nuclear emulsions, offer an alternative approach to muon detection. These films consist of a layer of photographic emulsion that is sensitive to charged particles. As a muon passes through the emulsion, it causes the silver halide crystals present in the emulsion to darken, leaving a visible trace of its path. These traces can be developed and studied under a microscope to precisely reconstruct the path of the muon. The high spatial resolution offered by emulsion films makes them particularly valuable for applications where fine detail is necessary, such as geologic or archeological investigations.

1.2.4 Muography Application Areas

Muography offers significant potential in diverse fields as a cutting-edge imaging technique that harnesses naturally occurring cosmic muons to examine the internal structure of various structures. Below are the major applications of muography categorized under different fields. Figure 1.7 shows variety of muon applications.

Geophysics and Volcanology

- **Volcano Monitoring:** By mapping the interior structure of volcanoes, muography can help understand volcanic processes and forecast eruptions. The high-energy muons can penetrate the dense structure and provide insights into magma chambers, lava tubes, and fault lines.
- **Exploration of Natural Resources:** Muography can be used to detect and quantify underground mineral deposits, oil reserves, or groundwater reservoirs. It allows for non-invasive, eco-friendly exploration which is crucial in protecting our environment.

Civil Engineering and Construction

- **Infrastructure Inspection:** The technique allows us to visualize the interior of large civil structures like bridges, dams, and buildings, providing valuable data about their structural integrity. This can be crucial in assessing safety and planning maintenance or reconstruction efforts.
- **Tunnel and Cavern Monitoring:** Muography can be used to inspect the safety of tunnels and caverns, or to map their uncharted regions. This can be especially important in mining or underground transportation.

Archeology and Cultural Heritage

- **Examination of Archaeological Structures:** Muography can help explore the internal structure of archaeological sites without causing any damage. For instance, it was used to investigate the Great Pyramid of Giza, revealing an unknown chamber.
- **Preservation of Cultural Heritage:** By detecting structural issues in historical monuments, muography can help in their preservation.

Security and Defense

- **Border Security:** Muography can be used for scanning large cargo containers to detect contraband or illicit materials.
- **Nuclear Safety and Non-proliferation:** It can be used to detect and monitor hidden nuclear materials in a non-invasive manner, aiding nuclear safety and treaty verification efforts.

Astrophysics

- **Cosmic Ray Studies:** Muography also finds its application in understanding cosmic rays and the universe. Muons are by-products of cosmic rays interacting with Earth's atmosphere, and their study provides valuable information about these high-energy particles from outer space.

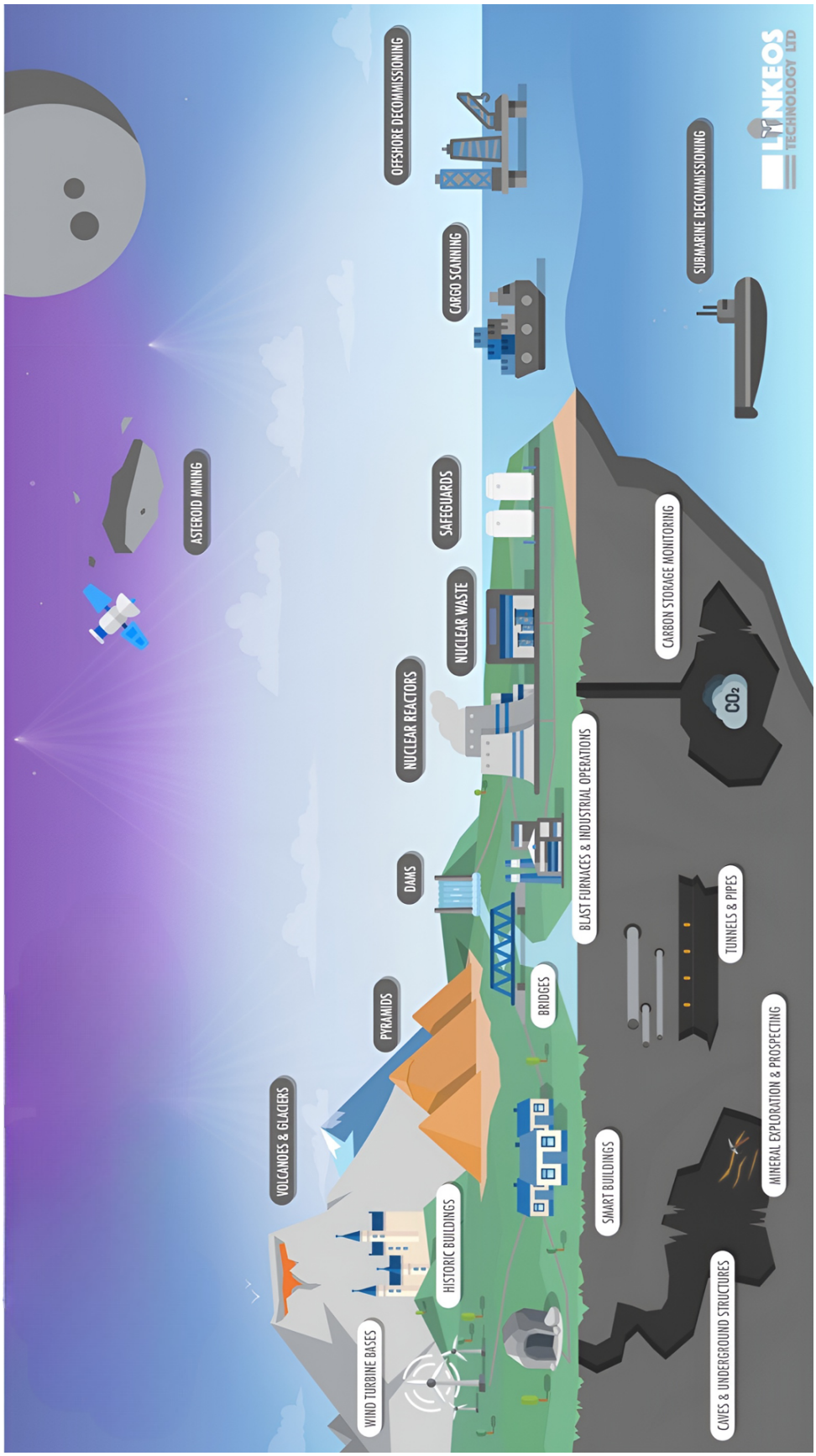

Fig. 1.7: Application of muography (Image by Lynkeos).

1.3 Magnetic Field Measurement Techniques

The capacity to accurately measure magnetic fields is paramount to a plethora of scientific, industrial, and technological endeavors. Ranging from the operation of electric motors and generators to geophysics, particle physics, medical imaging, and space exploration, the influence and utility of magnetic fields are far-reaching. Accordingly, multiple techniques have been developed over the years for the precise measurement of these fields, each technique being uniquely equipped to deal with the task but also accompanied by its own set of limitations. In the following, we provide an overview of the various techniques currently in use for magnetic field measurement.

Hall-Effect Sensors: These sensors measure the magnetic field intensity via the Hall effect. This phenomenon induces a voltage difference across an electrical conductor in response to an electric current in the conductor and a perpendicular magnetic field. The Hall voltage, which is proportional to the magnetic field strength, can then be measured. *Limitations*: The precision of Hall-effect sensors can be compromised by offset drift and sensitivity changes due to temperature fluctuations.

Coil Magnetometers: These devices, often referred to as search coils, operate based on Faraday's law of electromagnetic induction. When a magnetic field changes within a coil of wire, it induces an electromotive force (EMF), which generates a current. The strength of the magnetic field is determined by measuring this current. *Limitations*: Coil magnetometers can be influenced by temperature variations and are susceptible to external electromagnetic interference, requiring careful shielding. They are also more effective at measuring alternating magnetic fields than static ones.

Fluxgate Magnetometers: These devices measure magnetic fields using the nonlinear properties of magnetic materials. A small AC current is driven through a primary coil wound around a magnetically saturable core. An external magnetic field alters the core's saturation pattern, inducing a signal in a secondary coil that can be analyzed to determine the strength of the magnetic field. *Limitations*: Fluxgate magnetometers tend to be large, power-hungry, and require careful calibration. They also have limited frequency response.

Superconducting Quantum Interference Device (SQUID) Magnetometers: SQUIDs are highly sensitive detectors of magnetic fields. They operate based on principles of quantum mechanics and superconductivity. A SQUID consists of two superconductors separated by thin insulating layers, forming two parallel Josephson junctions. Changes in the magnetic field induce changes in the phase difference across the junctions, which are converted to voltage for measurement. *Limitations*: SQUIDs require ultra-low temperatures to maintain superconductivity, shielding from external noise, and are complex and not easily portable.

Spin Exchange Relaxation Free (SERF) magnetometers: SERF magnetometers detect magnetic fields by exploiting spin-exchange relaxation-free conditions in a dense alkali metal vapor. The magnetic field influences the spin precession of the alkali atoms, which can be detected optically. *Limitations*: SERF magnetometers are sensitive to environmental conditions and require controlled light and temperature. They are also relatively expensive and need careful handling.

Optically Pumped Magnetometers (OPM): OPMs are quantum sensors that measure magnetic fields by monitoring the behavior of specific atoms under a magnetic field and optical pumping. The magnetic field influences the orientation of atomic spins, which alters the absorption of polarized light. This interaction provides a means to measure the magnetic field. *Limitations*: OPMs require controlled conditions for optimal performance, and their sensitivity is highly dependent on the atomic species used and the intensity of the pump light. The required atomic vapor cell is fragile and susceptible to environmental influences.

1.4 Study Objectives

Despite the impressive capabilities of the current magnetic field measurement techniques, they come with certain limitations that necessitate the exploration of alternative approaches. One such promising alternative is using cosmic-ray muons. The primary objective of this study is to investigate the feasibility of a novel application of cosmic-ray muons or muography for the detection, imaging and the measurement of magnetic fields. Despite the significant progress and potential exhibited by muography in various applications, its use in detecting magnetic fields remains largely unexplored. This thesis aims to fill this gap in knowledge and contribute to the ongoing advancements in the field. The main focus of this thesis is to perform a feasibility study on magnetic field measurement and detection as a novel application of cosmic-ray muons. We named the proposed technique "Magnetic Field Imaging by Cosmic-ray Muon – Magic-μ –.

Cosmic-ray muons, with their unique characteristics, are proposed as potential tools for magnetic field measurement. This proposal is built upon the premise that muons, being charged particles, exhibit deflection when moving through a magnetic field - a behavior that can potentially be exploited for magnetic field detection. Furthermore, this study also aims to explore the impacts of magnetic fields on muography-based inspection systems, an aspect that has been largely overlooked in previous studies.

For magnetic field measurement, muography brings several advantages and disadvantages. On the upside, cosmic-ray muons serve as a cost-effective and inexhaustible source for magnetic field imaging. Their ability to penetrate dense structures and the ground allows

for magnetic field measurements in locations previously deemed unreachable. Muography's wide field of view facilitates large-scale magnetic field measurements, and its autonomous detection does not require artificial sources or close proximity to the measurement site. Furthermore, the deflection of muons due to the Lorentz force can be measured and utilized to infer the magnetic field's strength.

However, muography isn't without its shortcomings. Extracting meaningful insights from muon data requires complex statistical and computational methods. Despite its broad field of view, the spatial resolution of muography falls short compared to traditional techniques. Measurement accuracy can also suffer due to high background noise caused by muon interactions before and after reaching the detector. Moreover, the muon flux, which influences data interpretation, is susceptible to variations due to factors like altitude, atmospheric conditions, and solar activity. Finally, collecting a statistically significant amount of data may require extensive measurement periods due to the relatively low flux of cosmic-ray muons.

In summary, while traditional techniques present unique strengths and weaknesses, muography emerges as a promising frontier in the magnetic field measurement field. Although currently facing certain challenges, continuous research and technological improvements are steadily enhancing muography's feasibility and applicability, pitting it as a potential competitor to existing techniques.

1.5 Overview of the Thesis

Chapter 1 provides an in-depth look into the phenomenon of cosmic-ray muons and their creation processes. It introduces muography, describing its historical evolution, principles, detectors, and applications. Additionally, it gives an overview of the methods currently are being used for measuring magnetic fields. The chapter ends with defining the study objectives and providing an overview of the thesis.

In Chapter 2, the methodology is discussed, delving into the motion of muons in a magnetic field and the models for cosmic-ray spectrums, including the PARMA model. This chapter also explores the interactions of muons with matter and presents the tools used for particle transport.

Chapter 3 focuses on magnetic field muography detectors. It describes and analyzes the transmission and deflection methods proposed for the magnetic field studies using cosmic-ray muons, detailing the specific techniques and considerations for designing detectors, and analyzing methods.

Chapter 4 presents feasibility simulations for the transmission and deflection methods in magnetic field studies. It further delves into the proposed methods for the estimation of magnetic flux density and concludes with a summary of the simulation results.

In the final chapter, Chapter 5, the main findings are summarized, and recommendations for future research are proposed. This chapter ends with concluding remarks that restate the importance and potential of this research area.

This thesis endeavors to highlight the potential and complexity of using cosmic-ray muons for magnetic field detection and measurement.It points out that this is a difficult task, but it's feasible and it's very important to keep researching it because it's an exciting area with lots of potential.

Chapter 2

Methodology

Chapter 2 offers an in-depth view of the research methodology applied in this study. It explains the theoretical foundations of muon interactions with magnetic fields, and the conceptual design for detecting and measurement of magnetic field using cosmic-ray muons.

2.1 Muons Motion in a Magnetic Field

When a charged particle moves through an electromagnetic field, it experiences a force that acts perpendicular to both its direction of motion and the magnetic field as shown in Figure 2.1.

This force, known as the Lorentz force, influences the particle's trajectory without changing its speed. For instance, if a muon that carries a charge q and moves with a velocity $\vec{v}$ in an electric field $\vec{E}$ and a magnetic field $\vec{B}$, the Lorentz force $\vec{F}$ is defined as:

$$F = q(\vec{E} + \vec{v} \times \vec{B}) \tag{2.1}$$

Considering a situation where there is no electric field ($\vec{E} = 0$), the Lorentz force equation reduces to:

$$F = q\vec{v} \times \vec{B} \tag{2.2}$$

As the average energy of muons is around 4 GeV, we must apply the relativistic equations for them. In the case of relativistic velocities, we need to take into account the velocity dependence of the relativistic mass, given by $m_{\text{rel}} = \gamma m$, where $\gamma = (1 - v^2/c^2)^{-1/2}$. The equations of motion then become:

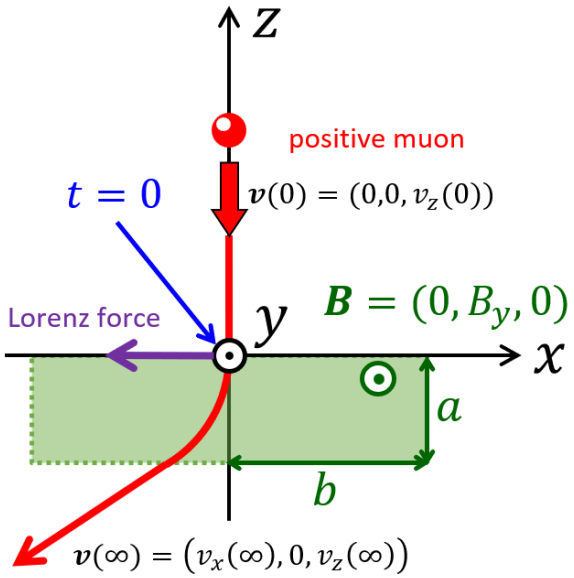

Fig. 2.1: A positive muon crossing a magnetic field.

$$\frac{d(\gamma m\vec{v})}{dt} = q\vec{v}\times\vec{B} \tag{2.3}$$

For a uniform magnetic field $\vec{B} = (0, B_y, 0)$ and initial velocity $\vec{v} = (0, 0, -v_z(0))$, the equation of motion for each element of Cartesian coordinate becomes:

$$\frac{dv_x}{dt} = \frac{-qv_zB_y}{m\sqrt{1-\frac{v_z^2(0)}{c^2}}} \tag{2.4}$$

$$\frac{dv_y}{dt} = 0 \tag{2.5}$$

$$\frac{dv_z}{dt} = \frac{qv_xB_y}{m\sqrt{1-\frac{v_z^2(0)}{c^2}}} \tag{2.6}$$

which gives:

$$x(t) = -r\cos(\omega t) \tag{2.7}$$

$$z(t) = r\sin(\omega t) \tag{2.8}$$

where:

$$\omega \equiv \frac{qB_y}{m\sqrt{1-\frac{v_z^2(0)}{c^2}}} \tag{2.9}$$

The Larmor radius is defined as:

$$r \equiv \frac{v_z(0)}{\omega} = \frac{mv_z(0)}{qB_y\sqrt{1-\left(\frac{v_z(0)}{c}\right)^2}} \tag{2.10}$$

and in these equations $v_z(0)$ can be calculated using:

$$v_z(0) = c\sqrt{1-\left(\frac{mc^2}{E+mc^2}\right)^2} \tag{2.11}$$

As a result, the muon describes a circular path in a plane perpendicular to the magnetic field. These equations reveal that the charged particle will execute circular motion in the $x-z$ plane under the influence of a uniform magnetic field in the y-direction. Since the force is always perpendicular to the velocity, the magnetic field does not do work on the muon, and the energy (and therefore speed) of the muon remains constant. Consequently, the muon's path describes a helix along the direction of the magnetic field. The radius r of the helix is described as Larmor radius and the period T of the muon's motion are given by:

$$T = \frac{2\pi\gamma m}{qB} \tag{2.12}$$

where γ is Lorentz factor and defined as:

$$\gamma = \frac{1}{\sqrt{1-\frac{v^2}{c^2}}} \tag{2.13}$$

The pitch h of the helix, the distance the muon travels along the direction of $\vec{B}$ in one period, is given by:

$$h = v_{\parallel}T = \frac{2\pi\gamma m v_{parallel}}{|q|B} \tag{2.14}$$

where $v_{\parallel}$ is the component of $\vec{v}$ parallel to $\vec{B}$.

The deflection angle of muons is defined as the difference between the outgoing and incoming angles, and it can be calculated using Eq. 2.15.

$$\Delta\theta = \frac{qBL}{p_{\perp}}, \tag{2.15}$$

where $\Delta\theta$ is the deflection angle, q is the muon's charge, B is the magnetic flux density, L is the distance over which the magnetic field is applied, and p is the muon's momentum.

To gain a more comprehensive understanding of how muons can be deflected within a magnetic field, we have conducted a series of simulations. These experiments examine muons of varying energies interacting with magnetic fields of 0.5 T and 5 T strengths with a thickness of 20 cm. The results of these simulations are represented in the following graphs:

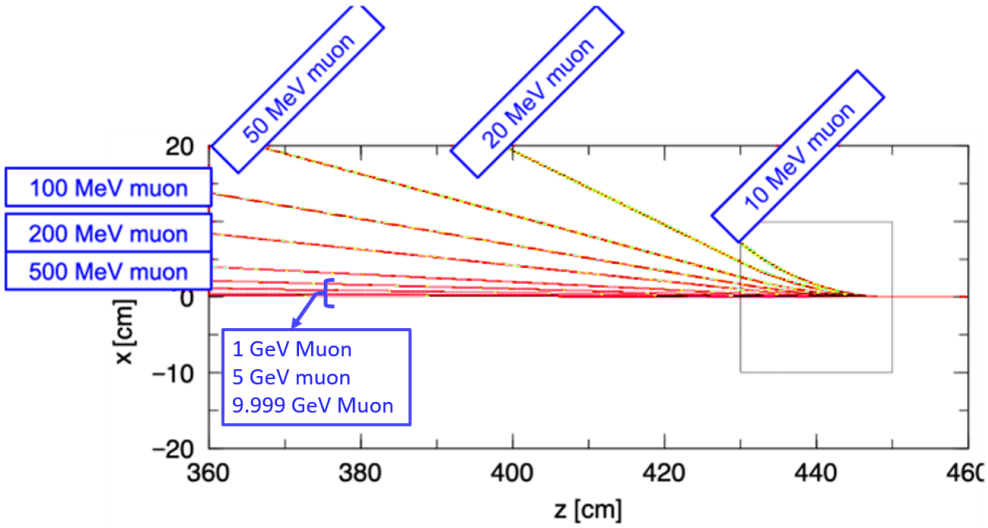

Fig. 2.2: Muons of various energies interacting with a 0.5 T, 20 cm thick magnetic field.

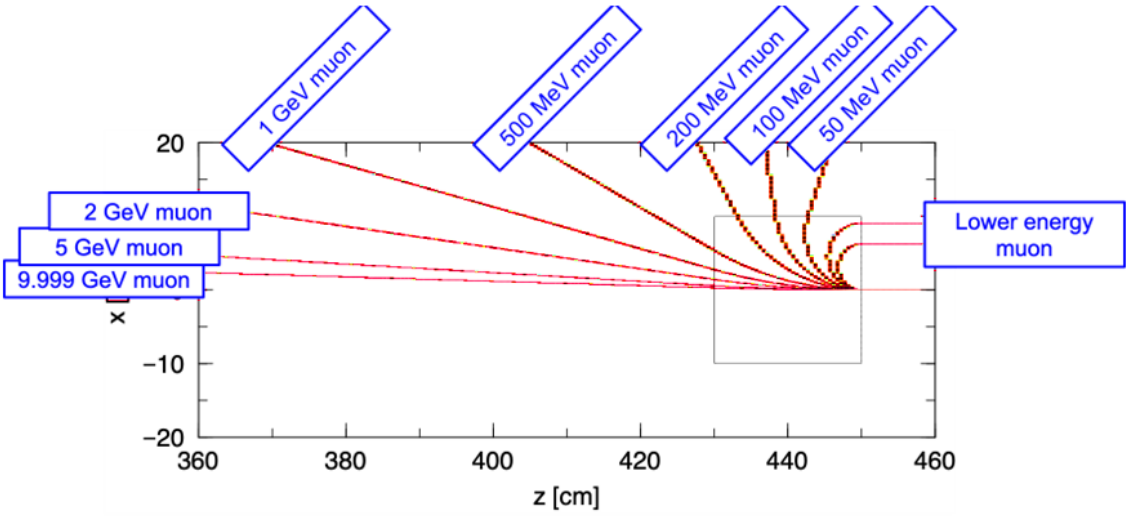

Fig. 2.3: Muons of various energies interacting with a 5 T, 20 cm thick magnetic field.

Utilizing the same principles found in absorption muography, we can not only detect but also image magnetic fields, particularly when they exhibit significant strength. To compare the effect of magnetic field on positive and negative muons, a magnetic region of vacuum with a size of 300 cm $\times$ 100 cm $\times$ 100 cm and a magnetic flux density of 500 mT was defined. A 1 GeV muons were generated in surface source of positive and negative muons was generated, and the track of the muons was investigated. Figures 2.4a and 2.4b represent the changes in the muon tracks due to the magnetic field for negative and positive muons, respectively. This proposes the idea of charge identification using a known magnet.

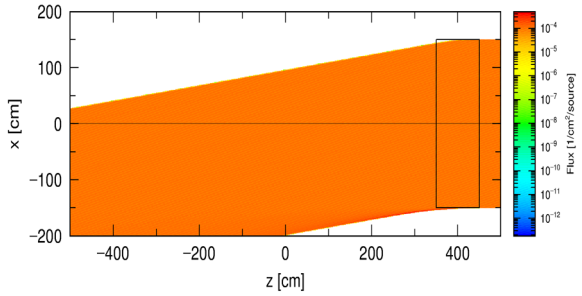

(a) Negative muons

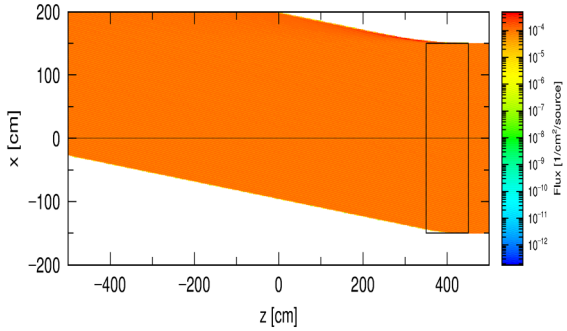

(b) Positive muons

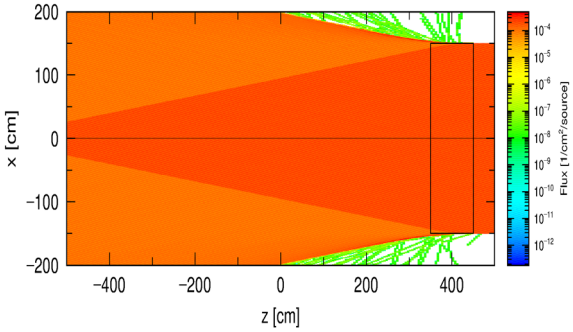

(c) Positive and negative muons

Fig. 2.4: Effect of a 500 mT magnetic field on the tracks of 1 GeV muons.

2.2 Cosmic-Ray Spectrum Models

The energy spectrum of cosmic ray muons at sea level varies over several orders of magnitude, from approximately 10 MeV to 10 GeV. Figure 2.5 was generated using EXPACS [26], and assumes a latitude of 38°. Integrating this curve with respect to energy suggests a total muon flux of $1.56 \times 10^{-2}, \mathrm{cm}^{-2}, \mathrm{sec}^{-1}$, which is in agreement with the often quoted value of $10,000, \mathrm{m}^{-2}, \mathrm{min}^{-1}$.

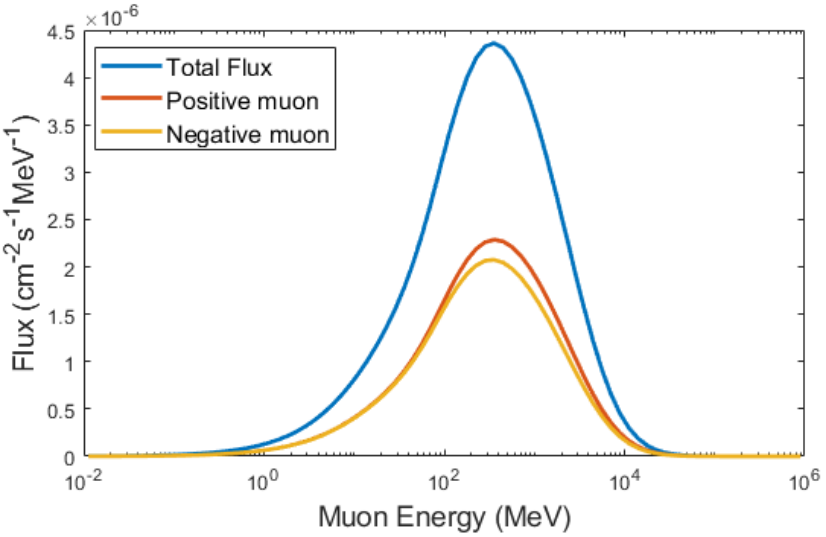

Fig. 2.5: Energy spectrum of cosmic ray muons at sea level.

According to Particle Data Group [27], the approximated vertical flux of muons having momentum greater than 1 GeV/c, is estimated around 70 muons for each square meter every second for every steradian. The vertical differential cosmic ray muon momentum spectrum at sea level, ranging from 0.2 to 10 GeV/c, is depicted in Figure 2.6 [28].

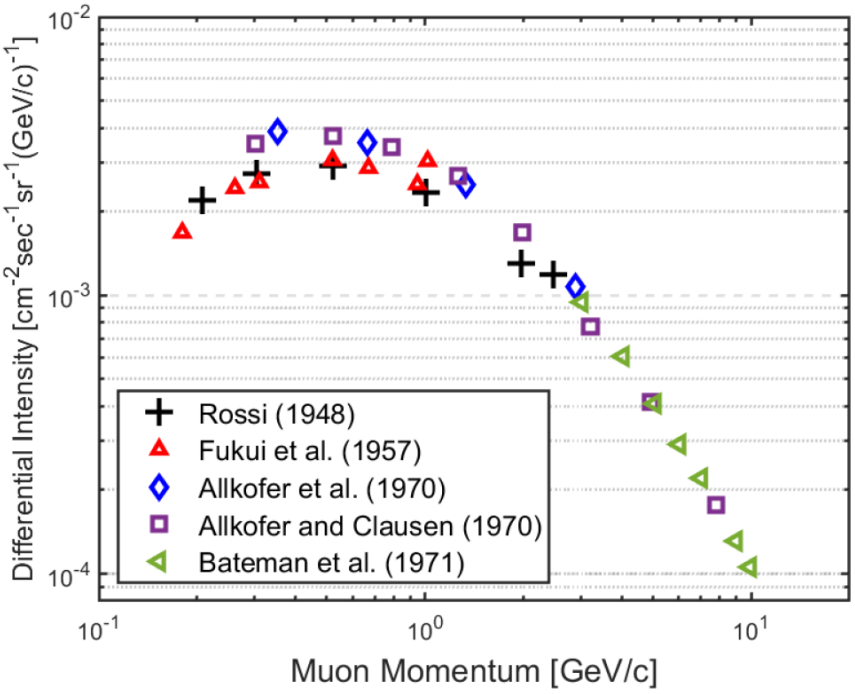

Fig. 2.6: Vertical differential cosmic ray muon momentum spectrum in the range of 0.2–10 GeV/c.

While the muon intensity is influenced by various factors such as longitude, azimuthal angle, Earth's movement in the universe, and solar activity, its variance is not significant when compared to the dependency on the zenith angle. In situations when the zenith angle is low ($\theta < 70°$), the muon energy spectrum can be calculated using the Gaisser formula, given as follows [27]:

$$\frac{dN_\mu}{dE_\mu d\Omega} \approx \frac{0.14E_\mu^{-2.7}}{cm^2 \text{ s sr GeV}} \times \left\{ \frac{1}{1+\frac{1.1E_\mu \cos\theta}{115GeV}} + \frac{0.054}{1+\frac{1.1E_\mu \cos\theta}{850GeV}} \right\} \tag{2.16}$$

In this formula, E and θ represent the energy of the muon and zenith angle respectively and Ω represents the solid angle. The first and second terms within the brackets account for the contributions from pion and kaon decays, which are integral in the generation of the muon flux. This highlights the role of secondary interactions in atmospheric cascades in shaping the muon energy spectrum.The atmospheric muons flux depends on the zenith angle, θ following a cosine-power law as follwos[29]:

$$f(\theta, h_v, E) = f(0^o)\cos^{n(h_v,E)}(\theta) \tag{2.17}$$

Here, θ is the zenith angle, h_v is vertical length of the muon path, $f(0^o)$ is the vertical muon intensity. The exponent, n (h, E), is a function of the muon energy, E, and vertical length of the muon path, h and at sea level, $n \approx 2$. Figure 2.7 shows the zenith angle distribution of cosmic ray muons at sea level in the range of 0 to 89°[28].

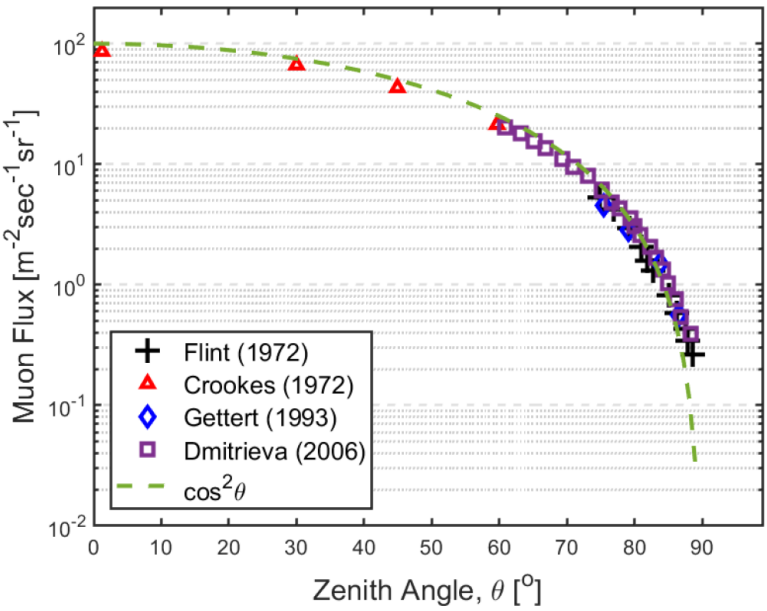

Fig. 2.7: The variation of cosmic ray muon flux with zenith angles in the range of 0 – 89° at sea level.

The azimuth angle distribution, under the assumption of isotropy (i.e., that cosmic rays arrive from all directions with equal probability), would be uniform. However, in reality, it is influenced by the Earth's magnetic field, which can deflect incoming cosmic rays and introduce a degree of anisotropy. There are some models and tools for modeling cosmic-ray that we will investigate in the following subsections.

2.2.1 PARMA Model

The PARMA (Parameterization of the primary cosmic-ray energy spectrum with the global multi-responses) model is an analytical approach primarily utilized to estimate the energy spectrum of cosmic rays over a broad energy range. This model has been developed in response to the necessity of accurately portraying the highly complex interactions of cosmic rays within the Earth's atmosphere [30]. Despite the inherent complexities and uncertainties in cosmic-ray simulations, the PARMA model has demonstrated the capability to effectively simulate the behavior of different types of primary cosmic rays. Its adaptability extends

to various experimental setups and atmospheric conditions, making it a versatile tool in this domain. The PARMA model can be utilized by EXPACS, which stands for "EXcel-based Program for calculating Atmospheric Cosmic-ray Spectrum", is a program capable of immediate computation of various cosmic ray fluxes on Earth. This includes neutrons, protons, ions with charge up to 28 (Ni), muons, electrons, positrons, and photons almost at any time and place within Earth's atmosphere. Furthermore, using the derived cosmic-ray fluxes, EXPACS can calculate the effective dose, ambient dose equivalent, and absorbed dose in air, which all pertain to cosmic-ray exposure.

2.2.2 CORSIKA (COsmic Ray SIMulations for KAscade)

CORSIKA is a Monte Carlo program explicitly designed for the theoretical modeling and simulation of the development of Extensive Air Showers (EAS) when high-energy primary particles (like photons, protons, and nuclei) enter the atmosphere. Developed to address the complexities in analyzing experimental data on EAS or planning corresponding experiments, CORSIKA incorporates the physics and data from several established program systems to not only provide accurate average values of observables but also to reproduce the correct fluctuations around these averages. It includes all known processes that could significantly influence EAS's observable quantities, covering particle transport through the atmosphere and their interactions with air as a target. Since its inception in 1989, CORSIKA has undergone numerous enhancements and extensions, incorporating several different hadronic interaction models to simulate high-energy interactions, managing fragmentation of nuclei in collisions, photoproducing muon pairs and hadrons, and calculating photon-induced showers' muon content. It also considers factors like the atmospheric elemental composition, density variation with altitude, and the Earth's curvature effect on atmospheric density profiles. The continuous development of CORSIKA is encouraged, and the user community's feedback on improvements, error rectifications, or assumptions' reservations is actively solicited. [31].

2.2.3 CRY

The CRY software library is designed to generate correlated cosmic-ray particle shower distributions at three different elevations (sea level, 2100 m, and 11300 m), acting as input for transport and detector simulation codes. The simulation relies on precomputed input tables derived from comprehensive MCNPX simulations of primary cosmic rays interacting with the atmosphere, and it's benchmarked against published cosmic-ray measurements. It provides the production of all particles (muons, neutrons, protons, electrons, photons, and pions) with the correct flux within a user-specified area and altitude. The code generates

individual showers of secondary particles, sampling energy, time of arrival, zenith angle, and multiplicity with basic correlations, and includes user controls for latitude (geomagnetic cutoff) and solar cycle effects. The software library can be used with C, C++, and Fortran, and offers interfaces to popular Monte Carlo transport codes such as MCNP, MCNPX, COG, and Geant4 [32]

2.3 Interaction of Muons with Matter

Both positive and negative muons are subject to electromagnetic and weak interactions. When a charged particle like a muon interacts with matter, it can do so through electrical, nuclear, or gravitational forces. However, due to the negligible effect of gravitational forces in this context, we focus on the contributions of the electrical and nuclear interactions to the stopping power. For muons specifically, the various mechanisms contributing to energy loss encompass ionization processes (which involve atomic excitation and electron collisions), bremsstrahlung radiation, direct electron-positron pair production, and photonuclear interactions. The energy loss of a muon can be mathematically represented as:

$$-\frac{dE}{dx} = a_{\text{ion}}(E) + \left[b_{\text{br}}(E) + b_{\text{pp}}(E) + b_{\text{ni}}(E)\right]E \tag{2.18}$$

In this equation, the first term represents energy loss due to ionization and atomic excitation which exhibits a weak logarithmic dependence on energy. In certain approximations, particularly when considering muon energy loss in the semi-relativistic regime, this term can be assumed to be nearly constant. The coefficients $b_{\text{br}}(E)$, $b_{\text{pp}}(E)$, and $b_{\text{ni}}(E)$ denote the energy losses due to bremsstrahlung radiation, electron-positron pair production, and photonuclear interactions, respectively. Each of these coefficients is associated with complex energy-dependent mathematical relationships.

For illustrative purposes, Table 2.1 and Figure 2.8 will compare these coefficients for six distinct muon energies when interacting with iron [33] as it is similar to permanent magnets.

Ionization

The ionization process dominates muon interactions. As a muon traverses a material, it ionizes atoms having collision with electrons. The ionization cross section of a muon incident on an atom of atomic number Z, representing the probability of an ionization event occurring, is given by[28]:

Table 2.1: Energy loss of muons for different energies in iron

	dE/dx (GeV g^{-1} cm^{-2})				
Muon Energy (GeV)	$a_{\text{ion}}(E)$	$b_{\text{br}}(E)$	$b_{\text{pp}}(E)$	$b_{\text{ni}}(E)$	Total
1,000	2.45E-3	2.87E-3	4.19E-3	3.88E-4	9.78E-3
10,000	2.50E-3	3.17E-2	4.52E-2	4.33E-3	8.38E-2
100	2.16E-3	2.24E-4	3.17E-4	3.85E-5	2.74E-3
300	2.25E-3	7.72E-4	1.13E-3	1.14E-4	4.27E-3
10	1.93E-3	1.40E-5	1.49E-5	4.23E-6	1.96E-3
1	1.56E-3	5.84E-7	1.77E-7	4.14E-7	1.56E-3

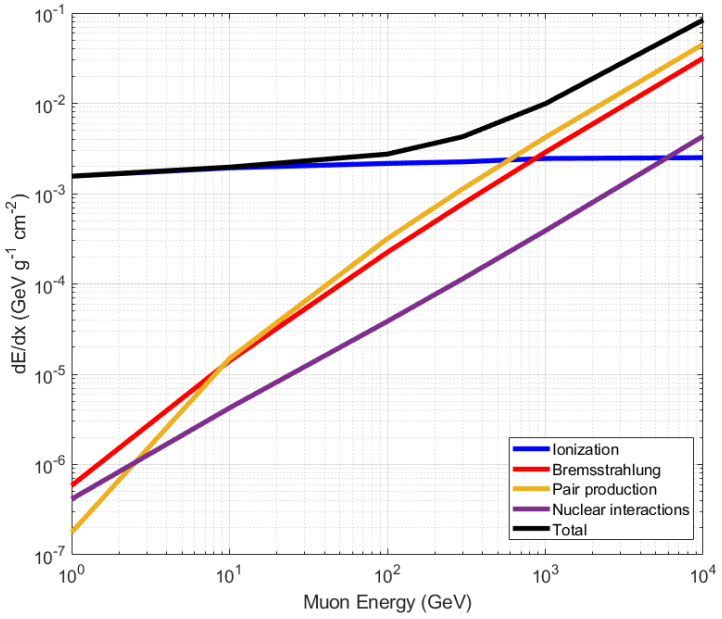

Fig. 2.8: Comparison of muon interactions shares in iron.

$$(\frac{d\sigma}{dv})_{ion} = Z\left(\frac{2\pi r_e^2}{\beta^2 v^2}\right)\left(\frac{m_e}{E_\mu}\right)\left[1-\beta^2\left(\frac{v}{v_{max}}\right)+\frac{v^2}{2}\right] \tag{2.19}$$

Where v_{max} is the maximum fractional energy transfer given by:

$$v_{\max} = \frac{\beta^2}{1+\left(\frac{m_\mu^2+m_e^2}{2m_e E_\mu}\right)} \tag{2.20}$$

The notations, constants, and symbols used in the above formulas are described in Table 2.2. The stopping power, which represents the energy loss of the muon due to ionization, is described by the Bethe-Bloch formula:

$$-\frac{dE}{dx} = Kz^2\frac{Z}{A}\frac{1}{\beta^2}\left[\frac{1}{2}\ln\left(\frac{2m_e c^2\beta^2\gamma^2 T_{\max}}{I^2}\right) - \beta^2 - \frac{\delta(\beta\gamma)}{2}\right] \tag{2.21}$$

Equation 2.21 is valid in the region $0.1 < \beta\gamma < 1000$ with an accuracy of a few percent. Since the energy of cosmic-ray muons falls within this range, the equation is suitable for muography studies. Figure 2.9 depicts the mass stopping power (mean energy loss rate) for a muon as a function of $\beta\gamma$ in various states and materials by using the Bethe-Block equation. As shown in this figure, $< dE/dx >$ is about the same for most materials, decreasing slowly with Z[34].

Table 2.2: Parameters used in and Bethe-Bloch formula.

Parameter	Description
K	Constant
z	charge of the particle (muon)
Z	Atomic number of the medium
A	Atomic mass of the medium
β	Velocity of the muon relative to the speed of light
γ	Lorentz factor (ratio of the total energy of muon to its rest mass energy)
$T_{\max}$	Maximum kinetic energy transfer in a single collision
c	Speed of light
I	Mean excitation energy
N_A	Avogadro's number
m_e	Rest mass of electron
δ	Density effect correction to ionization energy loss

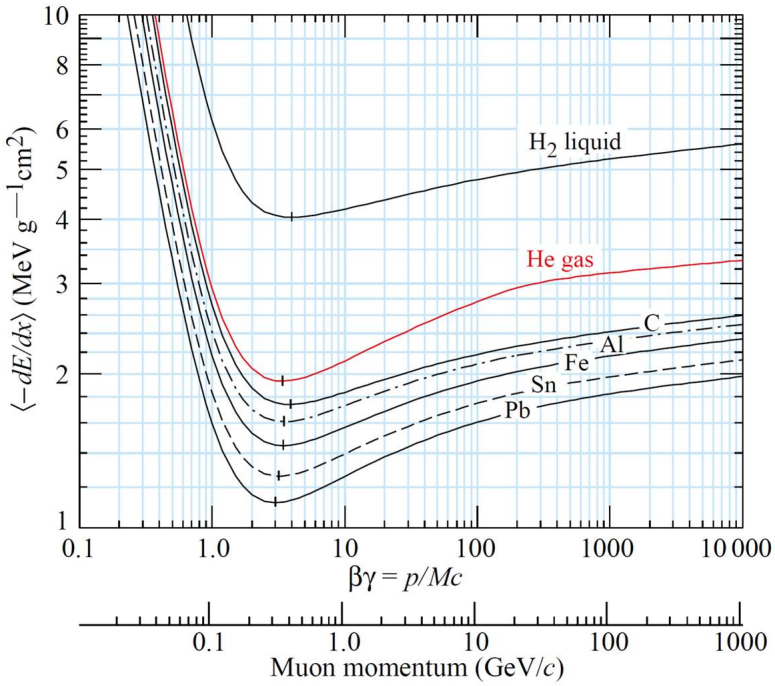

Fig. 2.9: Mean energy loss rate in some materials.

Figure 2.10 shows the mean rate of energy loss, $\langle -dE/dx \rangle$, of a positive muon in copper as a function of muon momentum in GeV/c and $\gamma\beta$. For low energy muons, a nuclear energy loss mechanism dominates whereas a radiative energy loss such as Bremsstrahlung radiation emission dominates in the high energy region. The majority of cosmic ray muon momentum spectrum extends from 0.1 to 100 GeV/c in which "Bethe" region in the figure. In the Bethe region where the Bethe equation is valid, the dominant interaction is ionization. The momentum range of cosmic ray muons has a low mass stopping power including the minimum ionization point.

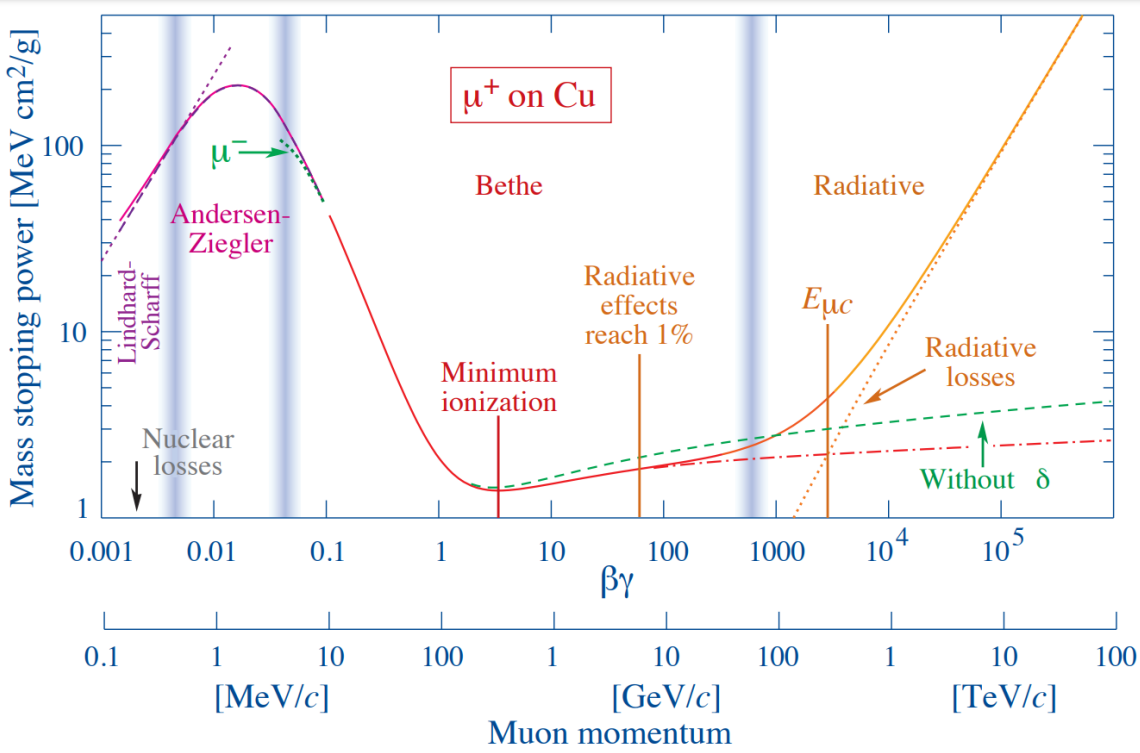

Fig. 2.10: Mass stopping power (= $< -dE/dx >$) for positive muons in copper as a function of $\beta\gamma = p/Mc$ over nine orders of magnitude in momentum (12 orders of magnitude in kinetic energy). The approximated cosmic muon energy range is indicated with vertical blurred lines

The term "minimum ionization particle (MIP)" refers to a particle for which the energy loss per unit path length, is at a minimum. Cosmic ray muons, possessing relativistic speeds at Earth's surface, are generally considered as minimum ionizing particles. Table 2.3 provides a summary of the minimum and maximum energy loss per unit length in different materials within the cosmic muon range. Moreover, the minimum ionization point, $\langle \frac{dE}{dx} \rangle_{\text{min}}$, of the mass stopping power for various materials exhibits a relation with the atomic number, Z. The fitted correlation for $(Z > 6)$ is described as follows:

$$< -dE/dx >_{min} = 2.35 - 0.28 lnZ (Z > 6) \tag{2.22}$$

Bremsstrahlung Radiation

Bremsstrahlung radiation occurs when a muon undergoes acceleration in the electromagnetic field of a target nucleus, causing the emission of a photon. The energy loss due to

Table 2.3: Minimum and maximum energy loss rates of muons for different materials within the cosmic muon energy range (0.1 to 100 GeV/c).

Material	Atomic Number	Density (g/cm^3)	$\Delta E_{\min}$ (MeV/cm)	$\Delta E_{\max}$ (MeV/cm)
H_2 (Liquid)	1	0.0709	0.284	0.382
He (Gas)	2	0.000178	0.00034	0.00057
Fe	26	7.9	11.46	17.38
Pb	82	10.7	12.31	19.26
U	92	19.1	21.01	30.56

bremsstrahlung radiation is proportional to the muon energy, with a higher contribution at higher energies. The bremsstrahlung energy loss can be described by the following formula:

$$-(\frac{d\sigma}{dv})_{br} = \alpha^3(2Z\lambda_e\frac{m_e}{m_\mu})^2\frac{1}{v}(\frac{4}{3}-\frac{4}{3}v+v^2)\Phi(\delta) \tag{2.23}$$

where λ_e represents the electron radiation length and the approximation for $\Phi(\delta)$ can be found in [35].

Electron Pair Production

In direct electron pair production, a muon interacts with the electromagnetic field of a nucleus and generates an electron-positron pair. This process becomes significant at higher energies and can be described by the following formula [36]:

$$(\frac{dP}{dv})_{pair} = C\frac{16}{\pi}Z(Z+\xi)\alpha^2\frac{1}{v}F(E_\mu, v) \tag{2.24}$$

Photonuclear Interactions

Photonuclear interactions occur when a muon emits a virtual photon, which is then absorbed by a nucleus. This process becomes increasingly relevant for muons at higher energies. The contribution of photonuclear interactions is about 1% for the lowest value of the measured fractional loss v and about 5% for the highest v value. The energy loss due to photonuclear interactions is given by [33]:

$$(\frac{dP}{dv})_{photonuclear} = C(\frac{A\sigma_\gamma N(\varepsilon)}{\pi r_e^2})\frac{\alpha}{2}v\Gamma F(E_\mu, v) \tag{2.25}$$

In summary, muon interactions with matter can be understood as a combination of ionization, bremsstrahlung radiation, direct electron pair production, and photonuclear interactions. Among these, ionization dominates at lower energies, while other interactions become significant at higher energies. A comprehensive understanding of these interactions

is essential for the analysis and interpretation of data from muon detection experiments and the further development of muon-based technologies.

2.4 Particle Transport Tools

Codes for the transport are usually based on the Monte Carlo method.Monte Carlo calculations first employed by Buffon in 1777, it was used to calculate the probability of a needle landing on a striped board. Later, Laplace adopted a similar technique to approximate the value of pi. The method's name, inspired by the renowned gambling city in Monaco, underscores its inherent probabilistic essence. The modern application of this technique can be traced back to the Manhattan Project during WWII, where it was crucial in modeling thermonuclear reactions. Notably, Ulam and von Neumann deployed the method for thermonuclear weapon development in 1946 [37]. The Monte Carlo method is distinguished by its approach to developing a statistical model, either replicating a specific problem or creating a model based on distinct rules. The method employs random variables to sample phenomena of interest repeatedly. The resulting data undergoes statistical analysis, turning the simulation into a theoretical experiment. In particle transport simulations, particles are emitted from the source with various spatial energy distributions and different geometries. The subsequent interactions are statistically simulated using applicable probability distributions, with the resulting information collected for further analysis. While the Monte Carlo method's complexity cannot be ignored, its strength lies in its ability to simplify complex problems and implement corrections effortlessly. Particularly in nuclear particle transport, the method can be applied to any geometric shape, regardless of its complexity. Nevertheless, the need for extensive computations often results in long execution times, with substantial improvements in calculation outcomes frequently demanding a considerable increase in computational time.

PHITS

PHITS (Particle and Heavy Ion Transport code System) code, used in the simulations carried out for this project. PHITS is a comprehensive Monte Carlo particle transport simulation code capable of describing the transport of nearly all particles, including muons, across a wide energy range. It has been developed by JAEA, RIST, KEK, and other institutes. PHITS has been used in a variety of research fields including cosmic-ray studies, radiation shielding, and medical physics and accelerator research [38]. PHITS provides a comprehensive simulation of cosmic-ray environments, primarily focusing on galactic cosmic-rays (GCRs) and their interaction with the Earth's atmosphere. It is particularly valuable for researching cosmic-ray muons, a significant component of GCRs. The software incorporates

the PARMA/EXPACS model, which enables a detailed examination of the GCR fluxes in the atmosphere, considering their complex altitude, geographical, and angular dependencies. Also the date for generating the cosmic-ray model can be inputted to the code. This robust method, through the careful handling of simulation parameters, supports accurate analysis of cosmic-ray muons. In PHITS' cosmic-ray source mode allows effective reproduction of cosmic-ray energy and angular distributions in the atmosphere. The absolute values of the tally results are normalized to (/sec) for GCR modes, which aids in calculating direct exposure doses, notably for aircraft crew.

Geant4

Geant4 is an open-source Monte Carlo code that traces its roots back to CERN's detector simulation package. Predominantly used in high-energy particle physics and radiation protection, it can simulate muon interactions within various systems. The project was initiated in 1993 by two independent groups aiming to enhance the Fortran-based Geant3, eventually culminating in the development of an object-oriented technology-based simulation program. Geant4, introduced in December 1998, is built on the C++ programming language, leveraging its advanced software engineering and object-oriented capabilities to construct specific projects. Its object-oriented approach resolves issues of inflexibility and complexity, making it easier to add new physical processes and manage complexity by defining user interfaces in different sections. The core of Geant4 encompasses diverse physical models covering a wide energy range, thereby facilitating control over particle interactions with matter [39, 40].

FLUKA (FLUctuating KAscade)

Fluka is a comprehensive tool for particle transport and interaction calculations, utilized in a diverse range of applications such as accelerator shielding, calorimetry, dosimetry, detector design, and cosmic ray studies, among others. Prioritizing the incorporation and enhancement of modern physical models, Fluka can simulate the interaction and propagation of about 60 different particles, including cosmic-ray muons, photons, electrons, neutrinos, hadrons, antiparticles, and heavy ions across a broad energy range. It is capable of handling complex geometries using an improved version of the Combinatorial Geometry (CG) package and can track charged particles in the presence of magnetic or electric fields. With no requirement for user programming in most applications, Fluka provides a balance between efficiency, accuracy, consistency, and flexibility, while offering unique features such as its ability to

function in both a biased mode and as a fully analogue code, making it a versatile tool for particle physics. [41, 42].

MCNP (Monte Carlo N-Particle)

MCNP is a general-purpose, multi-particle transport code developed by Los Alamos National Laboratory (LANL). It is widely used in nuclear physics, health physics, radiation protection, detector design, and other fields for simulating the interaction of radiation with matter. MCNP can track many particle types over broad energy ranges, including muons. It utilizes a three-dimensional geometry system that allows for complex configurations and offers flexible source and tally options, enabling the simulation of a wide variety of scenarios. While MCNP's primary focus is not cosmic-ray muon simulations, it is capable of simulating these particles, providing a valuable resource for studying their effects and interactions. [43].

Chapter 3

Magnetic field muography detectors

To understand the magnetic properties, two techniques based on muography have been proposed in this chapter. These methods are similar to transmission and scattering muography and can provide us qualitative and quantitative insights of the magnetic field.

3.1 Transmission Method

The first design is based on absorption muography described in Section 1.2.2.

3.1.1 Transmission Muography Detector Design

Normal absorption muography can be used as a tool for magnetic field studies, especially when we are dealing with huge and strong magnetic fields. The setup employed for magnetic field imaging in this method is identical to that of a conventional absorption muography detector as shown in Figure 3.1. The position and direction of the outgoing muons recorded by the detectors located downstream from the volume of interest. A strong magnetic field can be considered as a reflector and return the muons back to the universe. Reflected muons never reach a muon detector located below the magnetic field, similar to absorbed muons that never hit a muography detector placed downstream of the observed object.

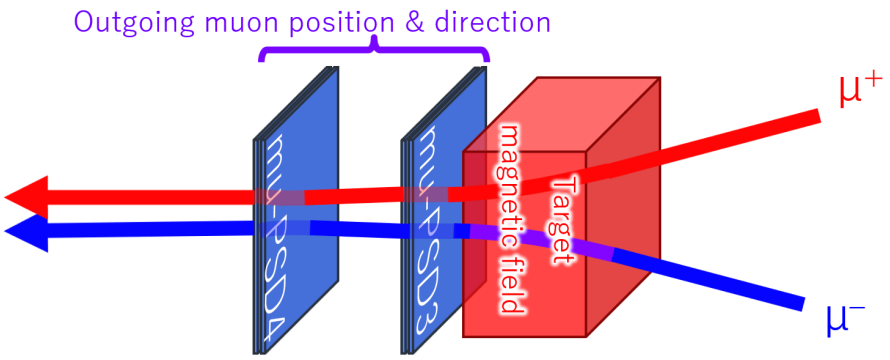

Fig. 3.1: Transmission muography.

This method is suitable for targets that have large-scale magnetic fields. It's applicable when either a background measurement (with the magnetic field OFF) can be done, or a precise simulation can be performed, and when only qualitative measurements are required.

In this context, the term "background" does not refer to open-sky conditions, but instead, it signifies measurements taken when the magnetic field is switched off. This provides a baseline against which the measurements under a magnetic field can be compared.

Given these capabilities, one potential application is in the monitoring of fusion reactors. Fusion reactors are characterized by intense magnetic fields required for plasma confinement, and the method's ability to image such large-scale magnetic fields could potentially be leveraged. However, the sufficiency of this method for fusion reactor monitoring needs further exploration. The efficacy of normal muography in magnetic field imaging for fusion reactors would depend on the reactor's specific requirements, such as the resolution needed, the intensity and variability of the magnetic field, and the conditions under which the imaging needs to occur. This underscores the need for further research and development in this area to fully exploit the potential of muography for magnetic field imaging in demanding industrial applications like fusion reactors.

To have an idea that how muography images might infected by magnetic field, we put a quadrupole magnet in front of 10 iron plates and Figures 3.2 and 3.3 represent the simulation geometry and the muography image of 10 iron plates in normal situation and in the presence of a quadrupole magnetic field.

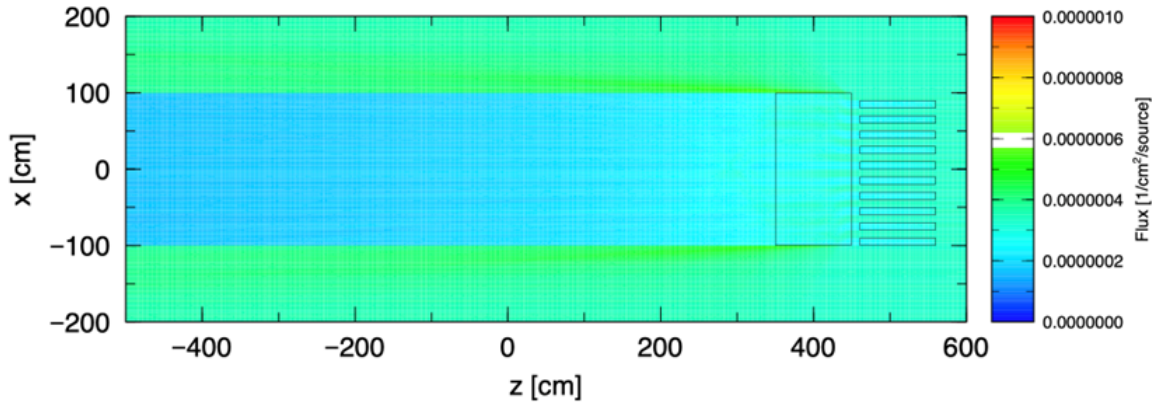

Fig. 3.2: Simulation used for muography image of 10 iron plates.

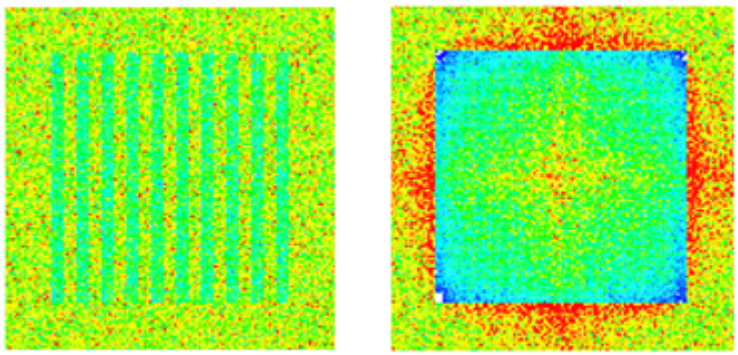

Fig. 3.3: Muography image of 10 iron plates for (a) normal muography and (b) in the presence of a quadrupole magnetic field.

To gain insights into the significance and probability distribution of muons based on their energy, we calculated the Cumulative Distribution Function (CDF) and the Probability Density Function (PDF) of both negative and positive muons at the location of Tokyo using PARMA model. As illustrated in Figure 3.4, lower-energy muons comprise a significant portion of the distribution. Specifically, muons with energy levels of 700 MeV and 500 MeV account for approximately 18% and 12% of the CDF, respectively. Thus, comparing with absorption muography which we use up to 10 % of absorption of muons make sense.

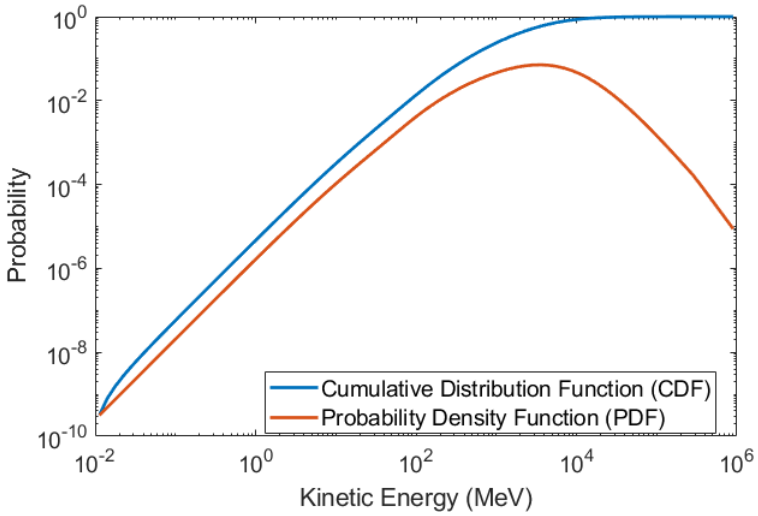

Fig. 3.4: Cumulative Distribution Function (CDF) and Probability Density Function (PDF) of muons calculated by the PARMA model.

The transmission muon method is an absorption-based approach for quantitatively measuring magnetic fields. However, the development of an analysis method to support this approach poses significant challenges due to its strong ill-posed problem nature. The ill-posed nature of the problem indicates that small changes in the input could result in large changes in the output, making it a difficult problem to handle analytically and numerically. To gain more information of the magnetic field, we proposed adding a new equipment to the muon to normal muography setup in order to perform muon charge identification. This part consists of two muon position-sensitive detectors sandwiching a known magnetic field in which positive and negative muons are deflected in opposite directions. Figure 3.5 shows the detection system proposed for this method. In this method, muon energy can be determined using Time-of-Flight (TOF) method or by using a multi-layer detector described in section 3.3.

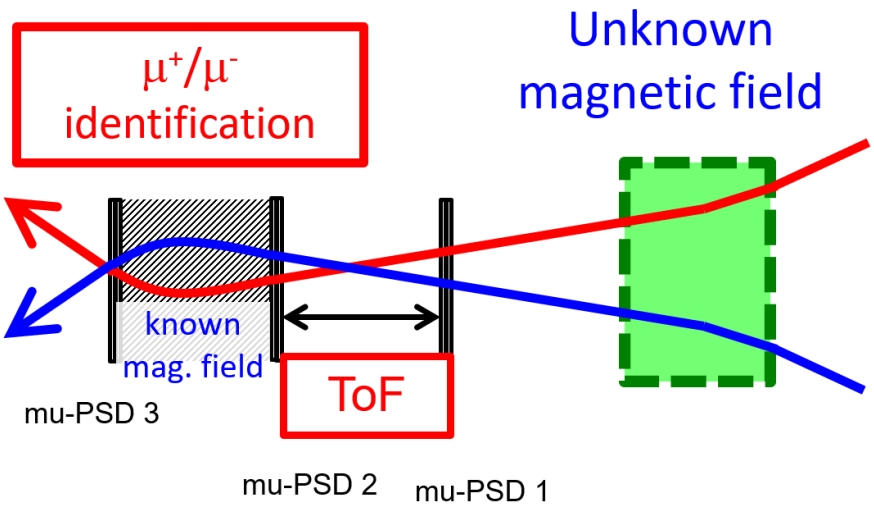

Fig. 3.5: Design of magnetic field measurement based on transmission muography.

While promising, this method demands further research and development to address its analytical challenges and applicability for different magnetic field environments.

3.1.2 Transmission Muography Analysis Method

The Figure of Merit (FOM) analysis is the method proposed for evaluating difference of magnetic field ON (foreground) and OFF (background) states and it allows us to quantify the effect of magnetic field in the muography images.

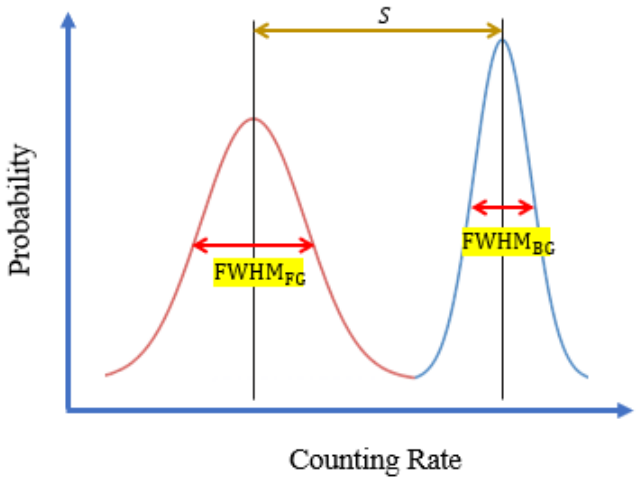

Fig. 3.6: Figure of merit analysis

The statistical significance between background and foreground was analyzed using the figure of merit (FOM) [44] defined as equation 3.1:

$$\mathrm{FOM} = \frac{S}{\mathrm{FWHMFG} + \mathrm{FWHMBG}} \tag{3.1}$$

Where S is defined as the difference between the foreground and background counting rates, and FWHM (the full width at half maximum) can be related to the statistical uncertainty σ using the equation 3.2:

$$\mathrm{FWHM} = 2\sigma\sqrt{2\ln 2} \tag{3.2}$$

In practical terms, a higher FOM would suggest a better differentiate between the two states, signifying a higher reliability of the method for detecting magnetic fields. Conversely, a lower FOM would indicate a lesser capability of the simulation to discriminate between the two conditions, questioning the method's reliability. Moreover, it provides a clear criterion for evaluating the simulation's capability to distinguish between different conditions or states, a crucial factor in the realm of magnetic field detection.

To use the FOM in our simulations, we used vector plots of magnetic field ON and OFF status. Vector plots are generated from the positions of muon hits registered by both detectors. Here, we assume two muon position sensitive detectors a and b, and the detector can measure sixteen discretized hitting position. For a single muon event travers the two detectors, we can obtain the hitting position (x_a, y_a) and (x_b, y_b), respectively by using position IDs from 0 to 15 for the discretized position. For each detected muon event, a vector is generated that points from the hit in the first detector to the corresponding hit in the second detector. This vector is computed by subtracting the coordinates of the hit in the first detector (x_a, y_a) from those in the second detector (x_b, y_b), thus yielding a vector with components $(\Delta x, \Delta y) = (x_b - x_a, y_b - y_a)$.

Plotting Δx against Δy furnishes a distribution that encompasses the vectors. The information held within this plot provides valuable insights about the paths taken by muons as they traverse the detectors. For instance, a vector $(\Delta x, \Delta y) = (0, 0)$ would denote a muon that traversed the detectors without deviating from a straight-line path - a 'vertical' muon, presuming the detectors are horizontally aligned.

The vector distribution can yield rich information depending on the object being probed. A larger spread of vector directions implies that the corresponding region in the object has a higher material density, as it causes more muons to be deflected. Conversely, a narrower spread of vector directions suggests lower density regions, causing fewer muons to deflect.

3.2 Deflection Method

The second design for magnetic field study using cosmic-ray muons is based on the scattering muography described in Section 1.2.2.

3.2.1 Detector Design

In this setup, the magnetic field is 'sandwiched' between two muon detector sets, enabling precise detection of any deflection that muons undergo while traversing the magnetic field. Figure 3.7 shows the proposed system for this technique. The detectable size range of the magnetic fields in this mode is smaller than the previous modes because it is limited by the region between Mu-PSDs and this technique is appropriate for small size magnetic fields. The measurement time in this mode is similar to scattering muography (about 5 to 10 minutes) and much shorter than the other two modes. For qualitative and transmission modes, the time required for the measurement varies depending on the size and magnetic flux density of the target. For example, for targets such as fusion reactors and accelerators, our simulation results have shown that the presence of a magnetic field can be detected in a few hours.

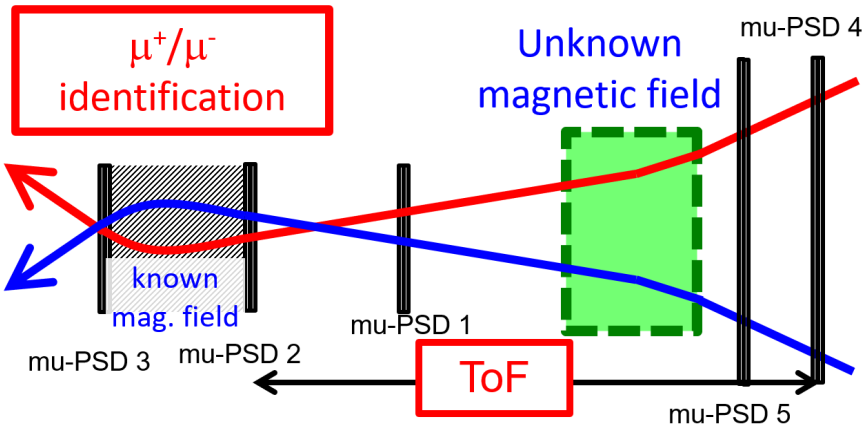

Fig. 3.7: Design of magnetic field measurement system using scattering muography

The primary focus in this approach is the deflection angles of the muons. By tracking the paths of muons entering and exiting the magnetic field, we can derive information about the strength and direction of the magnetic field.

The deflection method allows for the measurement of:

- Incoming position and direction: The exact location and trajectory of a muon as it enters the magnetic field.

- Outgoing position and direction: The location and trajectory of a muon as it emerges from the magnetic field.

The known factors in this method include:

- Double-differential cosmic-ray muons by Particle and Heavy Ion Transport code System (PHITS)-based Analytical Radiation Model in the Atmosphere (PARMA). The cosmic-ray muon flux is crucial for interpreting the measurements accurately.
- The magnetic field region, obtainable through imaging techniques. This provides a spatial context to the measurements, helping to identify any regional variations in the magnetic field.

In this method, two important parameters are Coulomb scattering angle and deflection of muons due to the magnetic field.

3.2.2 Coulomb Scattering Angle

The scattering of cosmic-ray muons is the primary interaction of muons when high-energy muons pass through a medium. This phenomenon is described by the multiple scattering theory (MST) of charged particles, which predicts the scattering angles and lateral displacements experienced by charged particles traversing a medium. Various formulas have been proposed to describe the scattering of cosmic-ray muons, each offering different levels of complexity and accuracy. In these formulas, the radiation length is used as a key parameter and defined as the mean distance a relativistic charged particle travels in an absorbing medium while its energy, due to radiation loss, decreases to 1/e (36.8%) of its initial value [45]. The radiation length is a characteristic length scale that describes the distance over which a charged particle loses a significant fraction of its energy due to interactions with matter. It is an essential quantity in high-energy physics and radiation protection, as it determines the amount of material required to effectively shield against charged particle radiation. The radiation length is defined by Equation 3.3, where A and Z are the atomic weight and atomic number of the material, respectively [46].

$$X_0 = \frac{716.4A}{Z(Z+1)\log(\frac{287}{\sqrt{Z}})} \tag{3.3}$$

The resulting value is given in units of g/cm^2, which can be converted to cm by dividing by the material's density.Table 3.1 shows the radiation length calculated for various materials.

To calculate the radiation length for a compound material, the effective atomic number (Z_{eff}) and effective atomic weight (A_{eff}) of the compound must first be calculated based on

the weight fractions and atomic properties of the constituent elements. The effective atomic number is defined by:

$$Z_{eff} = \frac{\sum_i w_i Z_i^2}{\sum_i w_i Z_i} \tag{3.4}$$

where w_i is the weight fraction of the i-th element in the compound, and Z_i is the atomic number of the i-th element. Similarly, the effective atomic weight is defined by:

$$A_{eff} = \frac{\sum_i w_i A_i}{\sum_i w_i} \tag{3.5}$$

where A_i is the atomic weight of the i-th element. Once Z_{eff} and A_{eff} are known, the same formula for the radiation length can be used with Z_{eff} and A_{eff} in place of Z and A.

Table 3.1: Radiation length calculations for various materials.

Element	**Z**	**A**	**Density (g/cm³)**	X_0 **(g/cm²)**	X_0 **(cm)**
Aluminum	13	26.98	2.7	24.263	8.986
Iron	26	55.85	7.87	14.141	1.797
Lead	82	207.2	11.34	6.311	0.556
Uranium	92	238.03	19.05	5.864	0.308
Water	8	18.015	1	38.801	38.801

The main theory for describing the multiple scattering is Molière theory and the equations to estimate the scattering angle distribution are based on that [47]. A widely used formula for calculating the scattering angle distribution is the Rossi formula [48], which is based on the assumption of small-angle scattering and provides the root-mean-square (RMS) of the scattering angles as:

$$\theta_0 = \frac{15\text{MeV}}{E\beta^2}\frac{x}{X_0} \tag{3.6}$$

Here, θ_0 is the RMS of the angle between the directions projected on a plane of a particle before and after traversing a thickness of x of the absorber, β is the particle's velocity in units of the speed of light (c), X_0 is the radiation length, and E is the energy of the muon. The RMS of scattering angle can be considered in a plane (2D) or in a space (3D). The relation between the RMS plane and RMS space can be described as [40]:

$$\theta_0 = \theta_{plane}^{rms} = \frac{\theta_{space}^{rms}}{\sqrt{2}} \tag{3.7}$$

Highland [49] added a correction term to adjust the formula for experimental purposes, and the formula was recommended by the Particle Data Group (PDG) for estimating multiple scattering [50]. The resulting formula for calculating the RMS of the scattering angle is given as:

$$\theta_0 = \frac{14.1\ \text{MeV}}{E\beta^2}\sqrt{\frac{x}{X_0}}\left(1+0.038\ln\frac{x}{X_0}\right) \tag{3.8}$$

Where the parameters are the same as those in Equation 3.6. This formula provides a better estimation for a wide range of particle energies and material thicknesses. Lynch and Dahl [51] proposed a formula that takes into account the β and incident particle charge (z_{inc}) dependence of the particle. This formula provides a more accurate description of the angular distribution of scattered muons, especially for low-momentum muons. The RMS of the scattering angle is given by Eq. 3.9.

$$\theta_0 = (\frac{13.6\text{MeV}}{E\beta^2})^2\sqrt{\frac{x}{X_0}}(1+0.088\log\frac{xz_{inc}^2}{X_0\beta^2}) \tag{3.9}$$

In this equation, Z_{inc} represents the charge number of the incident particle, which is equal to 1 for muons. The remaining parameters are the same as those in the previous equations.

In practice, these scattering angle formulas are used and implemented in Monte Carlo Simulation codes to estimate the angular distribution of particles after they pass through a medium. By comparing the scattering angles predicted by these formulas with experimental data or simulation results, researchers can evaluate the performance of detection systems and optimize their design to improve the accuracy and efficiency of material identification and characterization.

To use the theoretical formulas provided above, there isn't a strict threshold for the target thickness; however, the formulas are generally more accurate when the target thickness is much smaller than the particle's mean free path. To calculate the mean free path of muons, we need to consider the relevant interaction processes and their cross-sections. For muons traveling through a medium, the main processes to consider are ionization and energy loss, Bremsstrahlung, pair production, and photonuclear interactions. However, the mean free path associated with ionization and energy loss is generally much smaller than the mean free paths associated with the other processes. As a result, the effective mean free path of muons in the material will be determined primarily by ionization and energy loss. For this process, we can use the concept of radiation length, which is a characteristic property of the material and defined in Eq. 3.3.We can approximate the mean free path (λ) of muons in iron using the radiation length (X_0) by the following relation: $\lambda \approx X_0/\ln(2)$ [52]. This approximation comes from the relationship between the mean free path and the distance over

which a particle loses 50% of its energy. By using this approximation, we can determine if the target thickness is much smaller than the particle's mean free path, and consequently, if the scattering formulas are accurate for the specific simulation or experimental conditions.

3.2.3 Magnetic Field Deflection Angle

Muons, like electrons, carry an electric charge, and both positive and negative muons can be found. This characteristic plays a crucial role in their behavior in magnetic fields. Due to their charged nature, muons experience the Lorentz force when moving through a magnetic field, causing their trajectory to be deflected. Notably, this deflection is not a random process, unlike scattering, which is random. Instead, muons follow a helical path governed by the right-hand rule. The degree of deflection depends on several factors, including the muon's velocity, charge, and the strength of the magnetic field [53].

The muon's motion can be described as a combination of a circular trajectory in the plane perpendicular to the magnetic field and a linear motion parallel to the magnetic field. The Larmor radius characterizes the circular component of the trajectory, representing the radius of this circular motion. The deflection angle of muons is defined as the difference between the outgoing and incoming angles, and it can be calculated using Eq. 3.10.

$$\Delta\theta = \frac{qBL}{p_{\perp}}, \tag{3.10}$$

where $\Delta\theta$ is the deflection angle, q is the muon's charge, B is the magnetic field strength, L is the distance over which the magnetic field is applied, and p is the muon's momentum.

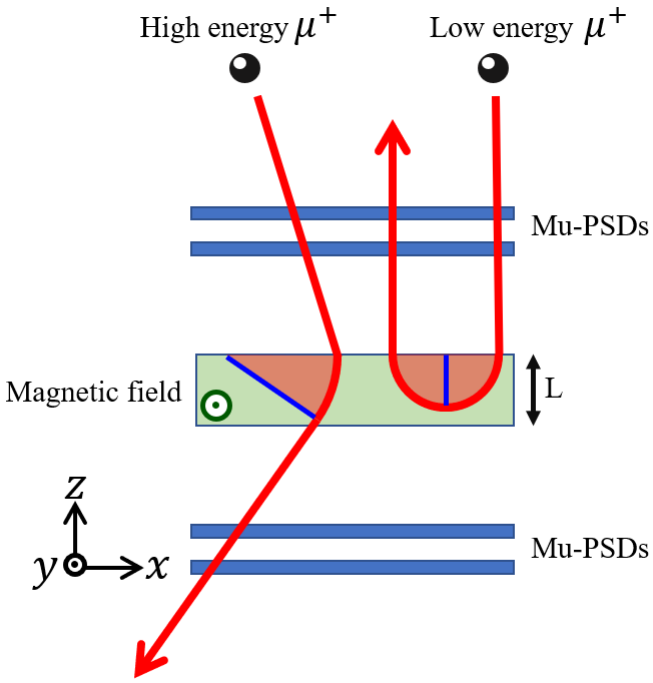

Fig. 3.8: Positive muons in a magnetic field.

Figure 3.8 demonstrates two positive muons crossing a magnetic field. In this example, a low-energy muon is reflected back, while a high-energy muon is deflected. It is important to note that this approach assumes the magnetic field is uniform over the distance L. For non-uniform magnetic fields or more complex geometries, a more detailed calculation or simulation may be necessary.

To compare the formulas about estimating the scatting angle distribution provided above, we calculated the RMS of scattering angle for iron of thickness of 20 cm for incident muons of 700 MeV. The respective RMS values were 13.99, 4.30, and 4.61 degrees for Rossi, Highland, and Lynch-Dahl equations, respectively. To compare this with deflection angle we used simulations in PHITS and changed the iron to magnetized iron of 1 T. The RMS of the scattering angle for iron, magnetized iron, and vacuum magnet were 4.55, 6.14, and 3.97 degrees, respectively.

In order to compute the scattering angle of cosmic-ray muons in a simulation, we can utilize two muon PSD sets (position-sensitive detectors) positioned before and after the region of interest. We can calculate the scattering angle by calculating the angle between the unit direction vectors of the muon paths before and after interacting with the target material as expressed in 3.11. The direction vectors are deduced from the position data recorded by the detectors. The scattering angle is then computed by taking the dot product of these

unit direction vectors, divided by the product of their magnitudes. If $\vec{U}$ and $\vec{V}$ represent the direction of incoming and outgoing muon, then we will have:

$$\theta = \arccos\left(\frac{\vec{U}\cdot\vec{V}}{|\vec{U}|\cdot|\vec{V}|}\right) \tag{3.11}$$

3.2.4 Analysis Method for Deflection Method

In scattering muography, the analysis and characterization of the scattered muons provide insights into the material properties of the object under study. In this method, we propsed using the Point of Closest Approach (PoCA) algorithm [54]. The process to obtain the image of targets has been explained in the following.

The first step of this process involves the reconstruction of the incoming and outgoing muon tracks. This is achieved by using the positional data of the muons hitting the detector, both before and after their interaction with the material under investigation. For each incoming muon, two detectors placed before the target material capture its trajectory. By backtracking the muon's trajectory between these two detectors, we can reconstruct its incoming direction. This method provides us with accurate data regarding the direction from which the muon arrived. Similarly, for each outgoing muon, we employ the same strategy. Following the reconstruction of the muon tracks, the algorithm identifies the Point of Closest Approach (PoCA). In a three-dimensional space, the PoCA is the point which lies closest to both the incoming and outgoing tracks of the muon. The identification of this point is a process of calculating and minimizing the perpendicular distance between the two tracks. Once the PoCA is determined, the algorithm proceeds to calculate the scattering angle, which is the angle between the incoming and outgoing muon paths. This angle serves as a critical parameter, as it reflects the degree of deflection experienced by the muon, and is directly influenced by the nature and density of the traversed material. The final step in the process is a thorough analysis of the distribution of these scattering angles. The pattern of this distribution provides valuable information about the atomic characteristics of the material. Generally, materials with higher atomic numbers or densities cause greater deflections in the muon paths, leading to larger scattering angles. A demonstration of the PoCA algorithm is depicted in Fig. 3.9.

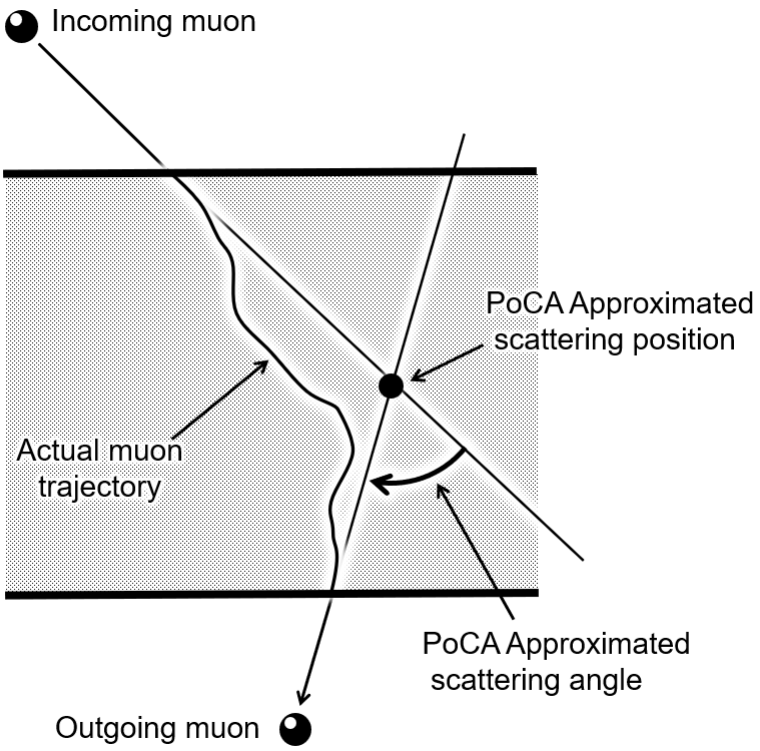

Fig. 3.9: Schematic of the PoCA algorithm.

The deflection experienced by cosmic-ray muons when traversing a magnetic field can serve as a unique methodology for estimating the properties of the magnetic field. In an analogy to scattering angles, which signify the density of a material (where higher-Z material corresponds to larger scattering angles), the deflection angle can give us the details about the magnetic field.

One of the main challenges with this approach is differentiating the magnetic field's influence from other potential sources of muon deflection, such as scattering within the medium. To address this, we can conduct simulations assuming that the magnet target is not magnetized, which would enable us to ascertain the scattering angle distribution in the absence of a magnetic field. Furthermore, we can utilize a target where the magnetic field can be toggled OFF. Comparing the deflection angles when the magnetic field is ON versus OFF can reveal the impact of the magnetic field.

3.2.5 Magnetic Flux Density Estimation Through Shift in PoCA Points

In the presence of magnetic field, PoCA points positions are determined by scattering and deflection. In this section, we endeavor to study this shift in PoCA points as a potentially reliable marker for estimating the magnetic flux density.

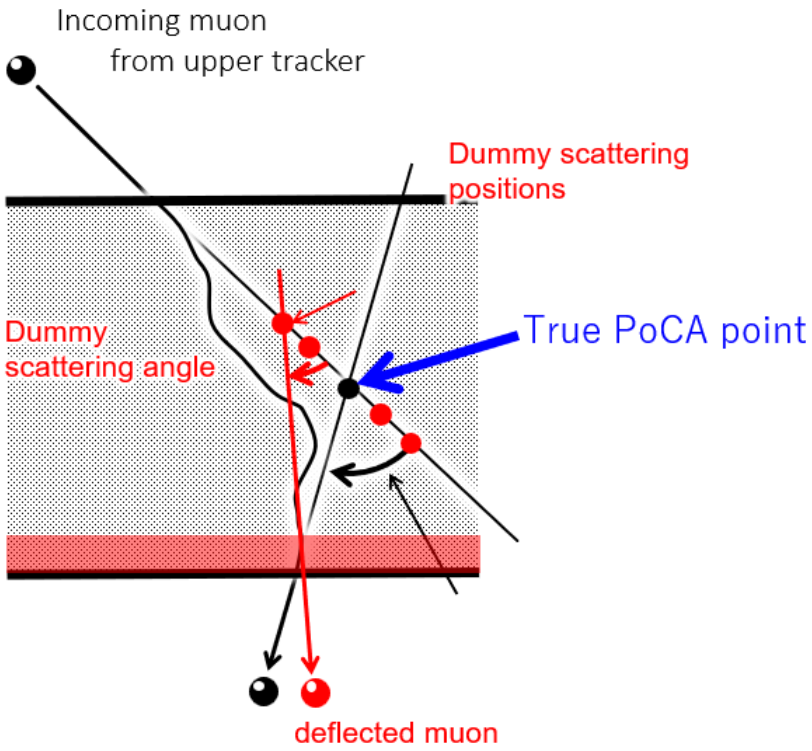

Fig. 3.10: Illustration of the magnetic field's influence on PoCA points.

To explore the magnetic field's impact on the PoCA points, we deployed a parallel beam of positive and negative muons. These muons had an energy distribution predicated on the PARMA model and were projected onto a uranium target with dimensions of 40 $cm \times$ 40 $cm \times 10$ cm. Our detectors, crafted from plastic scintillators, possessed dimensions of 2 $m \times 2$ $m \times 2$ mm, while the region exposed to the magnetic field spanned 50 $cm \times 50$ $cm \times$ 10 cm shown in Figure 3.11.

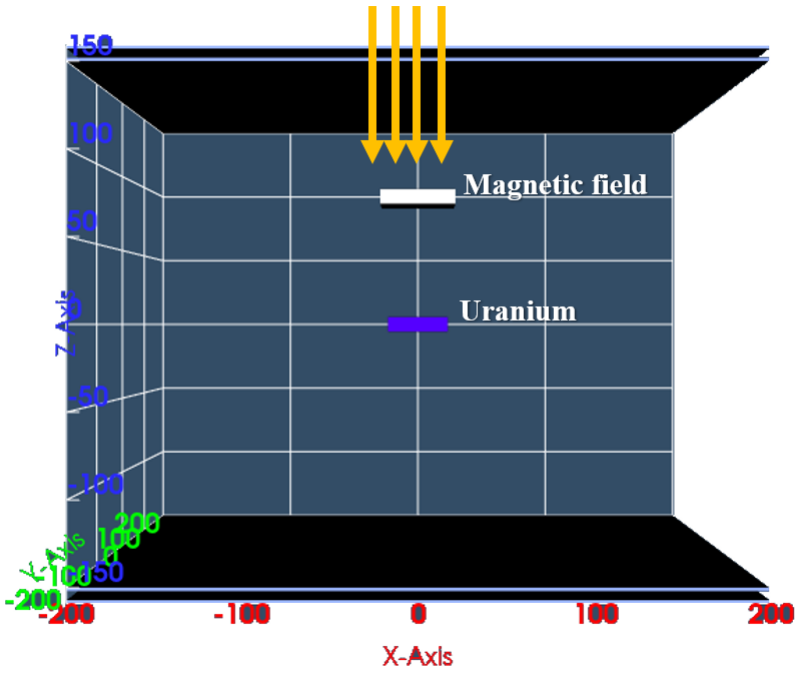

Fig. 3.11: Magnetic field region and uranium target simulation geometry.

The subsequent figures illustrate the distribution of PoCA points under various circumstances, which include the absence of a magnetic field and the presence of magnetic fields of different intensities, specifically 100 mT, 200 mT, 500 mT, 1T, and 5T. As evident from the figures, the PoCA points undergo distinct shifts and transformations under each condition, suggesting a potential correlation between these shifts and the magnetic field strength.

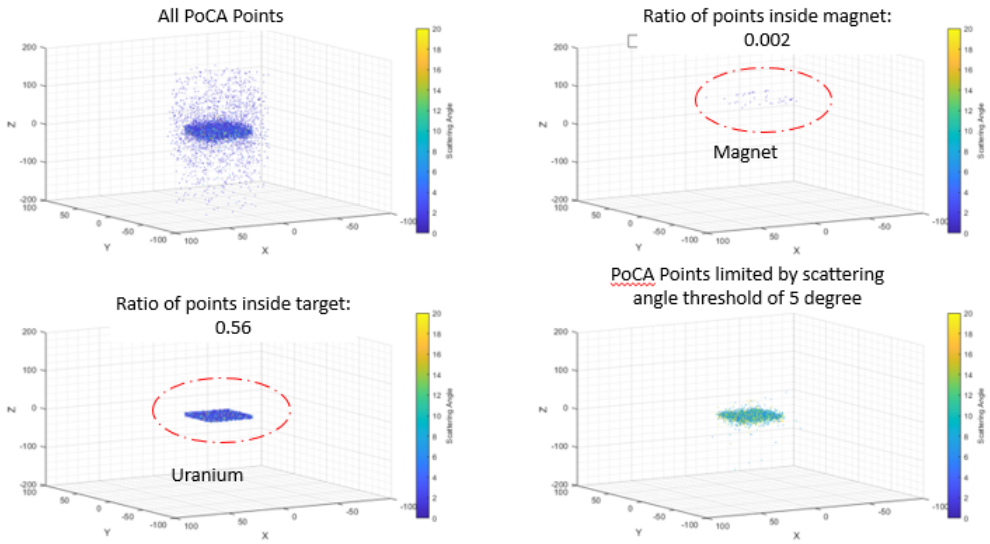

Fig. 3.12: Uranium target with no magnetic field.

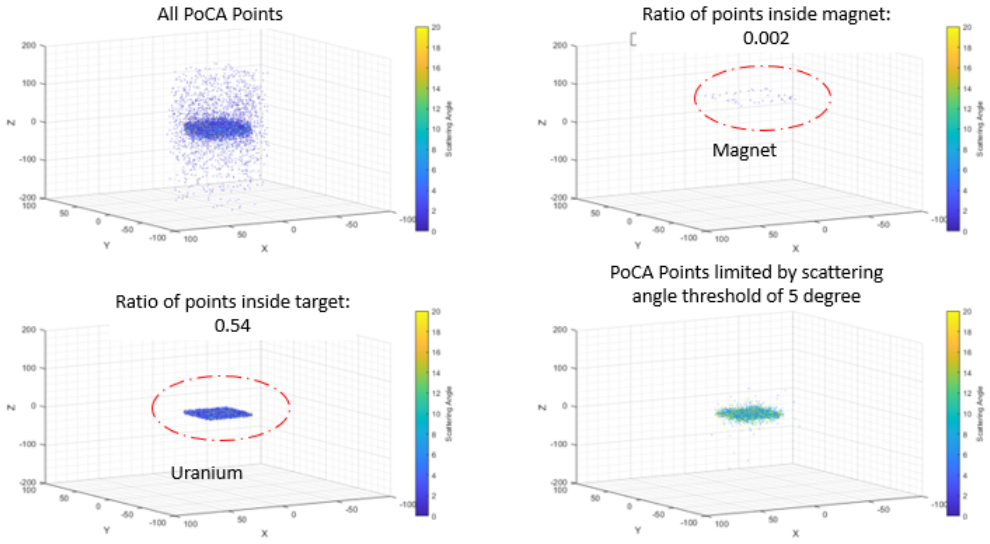

Fig. 3.13: Magnetic field of 100 mT and uranium target.

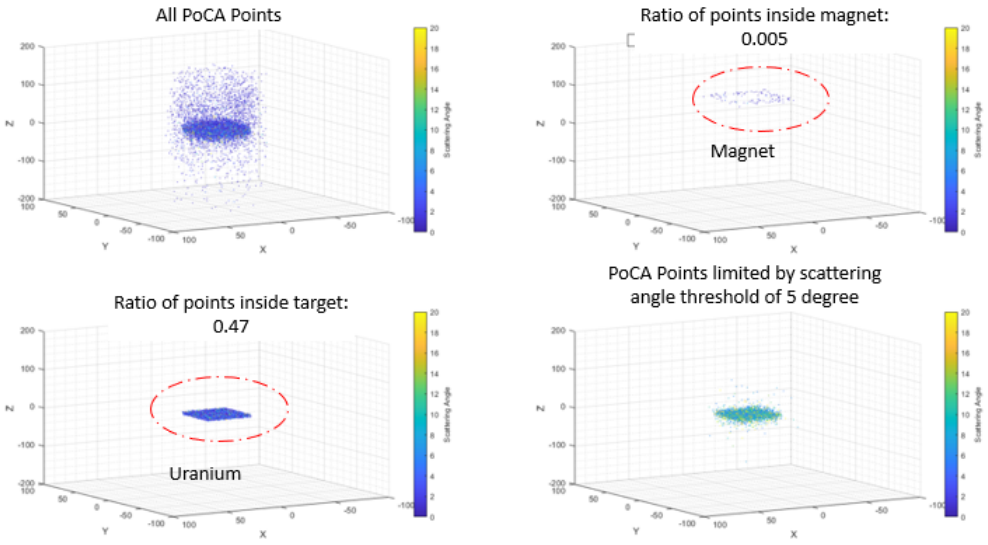

Fig. 3.14: Magnetic field of 200 mT and uranium target.

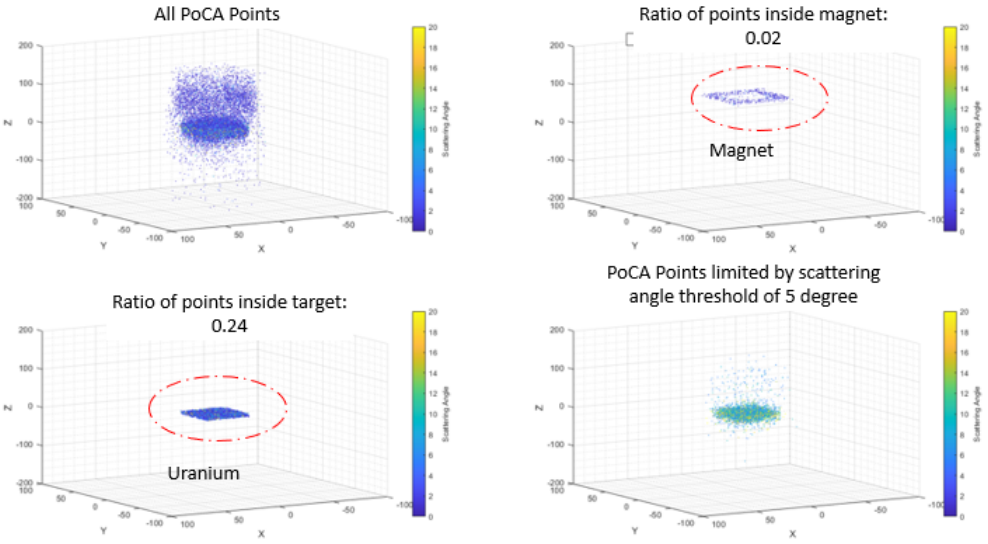

Fig. 3.15: Magnetic field of 500 mT and uranium target.

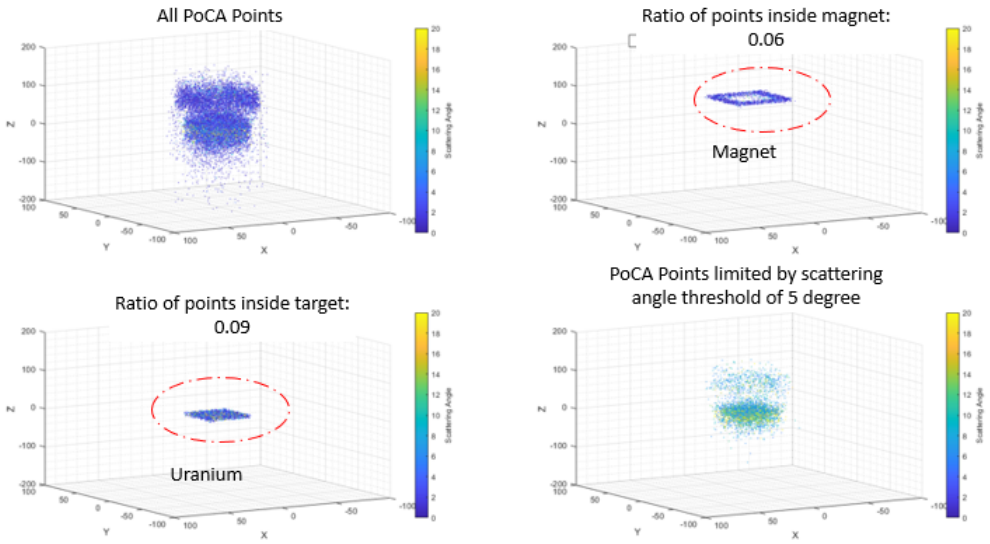

Fig. 3.16: Magnetic field of 1 T and uranium target.

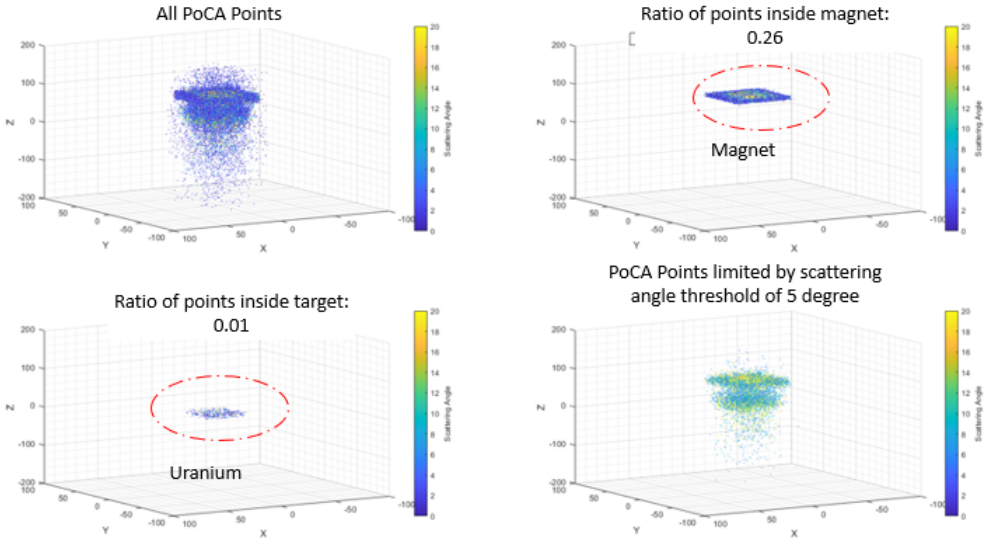

Fig. 3.17: Magnetic field of 5 T and uranium target.

In order to draw comparative insights on the magnet's impact on various materials, we performed simulations using four targets, comprised of uranium, lead, aluminium, and iron. We captured images in the absence of a magnetic field and with a 500 mT magnetic field positioned behind the targets.The results displayed in Figures 3.19 and 3.20 reveal that low-Z materials experience more pronounced image distortions compared to high-Z materials when exposed to the magnetic field.

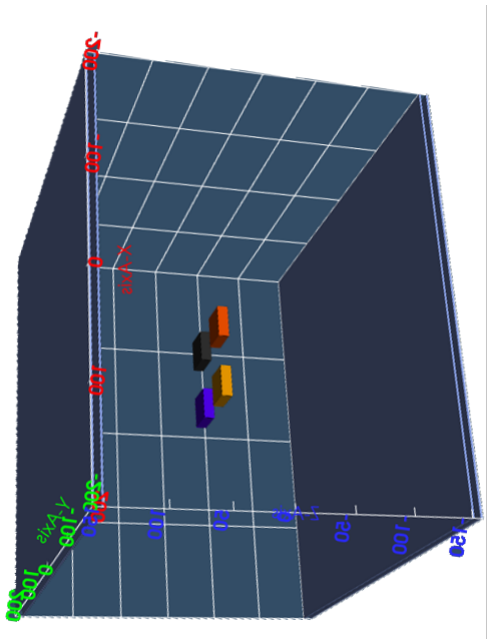

Fig. 3.18: Geometry of simulation using 4 targets.

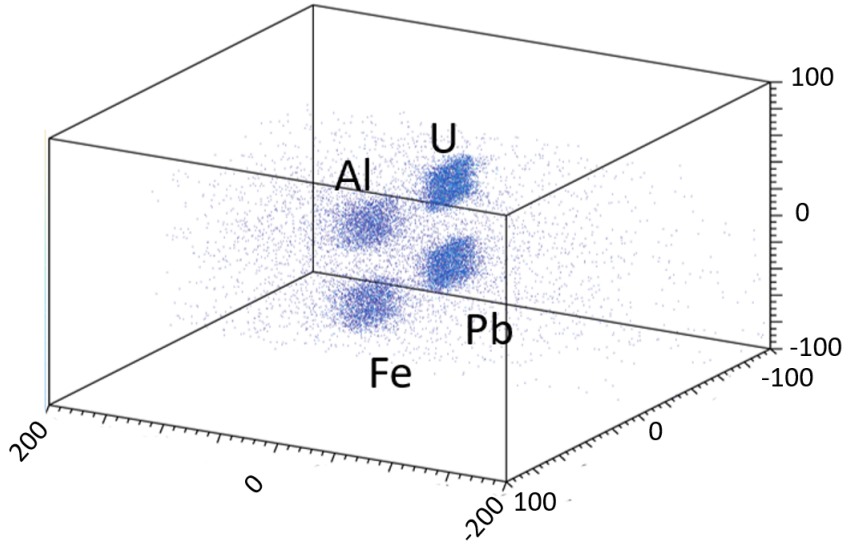

Fig. 3.19: Muography image of 4 targets using PoCA algorithm.

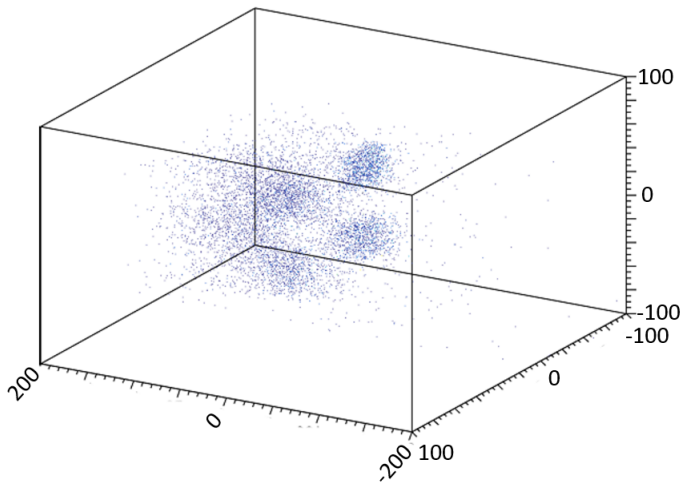

Fig. 3.20: Influence of magnetic field on the image of 4 targets.

Taken together, our simulation results indicate that the displacement of PoCA points is influenced by the magnetic field flux density. This observed correlation suggests the potential of utilizing PoCA point shifts as an indicator to estimate the magnetic field flux density effectively. However, the PoCA shift analysis is sensitive to the accuracy of the muon trajectory estimation. Errors in the trajectory estimation can lead to errors in the PoCA, which can in turn affect the magnetic field estimation. It also requires a sufficient number of muons passing close to each voxel to provide reliable statistics, which may not be achievable in all experimental setups.

3.3 Muon Energy Spectrometer

Our preceding discussions and analytical equations indicate that the kinetic energy of the incoming muon, the muon's displacement in the magnetic field, and the magnetic flux density are three critical parameters in this analysis. Determining any two of these parameters allows us to calculate the third. In this section we will propose some methods to determine muon energy to be used with the displacement information of muons to estimate the magnetic flux density.

The muon's displacement due to the magnetic field, denoted as (Δ) in Figure 3.21, is computed by measuring the positions of the incoming and outgoing muons.

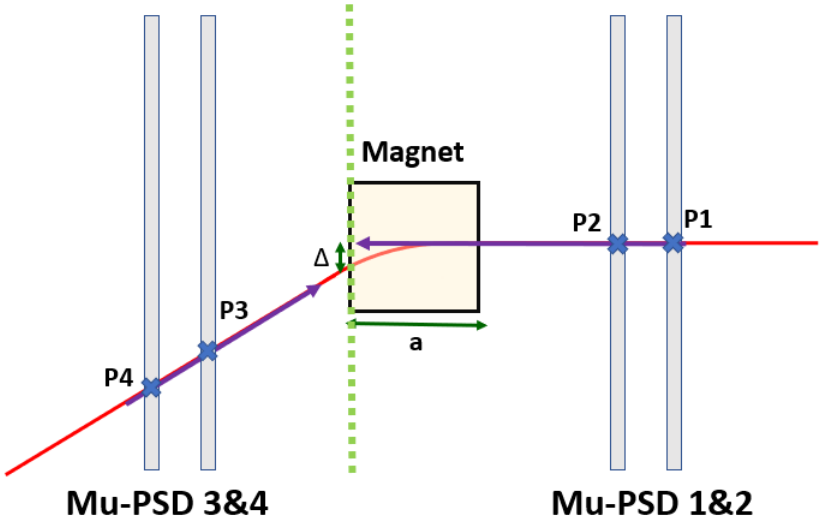

Fig. 3.21: Displacement of muons due to magnetic field.

The displacement measurement utilizes the information on the magnet's position and the direction in which muons hit the detector. Specifically, the muon direction is calculated from the first and second muon position-sensitive detector (mu-PSD) hit positions (denoted P1 and P2 in Figure 3.21) using the following equation:

$$U = \frac{P2 - P1}{\sqrt{(P1_x - P2_x)^2 + (P1_y - P2_y)^2 + (P1_z - P2_z)^2}} \tag{3.12}$$

With this directional information and the known positions, we can predict the muon's location at the last plane of the magnetic field region, in a scenario where the magnet is absent, using data from mu-PSD 1 and 2. The actual muon position exiting the magnetic field can then be found using data from mu-PSD 3 and 4. The displacement of the muon due to the magnetic field is estimated by subtracting the predicted position (assuming no magnet) from the actual position.

3.3.1 Magnetic spectrometer

This method involves using a known magnetic field as a reference to identify the charge of muons and determine their energy. The behavior of muons in this known magnetic field can be carefully studied, allowing for the development of a model that links muon charge and energy to their deflection pattern. This model can then be applied to unknown magnetic

fields to estimate their properties and also for designing the detector features. To estimate the magnetic flux density using cosmic-ray muons, a setup of 6 muon position-sensitive detectors (Mu-PSD) and one known and one unknown magnetic field was designed as shown in Figure 3.22.

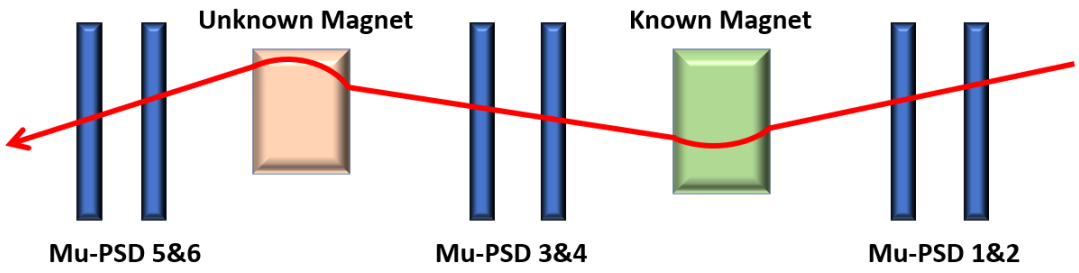

Fig. 3.22: Setup of detectors and magnetic fields.

By finding the displacement using the equations provided above, we can calculate the energy of incoming muons for a known magnetic field. Here the known parameters are:
a = thickness of magnetic field
Δ = displacement of muon in the magnetic field region

In the following calculations, we used the constant parameters listed in Table 3.2:

Table 3.2: Constant parameters.

Parameter	Value
m_μ (muon's mass)	$1.883531627 \times 10^{-28}$ kg
c (speed of light)	299792458 m/s
q (elementary charge)	$1.602176634 \times 10^{-19}$ C
$E_0\mu$ (muon's rest energy in joules)	1.69×10^{-11} J
$E_0\mu$ (muon's rest energy in MeV)	105.6700 MeV

In order to calculate the kinetic energy of incoming muons by using a known magnetic field, the following steps are required:

1. Calculate the Larmor radius using the geometrical relations:

$$r = (a^2 + \Delta^2)/(2\Delta) \tag{3.13}$$

2. Velocity of muons can be calculated using:

$$v = \sqrt{B^2 r^2 q^2 c^2/(B^2 r^2 q^2 + m_\mu^2 c^2)} \tag{3.14}$$

3. To calculate Lorentz factor(γ):

$$\gamma = 1/\sqrt{1 - v^2/c^2} \tag{3.15}$$

4. The total energy of muon can be obtained by using:

$$E = \gamma E_0 \tag{3.16}$$

5. Finally, the kinetic energy T can be calculated by subtracting E_0 from total energy:

$$T = E - E_0 \tag{3.17}$$

Now the energy of each incoming muon is determined and we can use that together with the displacement parameter that we already calculated, to estimate the magnetic field flux density of an unknown magnetic field by the following steps:

1. The total energy of muon can be obtained by using:

$$E = E_0 + T \tag{3.18}$$

2. Lorentz factor(γ) will be:

$$\gamma = 1 + (T/E_0\mu) \tag{3.19}$$

3. We can obtain the velocity using:

$$v = c\sqrt{(1 - (1./\gamma^2))} \tag{3.20}$$

4. The ratio of the muon's speed to the speed of light defined as β as:

$$\beta = \sqrt{(1 - v^2/c^2)} \tag{3.21}$$

5. By using the geometry information the Lamor radius can be approximated using:

$$r = (a^2 + \Delta^2)/(2\Delta) \tag{3.22}$$

6. Angular speed ω will be defined as:

$$\omega = v/r \tag{3.23}$$

7. Finally, magnetic flux density B can be calculated using the following equation:

$$B = \frac{\omega m_\mu}{q\beta} \tag{3.24}$$

3.3.2 Time-of-Flight (ToF)

Time-of-Flight (ToF) techniques constitute an essential tool for estimating the energy of muons, primarily relying on the measurement of the time a muon takes to travel a predetermined distance. The central idea is straightforward: if we know the distance a muon has traveled and the time it took to traverse that distance, we can calculate its speed.

Energy resolution of ToF method is dominantly determined by flight-path length and time resolution of the DAQ system. Some of the latest technologies achieved 50 ps of time resolution which corresponding to a few tens of MeV energy resolution around a few hundreds of MeV muons. It limits the measurable dynamic range up to around 500 MeV for the proposed detection conditions.

The precision and accuracy of this method can vary depending on the specifics of the experimental setup. For instance, the energy resolution depends on the distance between detectors: a larger distance can enhance the resolution but may also this may cause a lower muon detection rate as they probability of being absorbed or deflected in the larger distance will be more. In the case of measuring muons with energies around 500 MeV, an appropriate detector distance must be set to achieve the optimal balance between detection rate and resolution.

While ToF techniques offer a straightforward and relatively precise method for estimating muon energy, it is important to note the dependence on the timing resolution and detector setup. Therefore, careful calibration and design of the experiment are necessary to mitigate systematic uncertainties and optimize the measurements.

3.3.3 Multi-layer Muon Energy Spectrometer

Multilayer detectors are intricate systems designed to offer detailed measurements of muon trajectories and energies. They typically consist of alternating layers of iron plates and plastic scintillators, carefully designed to interact with muons at different energy levels. Figure 3.23 shows a design proposed by our group for multi-layer detector [55].

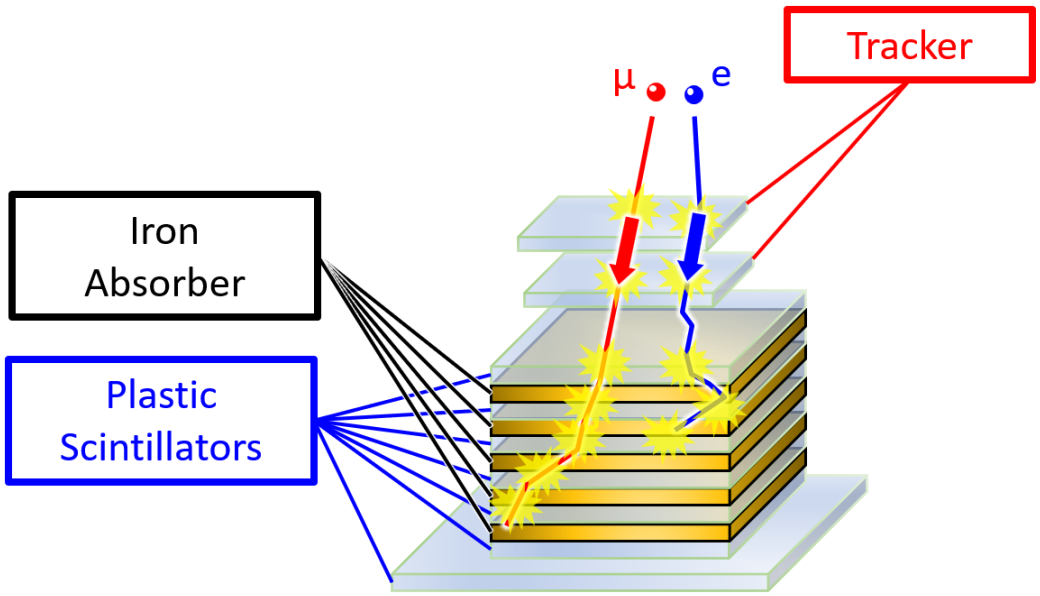

Fig. 3.23: Multi-layer muon energy spectrometer.

These layers work together to form a multilayer spectrometer capable of measuring muons across a wide range of energies simultaneously. The iron plates serve as absorbers that interact with the muons, causing them to lose energy and emit detectable particles. The plastic scintillators are used to detect these particles, and the energy of the muons can be inferred from the intensity and pattern of the detected signals.

In addition to energy measurements, these detectors can provide angular differential information through a muon tracker. This muon tracker can record the deflection of muons as they traverse the detector, providing additional insights into the magnetic field's strength and direction.

Furthermore, the energy deposition pattern within the detector layers can be used for particle identification (e.g., distinguishing between electrons and muons) and kinetic energy prediction. These capabilities make multi-layer detectors a powerful tool for magnetic field measurement using cosmic-ray muons, offering a high degree of precision and versatility.

Chapter 4

Feasibility Simulations

This chapter provides the details regarding the designs and geometries of various simulation scenarios and the results obtained for each simulaiton. Initially, we delve into the simulations implemented for strong and weak magnetic fields. Following this, we explore the simulations focused on assessing the impact of magnetic fields in the material detection and inspection systems. Finally, we conclude the chapter by outlining the simulations developed for two practical approaches.

4.1 Transmission method

4.1.1 Strong Magnetic Fields

To investigate the feasibility study of using cosmic-ray muons for magnetic field imaging in strong magnetic fields (more than 500 mT) a simulation setup shown in Figure 4.1 has been performed. We used PHITS and the cosmic-ray muons were generated with a realistic double differential flux, using the PARMA model. Since the difference between the foreground (with magnetic field) and background (without magnetic field) muography images are important, we performed the simulation in two steps. First, the muography image of nine lead blocks with a height of 30 cm was obtained using absorption muography. Then, a magnetic field with 4 different magnetic field flux densities was placed 1 meter above the detector to demonstrate the effect of the magnetic field on the muography images of the lead blocks. We assume 152 hours of measurements for each condition.

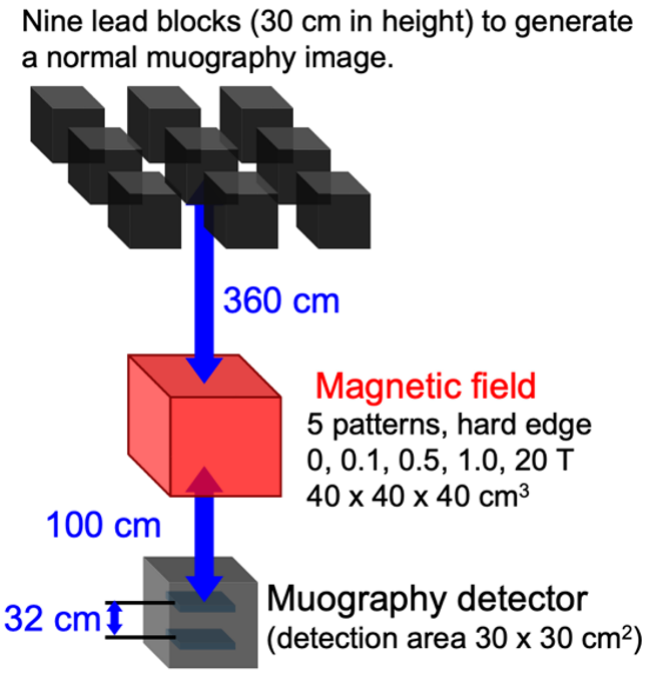

Fig. 4.1: Simulation setup and conditions for magnetic field imaging.

To analyze the simulations we used an assumption that cosmic-ray muography image is affected only by the magnetic field. In other words, the assumption states that the muography images are affected only by the absorption of objects and the deflection of muons by a magnetic field. Thus, magnetic field imaging can be found as the significance of a foreground muography image with respect to its background image. Note that unlike normal muography, the background is not an open-sky measurement but a measurement of known objects without a magnetic field. For a weak magnetic field, the effect can be observed as a distortion of the image.

In the case of a strong magnetic field, since a considerable number of muons with lower energies are deflected in a direction outside the detection range. Thus, the magnetic field acts as a momentum filter for the muons. In summary, we can straightforwardly determine the presence of a magnetic field by significance analysis of the magnetic field applied image from the background image. We used FOM method to detect the magnetic field region. As the FOM solely indicates the level of peak separation, it is necessary to establish a threshold value for magnetic field imaging. For the time being, we can consider utilizing a threshold value of 2.

The background image (muography image without a magnetic field) has clear nine lead blocks shown as “BG” in Fig.4.2 (a). First, we obtain a distorted image at 100 mT. Such a

weak magnetic field leads to a slightly distorted image, but at stronger magnetic fields, the magnetic field acts as an energy filter for muons. Next, all muography images affected by the magnetic field were analyzed using the FOM method. When the presence of a magnetic field is detected, the pixel is colored red to create Fig.4.2 (b). According to the results, the regions with magnetic flux densities of 1 T or stronger magnetic fields can be detected using a threshold value of 2 for FOM. Some incorrectly detected regions were observed around the edge of the magnetic field, but this is due to the geometric conditions of the magnet. Since the magnet has hard edges, muons passing near the edges of the magnetic field escape the magnetic field, resulting in very little deflection.

Moreover, the FOM values obviously increase when the magnetic field increases. Thus, we can estimate the absolute value of the magnetic flux density (the flux direction is never determined by the magnetic field imaging mode).

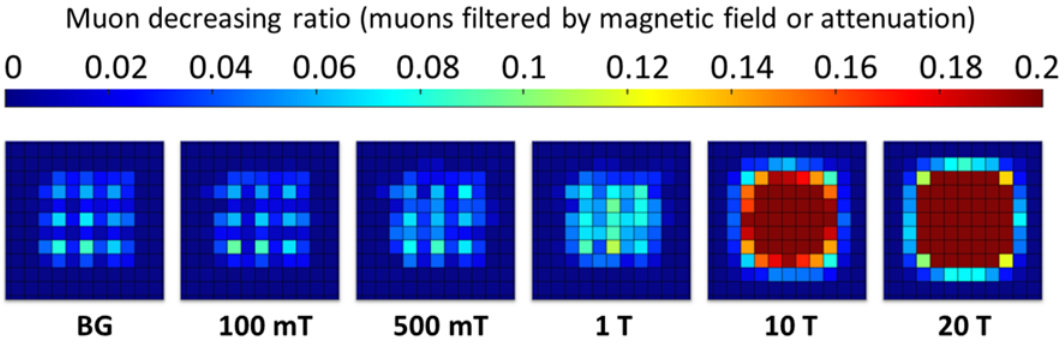

(a) Muography images of lead blocks

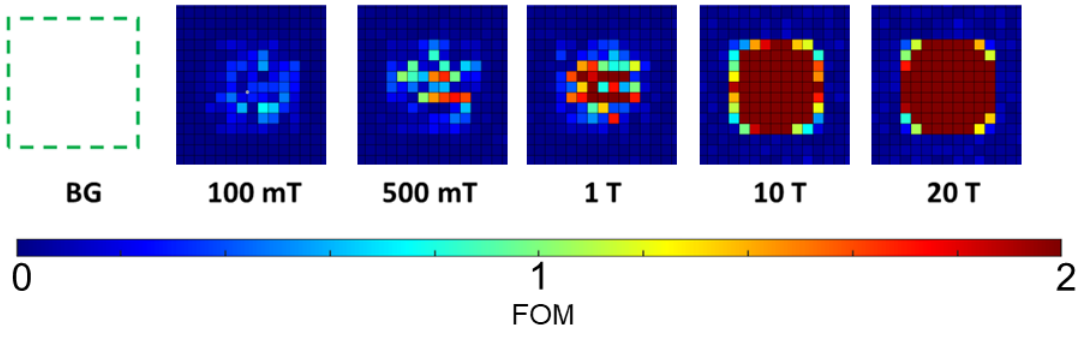

(b) Magnetic field region detected by Figure of Merit (FOM)

Fig. 4.2: (a) Muography images (attenuation ratio maps) of nine blocks with magnetic field flux densities of different magnitudes. (b) Magnetic field regions determined by the FOM methods are colored red, and the actual magnetic regions are indicated by dashed lines.

To determine the measurement time, we must consider the two parameters of dimension and magnetic flux density of the target. Measurement time is defined as the time we need to find a difference between the muography image when the magnetic field is off (background image) and when the magnetic field is present. For targets similar to fusion reactors and accelerators, preliminary simulations have shown that even after a few hours of measurement for the background and foreground, the effects of the magnetic field can be seen in the muography images. In both accelerators and fusion reactors, operations are stopped for inspection at regular intervals. Therefore, it is possible to monitor the background and foreground and obtain the muography images while the magnetic field is OFF and ON.

In summary, according to the simulation results, the magnetic field imaging for nuclear fusion reactors and accelerators is promising in the range of magnetic flux density from a few to 10 T, considering their enormous size and strong magnetic field.

In conclusion, the results demonstrate that magnetic field imaging or monitoring of variations in strong magnetic fields using cosmic-ray muons is applicable for targets of large size and strong magnetic fields, such as fusion reactors and accelerators with magnetic flux densities of a few tesla.

4.1.2 A Dipole Magnet with a Magnetic Field of 200 mT

In this section we present a feasibility study of by simulating a simple dipole magnet using the three-dimensional finite element solution package AMaze, together with the PHITS.

In the first step, the magnetic flux density of a simple dipole magnet was simulated in the AMaze software. The dimension of each magnet plate was considered to be 20 cm $\times$ 20 cm $\times$ 1.1 cm and the gap between two magnet plates was 9 cm. The plates were surrounded by a yoke of a thickness of 1 cm. A quite uniform magnetic flux density of 0.2 T was created in the gap region and the 3D distribution of magnetic flux densities was calculated in a 40 cm $\times$ 40 cm $\times$ 40 cm voxelized region around the magnet.

The next step was to convert the calculated distribution of magnetic flux densities into a format readable by PHITS. Then, the geometry of the magnet was defined in PHITS and the cosmic-ray muons were generated as originating from a hemisphere with a radius of 560 cm, assuming the local geomagnetic cut-off corresponding to the location of the Chikushi campus of Kyushu University ($33°31'N$, $13°28'E$, 35 m above sea level) using the model PHITS-based analytical radiation model (PARMA) implemented in the PHITS code [26]. The number of events corresponds to 152 hours of data collection and is large enough to achieve a statistical uncertainty of 1% in the region of interest.

To observe the influence of the magnet on traditional muography imaging, we placed a lead block with the height of 30 cm, 5 meters above the first mu-PSD. The position of the

lead block was determined in a way that it represented a single pixel in the center of the count rate map considering the detector resolution. The lead block is composed of smaller lead blocks of the dimension of 20 cm $\times$ 10 cm $\times$ 5 cm, disposed in such a way that we maximize the absorption of muons by lead while not exceeding the maximum load limit of the roof of the building, which is 300 kg per square meter. The distance between the two mu-PSDs is 31.9 cm and each mu-PSD has a size of 29.6 cm $\times$ 29.6 cm $\times$ 0.4 cm with 16 channels for each x and y direction, leading to a pixel area of 3.4 cm^2. The geometry and dimensions used in this simulation can be found in Figure 4.3.

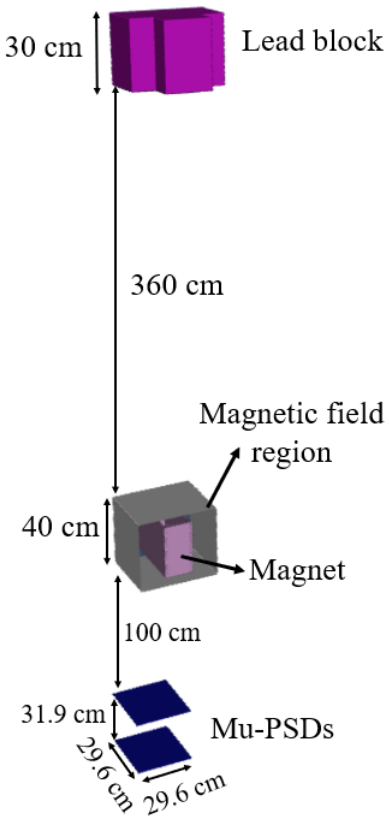

Fig. 4.3: Geometry of simulation in PHITS.

To illustrate the defined magnetic field region and verify the conversion of AMaze to PHITS, we used a surface source with 100 MeV muons. As shown in Figures 4.4a and 4.4b , the deflection of the muons is proportional to the magnitude of the magnetic field flux density in the defined meshes. The deflection is almost zero at the entrance of the magnetic field region and maximum in the middle where magnetic field is maximum. Moreover, positive and negative muons are deflected in opposite directions as expected. Due to the complexity of the magnetic field near the edge of the magnet, some muons are deflected in the opposite

direction. The empty area in the magnetic field region corresponds to the magnet plates where these 100 MeV muons were absorbed.

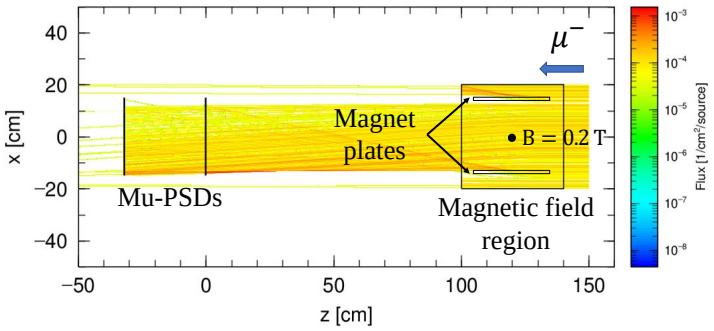

(a) Negative muons deflection due to magnet.

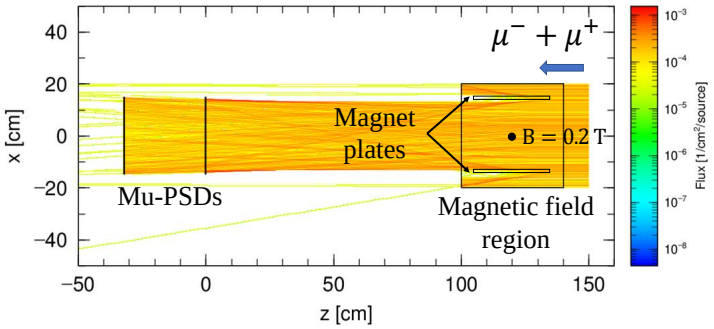

(b) Positive and negative muons deflection due to magnet.

Fig. 4.4: Simulation of the set-up for this feasibility study (a), and effect of the magnetic field on the muon trajectories (b,c) illustrated for the case of 100 MeV energy.

The information about the position, direction and energy of the muons hitting the first mu-PSD was analyzed using the ROOT framework [56]. We simulated three different conditions:

(a) Open sky: only the mu-PSDs in the PARMA source.

(b) Background: lead block and magnet while the magnetic field region was turned OFF.

(c) Foreground: lead block and magnetic field ON.

To study the effect of the magnet, the contrast of the count rate maps for the background and foreground measurements is important, therefore the counting rate maps (muography images of the lead block) for all three conditions were plotted. Figure 4.5 shows the vector plots corresponding to the displacement of muons between the upper and lower mu-PSDs for the three stages of this study. As we expected based on the theory and the known distribution

of cosmic muons (that approximately follows a $cos^2\theta$ 2.2 dependence on the zenith angle), in the open sky measurement we see the maximum flux in the center due to vertical events, while in the background the effect of absorption of muons in the lead block has a large impact on the flux in the center of the plot. In the foreground simulation, the distribution of counts has changed due to the effect of the magnetic field, and the central pixel corresponding to the image of the lead block is blurred. The increase in the pixels around $\Delta x, \Delta y = (0,0)$ is due to the deflection of the vertical events. In addition, some muons that could not reach the detector during the background measurement hit the detector after crossing the magnetic field region.

To detect the magnetic field region we used FOM analysis 3.1.2 and we applied a threshold of $FOM > 2$ which is a commenly used value in various applications. Each bin in the counting rate map of the background measurement was compared with the same bin in the foreground measurement and if the calculated FOM value was greater than 2 we considered that bin as magnetic field region. As the result of this analysis a square area in the center of the counting rate map was estimated as a possible magnetic field area. The magnet itself has a rectangular shape, but the magnetic field was present in a cubic volume around the magnet, so the detected region has a square shape.

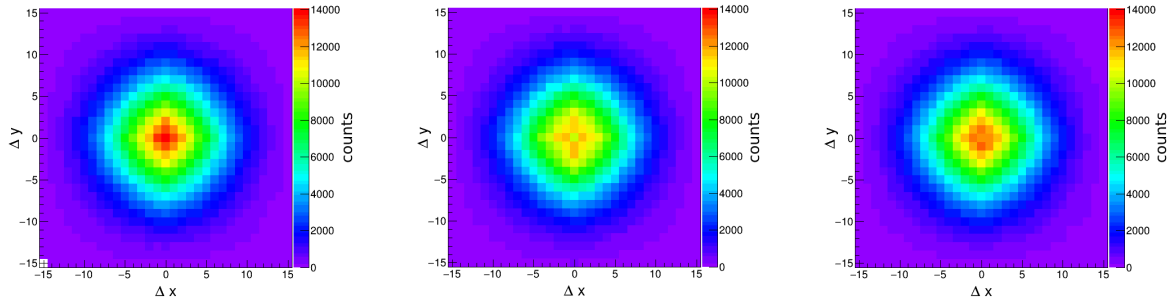

(a) Open sky (b) Background (c) Foreground

Fig. 4.5: Muon counting rate maps for a realistic simulation of the muon flux.

In conclusion, for a feasibility study of the proposed magnetic field muography technique, a simulation study was carried out in this section. First, the magnetic field flux density distribution around a simple dipole magnet (which had a maximum value of 0.2 T) was calculated using the AMaze software. Then, the magnet and magnetic field region were implemented in PHITS and the effect of this magnet on the count rate maps (muography image of a lead block) for the magnetic field ON and OFF status were studied. The results showed that this magnet has a significant impact on the count rate maps and can blur the lead block muography image. This effect can be used for magnetic field analysis. The simulation

results are promising for the newly proposed application of cosmic muons, the imaging of the magnetic field.

4.2 Deflection Method

4.2.1 Magnetic Field Effect in Material Detection

Additionally, magnetic fields can lead to inaccuracies in the Point of Closest Approach (PoCA) analysis, a common technique used in muography to determine the path of muons through a target. Due to the deflection caused by magnetic fields, the true PoCA point positions are often not obtained accurately. As shown in Figure 3.10, many reconstructed events that are interpreted as passing through a uranium block may actually be deflected trajectories due to the magnetic field, leading to misinterpretation of the detected material.

These factors underline the importance of detecting and characterizing magnetic fields in muography-based inspection systems. In the simplest scenario, the system can be updated to have the ability to detect magnetic fields and if any magnetic field is detected, further inspections are required. To investigate this idea, a simulation has been performed using the geometry shown in Figure 3.18. In this simulations, cosmic-ray muon source based on PARMA has been generated and the number of muons generated is equal to one hour measurement in the real-time. The simulation has been conducted in two steps. First the muography image of a target of 20 cm × 20 cm × 20 cm uranium and the distribution of PoCA points and also the scattering angle in a voxelized region of interest has been obtained. In this simulations we divided the region of interest into voxels of a dimension of 10 cm × 10 cm × 10 cm. Then, a dipole magnet of 250 mT has been placed below the target.

The image of uranium target has been obtained using PoCA algorithm shown in Figures 4.7 and 4.8. The later figure has a threshold of 5 degree on the scattering angle of muons. As depicted in the figures the uranium target can be seen clearly. Next the image of voxelized region of interst is presented in the following figures. Each sub figure showing a slice of image in z direction. Although the uranium target can be seen in the presence of magnetic field but the distribution of PoCA points and the scattering angles are influenced by the magnet.

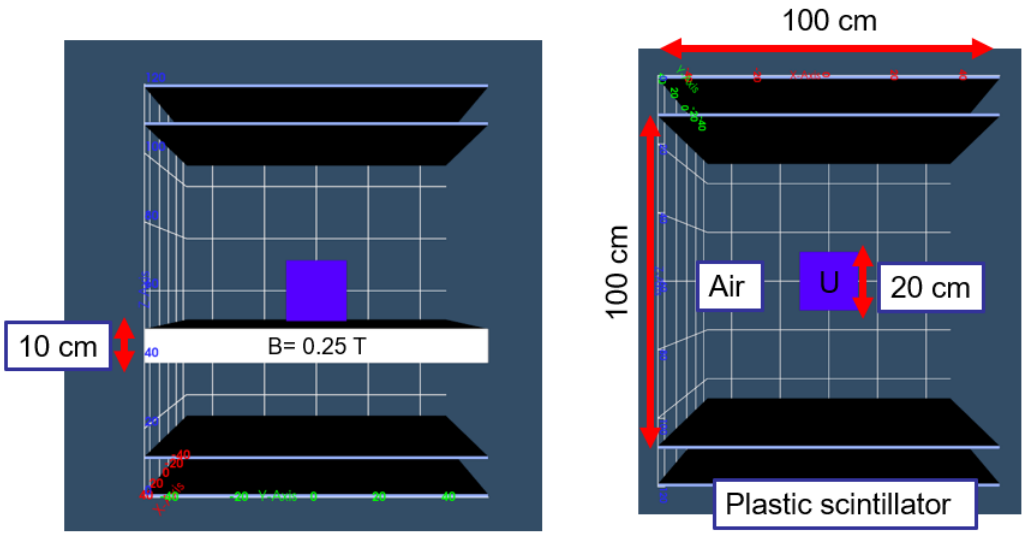

Fig. 4.6: Geometry of simulations used for investigation of the effect of magnetic field in material detection.

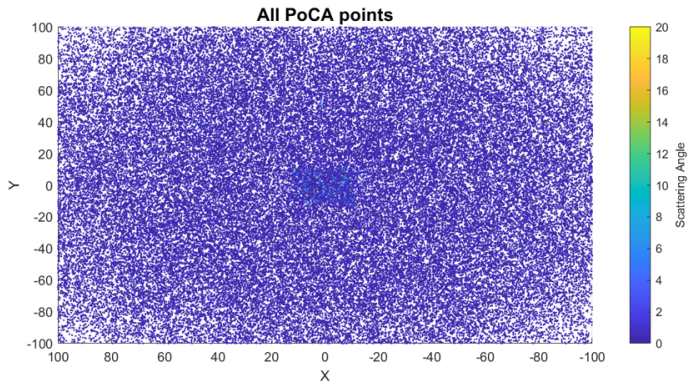

Fig. 4.7: Muography image of uranium target using all PoCA points.

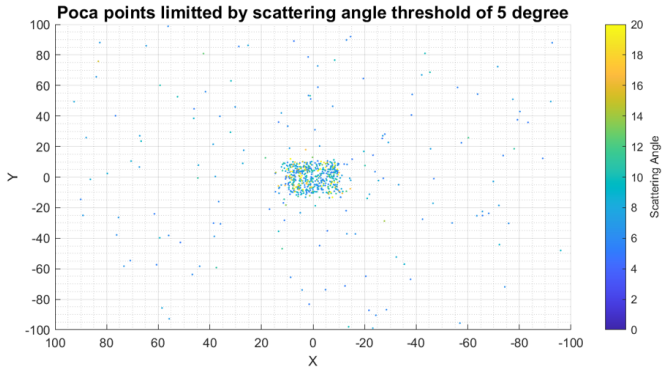

Fig. 4.8: Muography image of uranium target using a threshold of 5 degree for scattering angle.

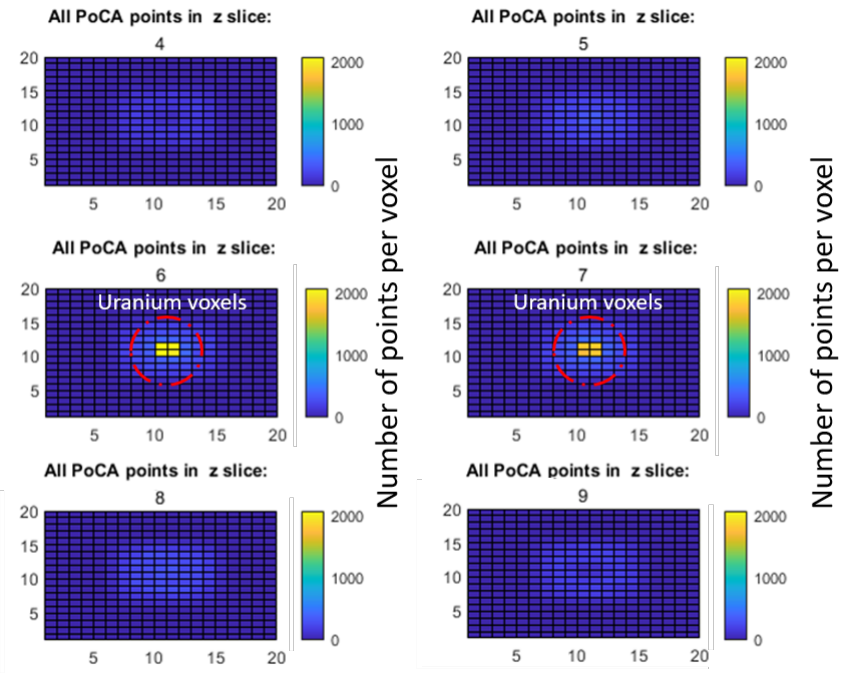

Fig. 4.9: Distribution of PoCA points in voxels in the absence of magnetic field.

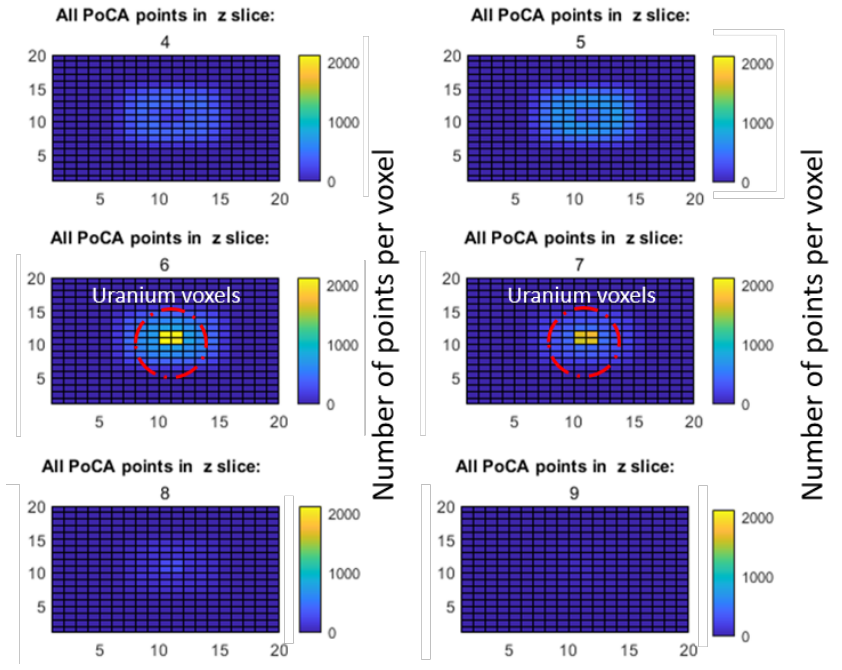

Fig. 4.10: Distribution of PoCA points in voxels in the presence of magnetic field.

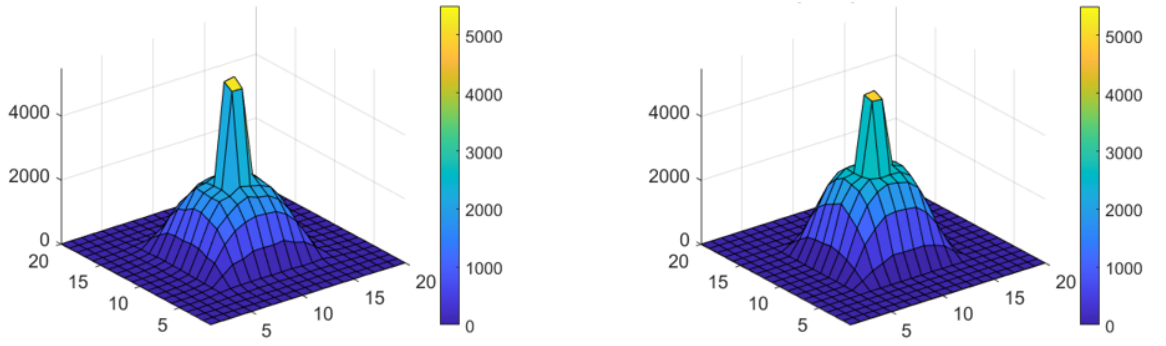

(a) PoCA points distribution in the absence of magnetic field

(b) PoCA points distribution in the presence of magnetic field

Fig. 4.11: Number of PoCA points in each voxel.

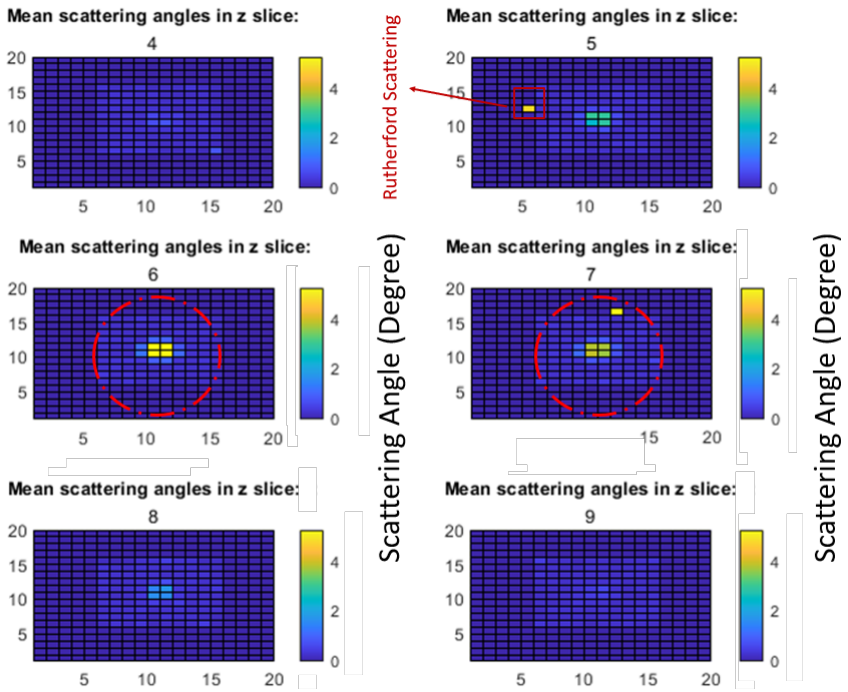

Fig. 4.12: Distribution of average scattering angles in voxels in the absence of magnetic field.

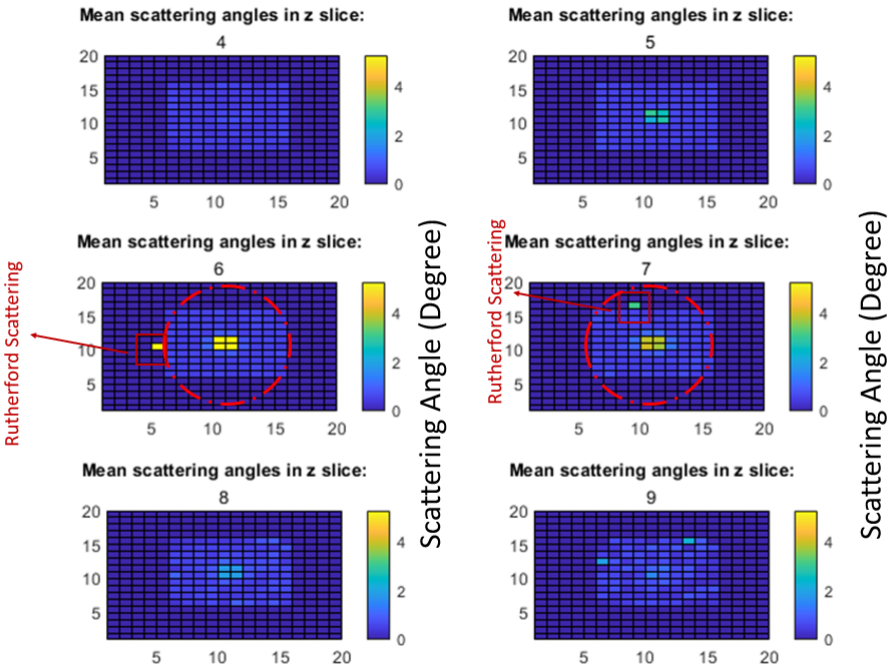

Fig. 4.13: Distribution of average scattering angles in voxels in the presence of magnetic field.

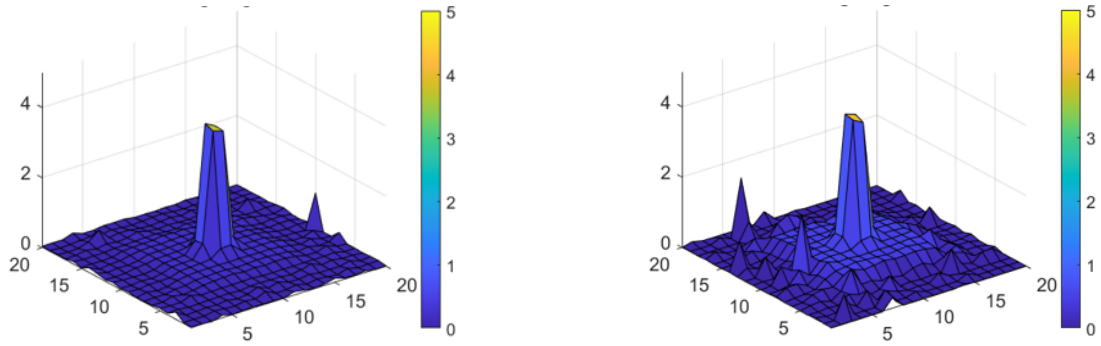

(a) Voxel mean scattering angle distribution in the absence of magnetic field

(b) Voxel mean scattering angle distribution in the presence of magnetic field

Fig. 4.14: Mean scattering angle inside each voxel.

If we plot the number of PoCA points in each voxel and then use K-means clustering method to divide the voxles into 2 clusters of Suspicions to nuclear material voxels and Normal voxels, we can see the shift and change in voxles as shown in Figures 4.15 and 4.16. In Conclusion, the magnetic field may have an impact on the material detection using cosmic-ray muons and in the presence of magnetic field some other materials might be

detected as nuclear material. Further research and investigations are necessary in this subject and if it approved, the systems proposed for the material identification must be capable of detecting the presence of magnetic field in the inspection area. In the next simulation, we will investigate the effect of magnetic field in a cargo inspection system.

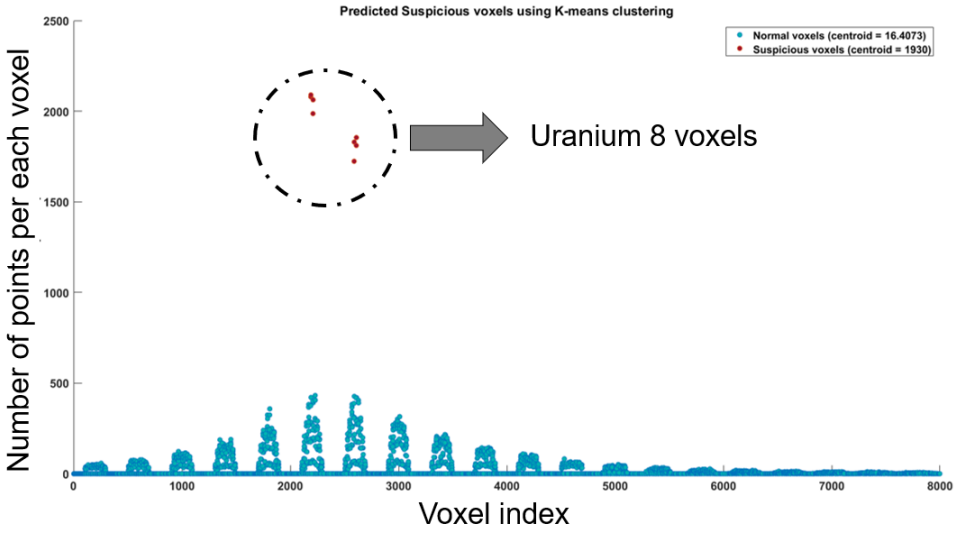

Fig. 4.15: Predicted suspicious voxels using K-means clustering in the absence of magnetic field.

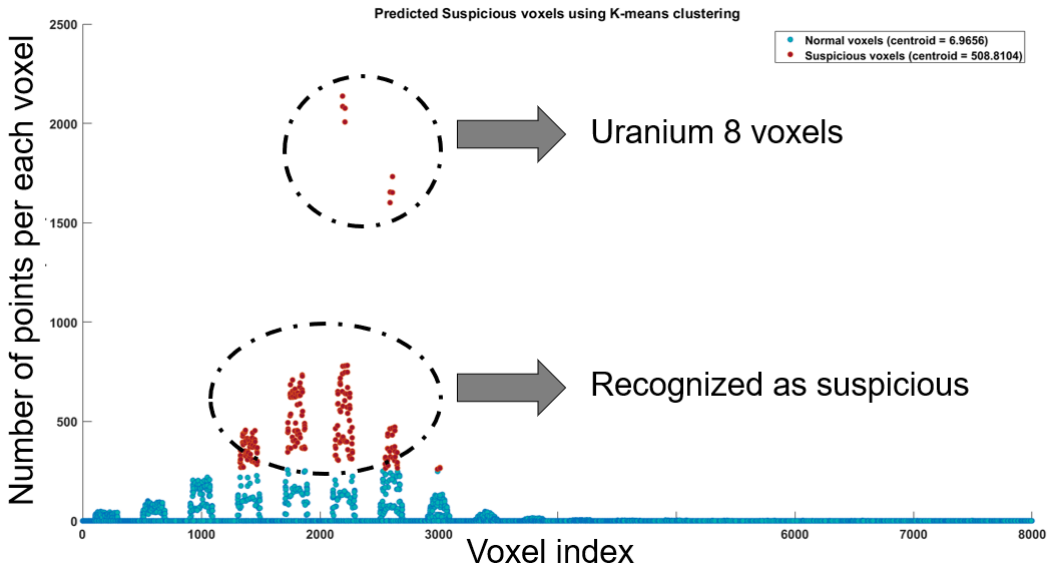

Fig. 4.16: Predicted suspicious voxels using K-means clustering in the presence of magnetic field.

4.2.2 Magnetic Field Effect in Imaging using Cosmic-ray Muons

To assess the impact of a magnetic field on material detection using muon-based systems, we designed a target shaped as the word "MUON", with a thickness of 40 cm, and placed it at the center of a standard 20-foot shipping container (dimensions: 600 cm x 234 cm x 228 cm). Each letter in the "MUON" target is comprised of a different material: M is made of uranium, U of lead, O of iron, and N of aluminum. The density of the materials decreases progressively from M to N. The detector, composed of a plastic scintillator, measures 3 m $\times$ 6 m. Fig. 4.17 provides an overview of the simulation geometry for the inspection system. The number of muons generated in this simulation corresponds to a measurement time of 13 minutes in a real-world setting.

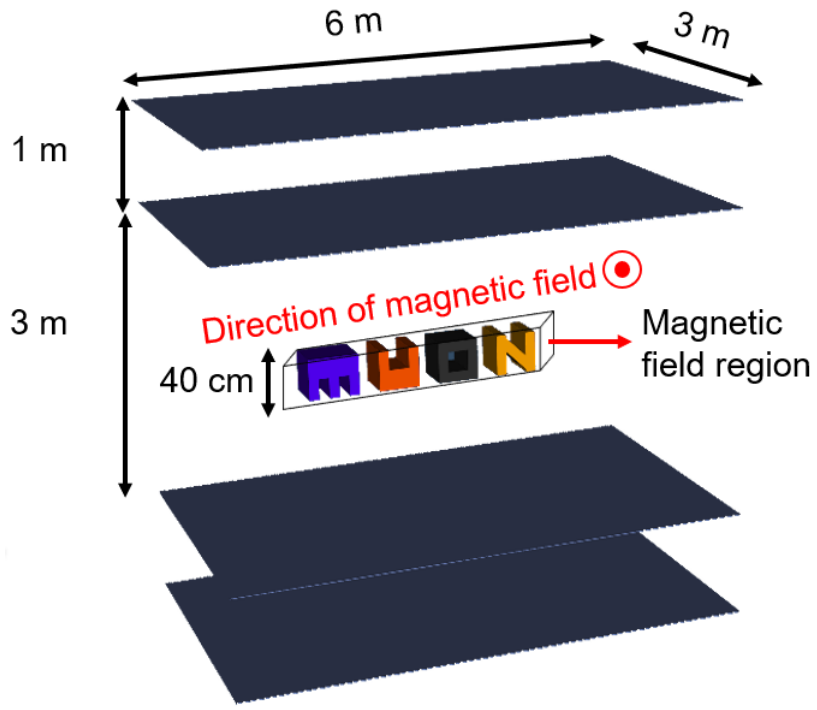

Fig. 4.17: Scheme of the design of the simulation study for the muon inspection system.

The simulation was conducted in two stages. Firstly, we obtained an image of the MUON target using the PoCA reconstruction algorithm. Secondly, we positioned the target within a uniform dipole magnetic field region and progressively increased the magnetic flux density from 100 mT to 500 mT, in 100 mT increments. We obtained a muography image of the target at each step. The image of the MUON target using the POCA algorithm is presented in Fig. 4.18, demonstrating how the image changes in response to the presence of different magnetic field intensities.

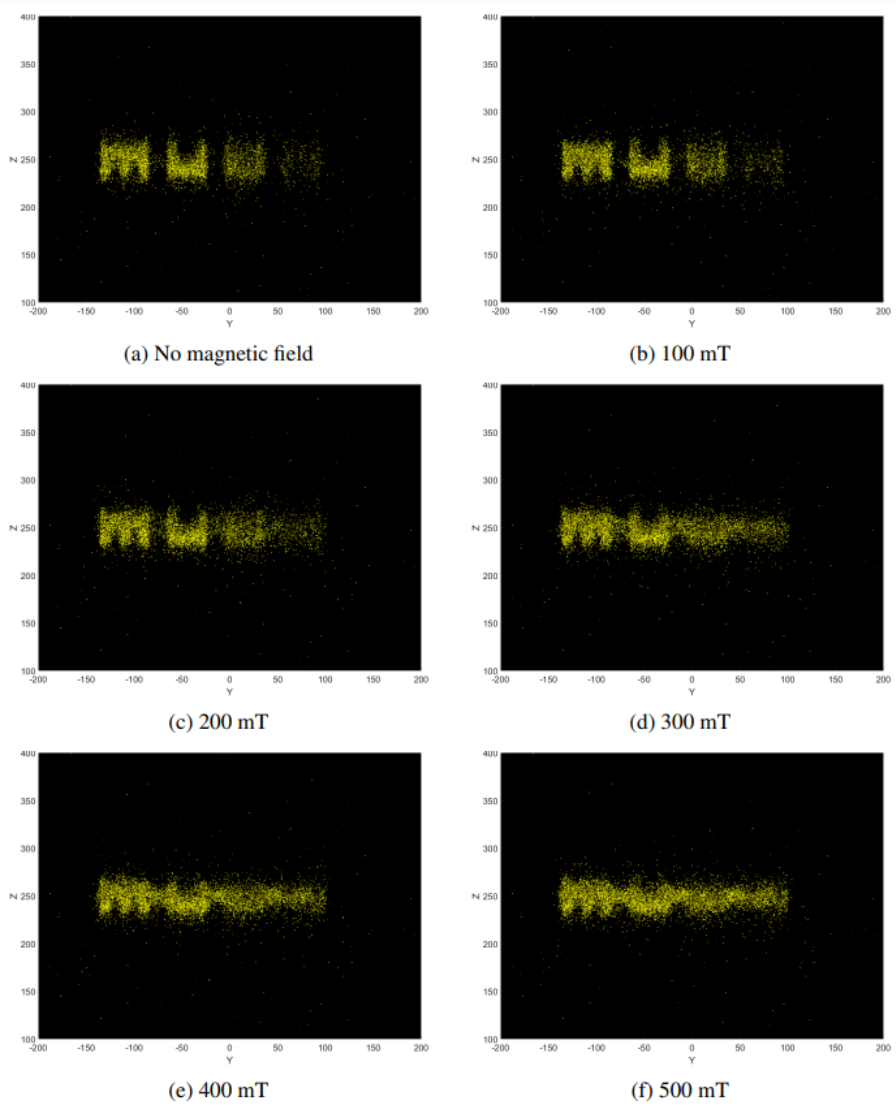

Fig. 4.18: Muography images under various magnetic fields.

As depicted in the figures, the magnetic field introduces noticeable deviations in the trajectory of the muons as they pass through the target and this lead to a change to the PoCA points obtained compared with the without magnet condition. This effect is particularly evident when comparing the image in the absence of magnetic field with the subsequent images, where the intensities of the magnetic fields range from 100 mT to 500 mT. As the magnetic field strength increases, the deflection of the muons becomes more pronounced, leading to observed distortions in the images of the MUON target. This highlights the impact of magnetic fields on the trajectories of cosmic-ray muons, an effect that needs to be considered when interpreting muon scattering data. A method to address this issue would be the charge identification. In the absence of magnetic field, the muography image of positive

and negative muons must be similar while in the presence of magnetic the positive and negative muons are deflected into opposite direction and will lead to a different image.

4.2.3 Magnetic Flux Density Estimation using a Known Magnet

To assess the method discussed in section 3.3.1, we implemented a simulation system as illustrated in Figure 4.19.

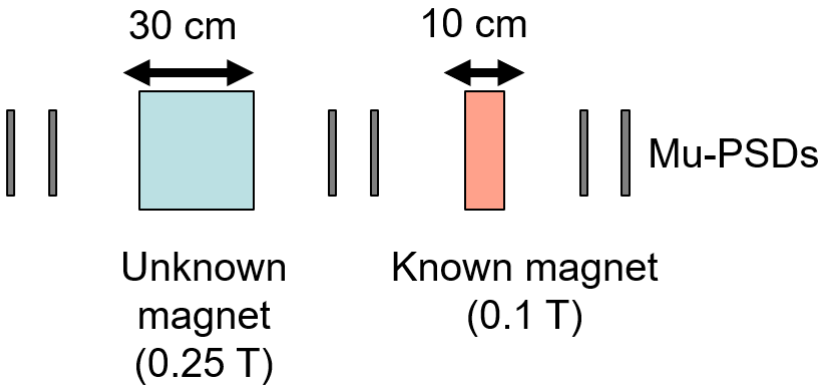

Fig. 4.19: Simulation geometry using a known magnetic field.

The simulation created a scenario where 100,000,000 cosmic-ray muons are generated within a hemisphere with a radius of 2 meters, emulating the distribution predicted by the PARMA model as implemented in the PHITS particle transport code. This muon distribution is comparable to a real-world measurement period of approximately 13 minutes and 15 seconds.

In this setup, the detector pairs were positioned 10 cm apart, each with a thickness of 1 cm. Two separate magnetic fields were introduced: the known magnetic field, with a thickness of 10 cm and a magnetic flux density of 0.1 T, and an unknown magnetic field, which had a thickness of 30 cm. In the simulation, we assumed an unknown magnetic flux density for the latter, setting it at 0.25T for the purpose of the test.

This simulation allowed us to observe and analyze the behavior and interactions of muons within a controlled environment, with known and unknown magnetic fields influencing their trajectory. It provided a framework to evaluate the validity and accuracy of our proposed magnetic flux density estimation method.

In the conducted simulation, we applied certain restrictions to utilize the information of the incoming muon. A muon was only considered in our analysis if it was detected in all six detector planes. Furthermore, we identified some muons that hit all detectors

but did not traverse the magnetic field as outliers. Outliers were defined as data points diverging more than three scaled Median Absolute Deviations (MAD) from the median. The scaled MAD is defined as $c \times median(abs(A - median(A)))$ in MATLAB software, where $c = -1/(\sqrt{2} \times \text{erfcinv}(3/2))$ [57].

In the initial part of the simulation, we determined the energy of each incoming muon by using a known magnetic field and derived equations. Figure 4.20 depicts the comparison between the calculated values and the actual values from the simulations. The red line represents the ideal case.

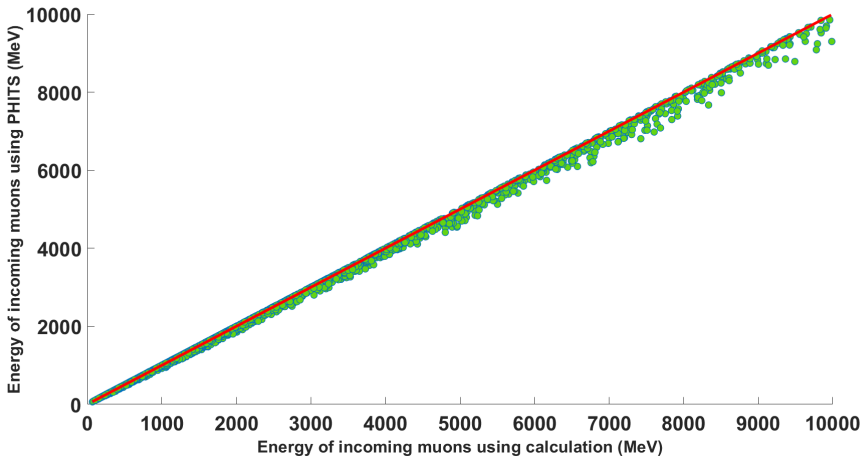

Fig. 4.20: Comparison of calculated and real values for muon energy.

Employing the known magnet, we could distinguish the muon type, whether positive or negative, as the direction of the magnetic field is known. Based on the calculated displacement, we determined the charge of the incoming particle. Using the displacement of muons in unknown magnetic field and the kinetic energy determined using the known magnet, the magnetic flux densities estimated to have a mean value of 0.25 and the standad deviation of 0.01 T which is similar to the true value.

4.2.4 Magnetic Flux Density Estimation Through PoCA Point Analysis

This section explores the correlation between magnetic flux density and the observed shifts in PoCA points. By conducting a simulation, we aimed to evaluate if these shifts, caused by a magnetic field, can be used to estimate the magnetic field's flux density.

The simulation model, detailed in Figure 4.21, was developed to facilitate this investigation. In this simulation, a lead block of 10 cm x 20 cm was placed beside a magnetic field region of 20 cm x 20 cm. Cosmic-ray muons are generated based on the PARMA model.

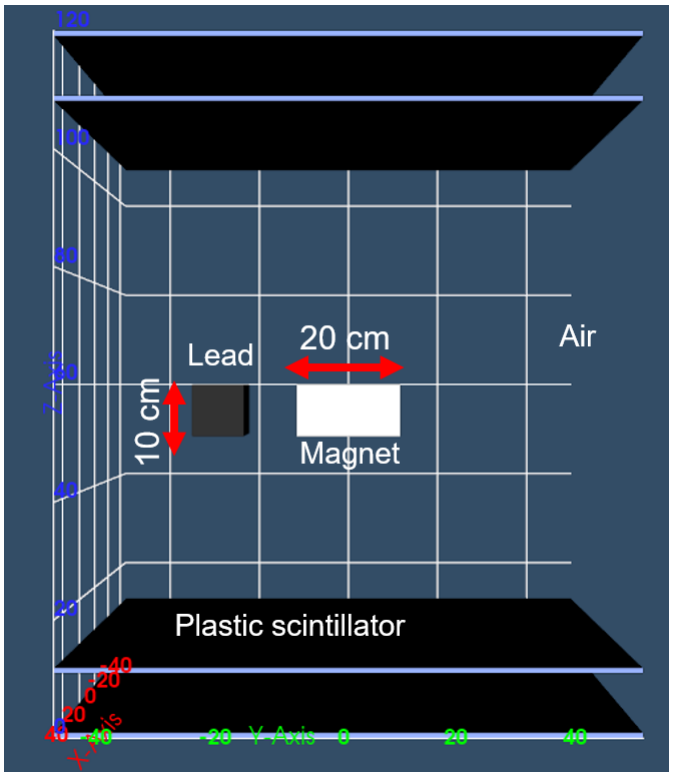

Fig. 4.21: The designed simulation geometry used for the estimation of magnetic flux density.

Using the PoCA algorithm, we extracted imaging data in a simulated setting. Figure 4.22 (a) shows the lead target's image in the absence of a magnetic field. Images of the lead block under magnetic fields of 0.55 T and 1 T are displayed in 4.22 (a) and (c) respectively. As shown in the graphs, the position of the magnetic field region is correctly determined and also the number of points in each voxel (shown by color) can represent magnetic field strength.

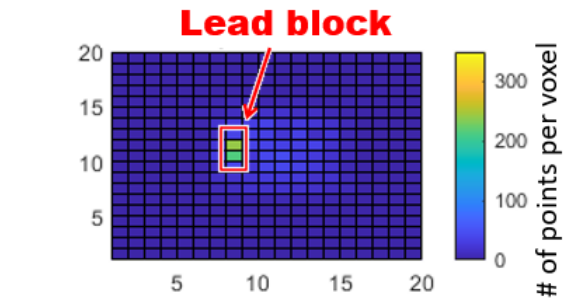

(a) Image of lead block

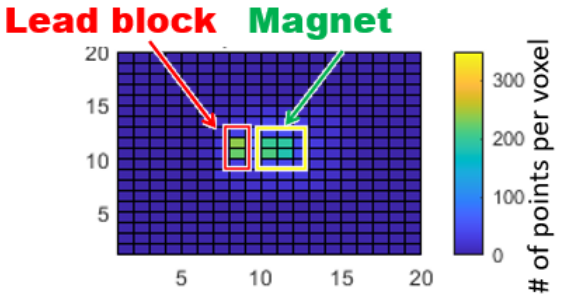

(b) Image of lead block and magnetic field of 0.55 T

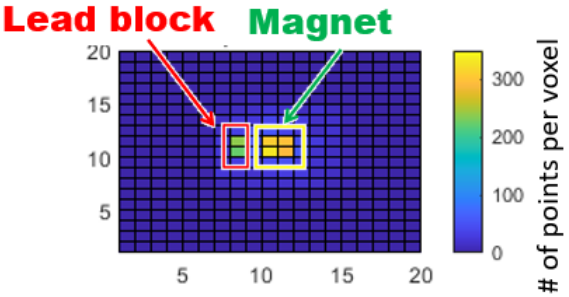

(c) Image of lead block and magnetic field of 1 T

Fig. 4.22: Imaging of the lead target and magnetic field.

After the simulations, we extracted features based on the PoCA points. To avoid complications caused by highly related features, we used a threshold rule. Any pair of features with a correlation coefficient above 0.8 was deemed highly correlated. One feature from each correlated pair was removed, resulting in a set of relatively uncorrelated features. These final features, including the average of each x, y, z, and the scattering angle of PoCA points, were used to estimate magnetic flux density.

We conducted the same simulation with various magnetic fields, creating a dataset based on PoCA points and the above-mentioned features. We split this data set into 70% training and 30% testing portions. The Ordinary Least Squares (OLS) model (which is a type of

linear regression analysis) was then fitted using the training data, enabling it to learn the relationship between the features and the target variable. This trained model was then used to predict the target variable for the testing data. The accuracy of these predictions was measured by comparing them with the actual values in the testing set.

Our results, presented in Figure 4.23, indicate the potential to estimate magnetic flux density for magnetic fields ranging from 0.1 to 1 tesla with an average absolute percentage error of 4.1%. This method does not apply to magnetic fields below 0.1 T, as for these weak fields, the PoCA points are determined more by the muons' scattering in the material than by deflection due to the magnet. For stronger fields, we could find out a relation between shifts in PoCA points and the magnetic field flux density.

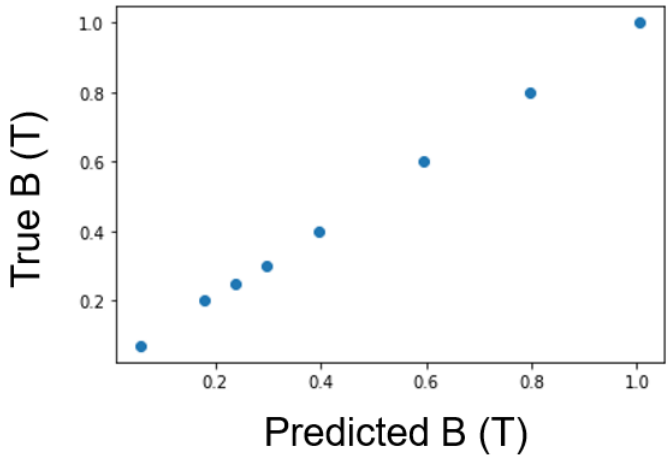

Fig. 4.23: Estimation of magnetic flux density using linear regression.

4.3 Summary

This chapter comprehensively outlined a variety of simulations and subsequent analyses illustrating the application of cosmic-ray muons in magnetic field detection and imaging. Magnetic field imaging can be possible by comparing magnetic field ON and OFF conditions using transmission muography. In the deflection method which the magnet is sandwiched between two detector sets, by using the information of incoming and outgoing muons and the PoCA algorithm, the magnetic field imaging is possible and the number of PoCA points in voxels can represent the strength of the magnetic field.

The simulations underscored the significant potential of cosmic-ray muons in magnetic field detection, involving scenarios with both strong and lower magnetic fields down to 200

mT. These studies provided a solid basis for our research conclusions, demonstrating the significant impact of varying magnetic fields on muon trajectories and imaging outcomes. We explored the impact of magnetic filed on material detection and cargo inspection systems.

The feasibility of using cosmic-ray muons for monitoring changes in strong magnetic fields associated with large structures like fusion reactors was established. This opens new doors for further study in magnetic field imaging using muon technology and offers promising implications for its practical application.

Moreover, by determining the energy of muons in a known magnet and through the utilization of PoCA point analysis, we estimated magnetic flux density.

These studies and their findings, combining the previous simulations and results chapters, significantly enhance our understanding and capabilities in cosmic-ray muon-based magnetic field imaging and detection. They set a robust foundation for future explorations, promising a bright future for the advancement of magnetic field imaging using cosmic-ray muons.

Chapter 5

Conclusions

The final chapter of this thesis provides a summary of the key findings, their implications for magnetic field detection, and recommendations for future research. It concludes with some final thoughts on the study and its potential impact on the field of muography.

5.1 Summary of Findings

Throughout this thesis, the potential application of cosmic-ray muons for magnetic field detection, imaging, and measurements using simulations has been investigated. As a novel and unexplored approach, this study introduces new possibilities and will require further research. In this thesis, we explored the principles and historical evolution of muography, including the creation and basic properties of cosmic-ray muons, their sources, and their interactions with matter. Then we reviewed existing magnetic field measurement techniques and proposed a new methodology for the application of muography in magnetic field studies. We developed two designs based on transmission and deflection muography for magnetic field investigations considering qualitative and quantitative approaches and proposed the analysis methods for each technique. Then simulation scenarios were created considering various magnetic field strengths and also the effect of magnetic field on material detection and imaging using the scattering muography has been investigated.In conclusion, The simulation results indicated that muography could be used to detect magnetic field and estimate magnetic flux density under certain conditions, highlighting the potential of this new methodology for practical applications.

5.2 Prospects

This thesis covered the groundwork and feasibility study of magnetic field imaging using cosmic-ray muons and gave us insight about the limitations and strength of the technique. For the next steps development and verification of methods for estimating the magnetic field is necessary. Also experimental work is needed for both transmission method and deflection method considering specific applications such as fusion reactor magnetic field monitoring or motor development for electric cars.

5.3 Concluding Remarks

This research represents an important step in the exploration of cosmic-ray muons for magnetic field imaging and measurements. It provides a theoretical foundation for this novel approach and demonstrates its potential through a series of simulations. However, much work remains to be done. The proposed methodologies and findings of this research must be validated and refined through further research and experimental testing. But despite these challenges, the potential benefits of this new application of muography are significant. By enabling a new way of measuring and monitoring magnetic fields, this research opens the door to a range of potential applications, from scientific research to industrial inspection and beyond.

References

[1] Seth H Neddermeyer and Carl D Anderson. Cosmic-ray particles of intermediate mass. *Physical Review*, 54(1):88, 1938.

[2] Thomas K Gaisser, Ralph Engel, and Elisa Resconi. *Cosmic rays and particle physics*. Cambridge University Press, 2016.

[3] A Haungs, J Blumer, B Fuchs, D Kang, S Schoo, D Wochele, J Wochele, WD Apel, JC Arteaga-Velázquez, K Bekk, et al. Kcdc—the kascade cosmic-ray data centre. In *Journal of Physics: Conference Series*, volume 632, page 012011. IOP Publishing, 2015.

[4] Viktor F Hess. Uber beobachtungen der durchdringenden strahlung bei sieben freiballonfahrten. *Phys. Zeits.*, 13:1084–1091, 1912.

[5] EP George. Cosmic rays measure overburden of tunnel. *Commonwealth Engineer*, 455, 1955.

[6] Luis W Alvarez, Jared A Anderson, F El Bedwei, James Burkhard, Ahmed Fakhry, Adib Girgis, Amr Goneid, Fikhry Hassan, Dennis Iverson, Gerald Lynch, et al. Search for hidden chambers in the pyramids. *Science*, 167(3919):832–839, 1970.

[7] S Minato. Feasibility study on cosmic-ray nondestructive testing through structural analysis of subway stations. *NDT international*, 20(4):231–234, 1987.

[8] JH Cobb, ML Marshak, WWM Allison, GJ Alner, DS Ayres, WL Barrett, C Bode, PM Border, CB Brooks, RJ Cotton, et al. Observation of a shadow of the moon in the underground muon flux in the soudan 2 detector. *Physical Review D*, 61(9):092002, 2000.

[9] Arturo Menchaca-Rocha. Searching for cavities in the teotihuacan pyramid of the sun using cosmic muons experiments and instrumentation. In *Proceedings of the 32nd International Cosmic Ray Conference (ICRC2011), held 11-18 August, 2011 in Beijing, China. Vol. 4 HE2: Extensive Air Showers and HE Cosmic Rays, p. 325*, volume 4, page 325, 2011.

[10] Konstantin N Borozdin, Gary E Hogan, Christopher Morris, William C Priedhorsky, Alexander Saunders, Larry J Schultz, and Margaret E Teasdale. Radiographic imaging with cosmic-ray muons. *Nature*, 422(6929):277–277, 2003.

[11] Hiroyuki KM Tanaka, Toshiyuki Nakano, Satoru Takahashi, Jyunya Yoshida, Minoru Takeo, Jun Oikawa, Takao Ohminato, Yosuke Aoki, Etsuro Koyama, Hiroshi Tsuji, et al. High resolution imaging in the inhomogeneous crust with cosmic-ray muon radiography: The density structure below the volcanic crater floor of mt. asama, japan. *Earth and Planetary Science Letters*, 263(1-2):104–113, 2007.

[12] Silvia Pesente, S Vanini, M Benettoni, G Bonomi, P Calvini, P Checchia, E Conti, F Gonella, G Nebbia, S Squarcia, et al. First results on material identification and imaging with a large-volume muon tomography prototype. *Nuclear Instruments and Methods in Physics Research Section A: Accelerators, Spectrometers, Detectors and Associated Equipment*, 604(3):738–746, 2009.

[13] Haruo Miyadera, Konstantin N Borozdin, Steve J Greene, Zarija Lukić, Koji Masuda, Edward C Milner, Christopher L Morris, and John O Perry. Imaging fukushima daiichi reactors with muons. *Aip Advances*, 3(5):052133, 2013.

[14] G Jonkmans, VNP Anghel, C Jewett, and M Thompson. Nuclear waste imaging and spent fuel verification by muon tomography. *Annals of Nuclear Energy*, 53:267–273, 2013.

[15] C Cârloganu, V Niess, S Béné, Emmanuel Busato, P Dupieux, F Fehr, Pascal Gay, Didier Miallier, B Vulpescu, Pierre Boivin, et al. Towards a muon radiography of the puy de dôme. *Geoscientific Instrumentation, Methods and Data Systems*, 2(1):55–60, 2013.

[16] S Kedar, HKM Tanaka, CJ Naudet, CE Jones, JP Plaut, and FH Webb. Muon radiography for exploration of mars geology. *Geoscientific Instrumentation, Methods and Data Systems*, 2(1):157–164, 2013.

[17] Aldo Zenoni. Historical building stability monitoring by means of a cosmic ray tracking system. In *2015 4th International Conference on Advancements in Nuclear Instrumentation Measurement Methods and their Applications (ANIMMA)*, pages 1–8. IEEE, 2015.

[18] Anthony Clarkson, David J Hamilton, Matthias Hoek, David G Ireland, JR Johnstone, Ralf Kaiser, Tibor Keri, Scott Lumsden, David F Mahon, Bryan McKinnon, et al. The design and performance of a scintillating-fibre tracker for the cosmic-ray muon tomography of legacy nuclear waste containers. *Nuclear Instruments and Methods in Physics Research Section A: Accelerators, Spectrometers, Detectors and Associated Equipment*, 745:138–149, 2014.

[19] S Bouteille, D Attié, P Baron, D Calvet, P Magnier, I Mandjavidze, S Procureur, M Riallot, and M Winkler. A micromegas-based telescope for muon tomography: The watto experiment. *Nuclear Instruments and Methods in Physics Research Section A: Accelerators, Spectrometers, Detectors and Associated Equipment*, 834:223–228, 2016.

[20] Kunihiro Morishima, Mitsuaki Kuno, Akira Nishio, Nobuko Kitagawa, Yuta Manabe, Masaki Moto, Fumihiko Takasaki, Hirofumi Fujii, Kotaro Satoh, Hideyo Kodama, et al. Discovery of a big void in khufu's pyramid by observation of cosmic-ray muons. *Nature*, 552(7685):386–390, 2017.

[21] D Lo Presti, G Gallo, Danilo Luigi Bonanno, Giovanni Bonanno, Daniele Giuseppe Bongiovanni, Daniele Carbone, C Ferlito, J Immè, P La Rocca, Fabio Longhitano, et al. The mev project: Design and testing of a new high-resolution telescope for muography of etna volcano. *Nuclear Instruments and Methods in Physics Research Section A: Accelerators, Spectrometers, Detectors and Associated Equipment*, 904:195–201, 2018.

[22] Decision sciences. https://decisionsciences.com/. [Accessed: 20/05/2023].

[23] Sébastien Procureur, David Attié, Laurent Gallego, Hector Gomez, Philippe Gonzales, Baptiste Lefèvre, Marion Lehuraux, Bertrand Lesage, Irakli Mandjavidze, Philippe Mas, et al. 3d imaging of a nuclear reactor using muography measurements. *Science Advances*, 9(5):eabq8431, 2023.

[24] Sébastien Procureur, Kunihiro Morishima, Mitsuaki Kuno, Yuta Manabe, Nobuko Kitagawa, Akira Nishio, Hector Gomez, David Attié, Ami Sakakibara, Kotaro Hikata, et al. Precise characterization of a corridor-shaped structure in khufu's pyramid by observation of cosmic-ray muons. *Nature Communications*, 14(1):1144, 2023.

[25] Rasha NI Altameemi, Nurul Shazana Abdul Hamid, Wan Mohd Aimran Wan Mohd Kamil, and Saad M Saleh Ahmed. Determination of muon absorption coefficients in heavy metal elements. *Journal of Radiation Research and Applied Sciences*, 12(1):281–288, 2019.

[26] Tatsuhiko Sato, Hiroshi Yasuda, Koji Niita, Akira Endo, and Lembit Sihver. Development of parma: Phits-based analytical radiation model in the atmosphere. *Radiation research*, 170(2):244–259, 2008.

[27] R. L. Workman et al. Review of Particle Physics. *PTEP*, 2022:083C01, 2022.

[28] Peter KF Grieder. *Extensive Air Showers: High Energy Phenomena and Astrophysical Aspects-A Tutorial, Reference Manual and Data Book*. Springer Science & Business Media, 2010.

[29] M Bahmanabadi. A method for determining the angular distribution of atmospheric muons using a cosmic ray telescope. *Nuclear Instruments and Methods in Physics Research Section A: Accelerators, Spectrometers, Detectors and Associated Equipment*, 916:1–7, 2019.

[30] Tatsuhiko Sato. Analytical model for estimating the zenith angle dependence of terrestrial cosmic ray fluxes. *PloS one*, 11(8):e0160390, 2016.

[31] Dieter Heck, Johannes Knapp, JN Capdevielle, G Schatz, T Thouw, et al. Corsika: A monte carlo code to simulate extensive air showers. *Report fzka*, 6019(11), 1998.

[32] Chris Hagmann, David Lange, and Douglas Wright. Cosmic-ray shower generator (cry) for monte carlo transport codes. In *2007 IEEE Nuclear Science Symposium Conference Record*, volume 2, pages 1143–1146. IEEE, 2007.

[33] Wolfgang Lohmann, Roberto Kopp, and Rüdiger Voss. Energy loss of muons in the energy range 1-10000 gev. Technical report, European Organization for Nuclear Research, 1985.

[34] Particle Data Group, PAea Zyla, RM Barnett, J Beringer, O Dahl, DA Dwyer, DE Groom, C-J Lin, KS Lugovsky, E Pianori, et al. Review of particle physics. *Progress of Theoretical and Experimental Physics*, 2020(8):083C01, 2020.

[35] AA Petrukhin and VV Shestakov. The influence of the nuclear and atomic form factors on the muon bremsstrahlung cross section. *Canadian Journal of Physics*, 46(10):S377–S380, 1968.

[36] P Amaral and ATLAS Collaboration. A precise measurement of 180 gev muon energy losses in iron. *The European Physical Journal C-Particles and Fields*, 20(3):487–495, 2001.

[37] Alireza Haghighat. *Monte Carlo methods for particle transport*. Crc Press, 2020.

[38] Tatsuhiko Sato, Yosuke Iwamoto, Shintaro Hashimoto, Tatsuhiko Ogawa, Takuya Furuta, Shin-ichiro Abe, Takeshi Kai, Pi-En Tsai, Norihiro Matsuda, Hiroshi Iwase, et al. Features of particle and heavy ion transport code system (phits) version 3.02. *Journal of Nuclear Science and Technology*, 55(6):684–690, 2018.

[39] Geant Collaboration. Geant4 user's guide for application developers. *Accessible from the GEANT4 web page [1] Version geant4*, 9, 2012.

[40] Rene Brun, L Urban, Federico Carminati, Simone Giani, M Maire, A McPherson, F Bruyant, and G Patrick. Geant: detector description and simulation tool. Technical report, CERN, 1993.

[41] A. Ferrari, A. Fasso, P.R. Sala, J. Ranft, Stanford Linear Accelerator Center, United States. Department of Energy. Office of Scientific, and Technical Information. *FLUKA: A Multi-Particle Transport Code*. United States. Department of Energy, 2005.

[42] Giuseppe Battistoni, A Ferrari, S Muraro, and PR Sala. Atmospheric muon simulation using the fluka mc model. *Nuclear Physics B Proceedings Supplements*, 168:286–288, 2007.

[43] T Goorley, Michael James, Thomas Booth, F Brown, J Bull, LJ Cox, J Durkee, J Elson, Michael Fensin, RA Forster, et al. Initial mcnp6 release overview. *Nuclear technology*, 180(3):298–315, 2012.

[44] Natalia Zaitseva, Andrew Glenn, Leslie Carman, Robert Hatarik, Sebastien Hamel, Michelle Faust, Brandon Schabes, Nerine Cherepy, and Stephen Payne. Pulse shape discrimination in impure and mixed single-crystal organic scintillators. *IEEE Transactions on Nuclear Science*, 58(6):3411–3420, 2011.

[45] Ervin B Podgoršak et al. *Radiation physics for medical physicists*, volume 1. Springer, 2006.

[46] Mukund Gupta. Calculation of radiation length in materials. Technical report, CERN, Geneva, 2010.

[47] Hans A Bethe. Moliere's theory of multiple scattering. *Physical review*, 89(6):1256, 1953.

[48] Bruno Rossi and Kenneth Greisen. Cosmic-ray theory. *Reviews of Modern Physics*, 13(4):240, 1941.

[49] Virgil L Highland. Some practical remarks on multiple scattering. *Nuclear Instruments and Methods*, 129(2):497–499, 1975.

[50] Claude Amsler, Michael Doser, P Bloch, A Ceccucci, GF Giudice, A Höcker, ML Mangano, A Masoni, S Spanier, NA Törnqvist, et al. Review of particle physics. *Physics Letters B*, 667(1-5):1–6, 2008.

[51] Gerald R Lynch and Orin I Dahl. Approximations to multiple coulomb scattering. *Nuclear Instruments and Methods in Physics Research Section B: Beam Interactions with Materials and Atoms*, 58(1):6–10, 1991.

[52] Donald E Groom, Nikolai V Mokhov, and Sergei I Striganov. Muon stopping power and range tables 10 mev–100 tev. *Atomic Data and Nuclear Data Tables*, 78(2):183–356, 2001.

[53] John David Jackson. Classical electrodynamics, 1999.

[54] Daniel Sunday. Practical geometry algorithms: With c++ code. *KDP Print US*, 2021.

[55] S. Noda T. Kin, T. Komori and T. Amano. Method and device for discriminating energy of radiation ray using machine learning. *Japanese PatentsApplication*, 2019-160460, Deciusion to Grant a Patent on Jun.13,2023.

[56] Rene Brun and Fons Rademakers. ROOT — An object oriented data analysis framework. *Nuclear Instruments and Methods in Physics Research Section A: Accelerators, Spectrometers, Detectors and Associated Equipment*, 389(1-2):81–86, 1997.

[57] MATLAB. *9.12.0.1956245 (R2022a)*. The MathWorks Inc., Natick, Massachusetts, 2022.

List of figures

1.1 Particle classification. 2
1.2 Schematic view of an extensive air shower. 3
1.3 Absorption muography method. 7
1.4 Scattering muogaphy method. 8
1.5 Muon multiple scattering. 9
1.6 A plastic scintillator based muography detector. 10
1.7 Application of muography (Image by Lynkeos). 13

2.1 A positive muon crossing a magnetic field. 20
2.2 Muons of various energies interacting with a 0.5 T, 20 cm thick magnetic field. 22
2.3 Muons of various energies interacting with a 5 T, 20 cm thick magnetic field. 22
2.4 Effect of a 500 mT magnetic field on the tracks of 1 GeV muons. 23
2.5 Energy spectrum of cosmic ray muons at sea level. 24
2.6 Vertical differential cosmic ray muon momentum spectrum in the range of 0.2–10 GeV/c. 25
2.7 The variation of cosmic ray muon flux with zenith angles in the range of 0 – 89° at sea level. 26
2.8 Comparison of muon interactions shares in iron. 29
2.9 Mean energy loss rate in some materials. 31
2.10 Mass stopping power (= $< -dE/dx >$) for positive muons in copper as a function of $\beta\gamma = p/Mc$ over nine orders of magnitude in momentum (12 orders of magnitude in kinetic energy). The approximated cosmic muon energy range is indicated with vertical blurred lines 32

3.1 Transmission muography. 38
3.2 Simulation used for muography image of 10 iron plates. 39
3.3 Muography image of 10 iron plates for (a) normal muography and (b) in the presence of a quadrupole magnetic field. 39

3.4 Cumulative Distribution Function (CDF) and Probability Density Function (PDF) of muons calculated by the PARMA model. 40
3.5 Design of magnetic field measurement based on transmission muography. . 41
3.6 Figure of merit analysis 41
3.7 Design of magnetic field measurement system using scattering muography . 43
3.8 Positive muons in a magnetic field. 48
3.9 Schematic of the PoCA algorithm. 50
3.10 Illustration of the magnetic field's influence on PoCA points. 51
3.11 Magnetic field region and uranium target simulation geometry. 52
3.12 Uranium target with no magnetic field. 53
3.13 Magnetic field of 100 mT and uranium target. 53
3.14 Magnetic field of 200 mT and uranium target. 54
3.15 Magnetic field of 500 mT and uranium target. 54
3.16 Magnetic field of 1 T and uranium target. 55
3.17 Magnetic field of 5 T and uranium target. 55
3.18 Geometry of simulation using 4 targets. 56
3.19 Muography image of 4 targets using PoCA algorithm. 56
3.20 Influence of magnetic field on the image of 4 targets. 57
3.21 Displacement of muons due to magnetic field. 58
3.22 Setup of detectors and magnetic fields. 59
3.23 Multi-layer muon energy spectrometer. 62

4.1 Simulation setup and conditions for magnetic field imaging. 64
4.2 (a) Muography images (attenuation ratio maps) of nine blocks with magnetic field flux densities of different magnitudes. (b) Magnetic field regions determined by the FOM methods are colored red, and the actual magnetic regions are indicated by dashed lines. 65
4.3 Geometry of simulation in PHITS. 67
4.4 Simulation of the set-up for this feasibility study (a), and effect of the magnetic field on the muon trajectories (b,c) illustrated for the case of 100 MeV energy. 68
4.5 Muon counting rate maps for a realistic simulation of the muon flux. 69
4.6 Geometry of simulations used for investigation of the effect of magnetic field in material detection. 71
4.7 Muography image of uranium target using all PoCA points. 71
4.8 Muography image of uranium target using a threshold of 5 degree for scattering angle. 71

4.9 Distribution of PoCA points in voxels in the absence of magnetic field. . . 72
4.10 Distribution of PoCA points in voxels in the presence of magnetic field. . . 72
4.11 Number of PoCA points in each voxel. 73
4.12 Distribution of average scattering angles in voxels in the absence of magnetic field. 73
4.13 Distribution of average scattering angles in voxels in the presence of magnetic field. 74
4.14 Mean scattering angle inside each voxel. 74
4.15 Predicted suspicious voxels using K-means clustering in the absence of magnetic field. 75
4.16 Predicted suspicious voxels using K-means clustering in the presence of magnetic field. 75
4.17 Scheme of the design of the simulation study for the muon inspection system. 76
4.18 Muography images under various magnetic fields. 77
4.19 Simulation geometry using a known magnetic field. 78
4.20 Comparison of calculated and real values for muon energy. 79
4.21 The designed simulation geometry used for the estimation of magnetic flux density. 80
4.22 Imaging of the lead target and magnetic field. 81
4.23 Estimation of magnetic flux density using linear regression. 82

List of tables

2.1 Energy loss of muons for different energies in iron 29
2.2 Parameters used in and Bethe-Bloch formula. 30
2.3 Minimum and maximum energy loss rates of muons for different materials within the cosmic muon energy range (0.1 to 100 GeV/c). 33

3.1 Radiation length calculations for various materials. 45
3.2 Constant parameters. 59